Computer Simulations of Chemical Reactions on Metal Oxide Surfaces

Dissertation

zur

Erlangung der naturwissenschaftlichen Doktorwürde
(Dr. sc. nat.)

vorgelegt der

Mathematisch-naturwissenschaftlichen Fakultät
der
Universität Zürich

von

Konstanze Regina Hahn
aus
Deutschland

Promotionskomitee
Prof. Dr. Jürg Hutter (Vorsitz und Leitung)
Prof. Dr. Karl-Heinz Ernst

Zürich, 2013

Abstract

In this work, the suitability of density functional theory (DFT) for the simulation of metal oxides has been evaluated and compared to extended methods such as DFT+U and hybrid DFT (PBE0). The DFT+U method has been applied to study the formation of small Ni clusters on the CeO_2 surface showing a stabilization of the particles with increased number of Ni atoms. Ni-Ni bond length and gyration radius of Ni particles supported on CeO_2 have been shown to be larger compared to similar Ni clusters in the gas phase indicating an opening of the cluster structure. It is suggested that this leads to enhanced accessibility and improved catalytic activity of the Ni clusters.

Investigation of CO_2 adsorbed on the $CeO_2(111)$ surface has identified a monodentate carbonate species of CO_2 to be most stable on CeO_2 at low coverage. Activation of CO_2 is similar to what has been found on pure metals such as Pt, Ni and Pd. Increasing CO_2 coverage leads to a destabilization of the monodentate species directing a mixed adsorption mechanism with both carbonate and linear CO_2 species.

Poor selectivity in particular in the presence of H_2O vapor is one of the main drawbacks of SnO_2 gas sensors. Experimentally, it has been shown that this can be overcome by doping of SnO_2 with other metal atoms. Here, the formation of $Sn_{1-x}Ti_xO_2$ solid solutions has been evaluated demonstrating favorable distribution of Ti on the SnO_2 surface. The introduction of Ti atoms on six-fold surface sites has further been shown to destabilize H_2O species adsorbed dissociatively on the $Sn_{1-x}Ti_xO_2$ surface. An overall minimum in the absolute value of H_2O binding energy has been found at 25-30% surface Ti content. This gives a possible explanation for the minimum in cross-sensitivity to humidity found experimentally for Ti-doped SnO_2 particles.

Kurzfassung

In dieser Arbeit wurde die Eignung von DFT für die Berechnung von CeO_2 untersucht und mit erweiterten Methoden (DFT+U und hybrid DFT) verglichen. Die DFT+U Methode wurde verwendet, um die Formation von Ni-Partikeln auf einer CeO_2-Oberfläche zu untersuchen. Es wurde gezeigt, dass die Stabilität der Ni-Anhäufungen mit der Anzahl an Ni-Atomen steigt. Die Charakterisierung der geometrischen Eigenschaften zeigte auf, dass sich die Struktur von Ni-Partikeln auf CeO_2 im Vergleich zu entsprechenden Partikeln in der Gasphase öffnet. Dies lässt die Schlussfolgerung zu, dass Ni-Partikel, abgelagert auf CeO_2 zugänglicher für adsorbierende Moleküle sind als reines Ni und deshalb einen geeigneteren Katalysator darstellen.

Des Weiteren wurde die Adsorption von CO_2 auf CeO_2 untersucht und eine Karbonatverbindung aus CO_2 und einem Oberflächensauerstoffatom als stabilste Form gefunden. Diese Struktur ist jedoch nur bis zu einer bestimmten Beladung stabil. Bei hohen Beladungen sind neben der Karbonatstrukturen außerdem lineare CO_2-Moleküle vorhanden.

Der Schwachpunkt von SnO_2-Gassensoren ist deren geringe Selektivität, insbesondere bei hoher Luftfeuchtigkeit. Eine Verbesserung der Selektivität kann durch die Dotierung mit anderen Metallen erreicht werden. In dieser Arbeit wurde die Struktur von $Sn_{1-x}Ti_xO_2$ Mischkristallen untersucht. Es wurde festgestellt, dass sich Ti-Fremdatome bevorzugt an der SnO_2-Oberfläche ansammeln und die Lokalisierung von Ti auf sechsfach-koordinierten Oberflächenplätzen zu einer Destabilisierung von H_2O auf $Sn_{1-x}Ti_x(110)$ führt. Dies gibt eine mögliche Erklärung für die optimale Selektivität für Ethanoldetektion in feuchter Umgebung, die experimentell für Ti-dotierte SnO_2-Partikel bei einem Ti-Gehalt von 4.6 at% ermittelt wurde.

Acknowledgements

Truly, I have written this thesis. But the writing is not all behind a PhD, this is only the top of the mountain. Behind is a huge learning process about failing and getting up again, about how to address problems and discrepancies with your colleagues, about how to organize your time and assigning priorities and eventually about yourself and forming your own ideas. However, this whole process that I went through in the last four years would have never been possible without the interaction and courtesy of the many valuable people around me.

In this respect, I would firstly like to express my deepest gratitude to my advisor Jürg Hutter for giving me the possibility to pursue my PhD that I started at ETH. I am not sure if I had continued my academic carrier without his offer to proceed my work with him. It has been a pleasure working in the kind environment of his group and to experience that there are still professors who are actually doing research themselves. I am greatly inspired by his way of conducting all the necessary bureaucratic work without giving up the actual hands-on research.

On the financial site I would like to thank the University of Zurich supporting my work with the Forschungskredit 2012 from September 2012 to June 2013.

I am grateful for the collaboration of Gianluca Santarossa, Angelo Vargas and Prof. Baiker who supported the work I started at ETH.

Furthermore, I would like to thank Manos for all his support throughout my thesis, especially for his encouragement and his advice when I was looking for another group to continue my PhD.

I would like to thank all my group members and the CMSZH graduate school for a great time at the Institute of Physical Chemistry at UZH. In particular, I thank Rebecca for her work that she conducted during her bachelor thesis with me. Special thanks also go to Ari who was never tired of explaining the basics of molecular orbital and group theory to me and who carefully revised my manuscripts. Even though

I sometimes felt really stupid, I'm still convinced I learned a lot from our discussions.

Moreover, I am really grateful to have met the running team here, including Julien, Marcella, Ana, Ari and Jaime. I should probably mention Jaime in particular who was always there for me, no matter if it was for lunch, running, Spanish lessons or discussion of our work. Maybe it was also part of the learning process to realize that life is always too short and never predictable. It is great to have met you, Jaime.

Peró mi sa che la persona piu importante durante il mio dottorato all'Università sia stata Marcella. É stato un grande piacere dividere l'ufficio con lei, sentire le storie di Akira ed Aisha, ridere insieme e discutere i problemi scientifici. Grazie di essere una collega meravigliosa e di tutto ció che mi hai insegnato.

But as mentioned before, the PhD, at least in my opinion, is not only about writing and working. I would have never been able to focus on my work without all my friends in the background. It was great to recover some mental energy during the climbing sessions with Dan and Dani. I'm definitely also very grateful to have met Daphne, Valeria, Elsa and Ana during my PhD who were always there when I needed them. Especially Ana. Volim te.

Vorrei anche ringraziare Antonio che mi ha insegnato tantissime cose del mondo academico e che é sempre stato qua per me nei primi tre anni del dottorato.

Last but not least, I'd like to thank my family for the best, warmest and strongest mental support I could have ever asked for. Danke, dass ihr immer für mich da seid, Rine, Mama, Papa und Max.

The most beautiful thing we can experience is the mysterious. It is the source of all true art and all science. He to whom this emotion is a stranger, who can no longer pause to wonder and stand rapt in awe, is as good as dead: his eyes are closed.

Albert Einstein, 1931

Publications

This work has led to several publications. The chapters based on these scientific articles are listed below.

1. Chapter 5
   K. R. Hahn, M. Iannuzzi, A. P. Seitsonen and J. Hutter, "Coverage Effect of the CO_2 Adsorption Mechanisms on CeO_2(111) by First Principles Analysis", *Journal of Physical Chemistry C* 117(4) **2013**, 1701-1711.

2. Chapter 6
   K. R. Hahn, A. Tricoli, G. Santarossa, A. Vargas and A. Baiker, "Theoretical Study of the (110) Surface of $Sn_{1-x}Ti_xO_2$ Solid Solutions with Different Distribution and Content of Ti", *Surface Science* 605(15-16) **2011**, 1476-1482.

3. Chapter 7
   K. R. Hahn, A. Tricoli, G. Santarossa, A. Vargas and A. Baiker, "First Principles Analysis of H_2O Adsorption on the (110) Surfaces of SnO_2, SnO_2 and Their Solid Solutions", *Langmuir* 28(2) **2012**, 1646-1656.

Contents

1

Introduction

Metal oxide-based materials have gained increased interest in numerous technologically important applications in the last century. Among others they have shown to exhibit excellent properties for microchip technology [1, 2], in spintronic devices [3, 4], in solar cells [5, 6], as portable chemoresistive gas sensors [7–9] and as photocatalysts [10–12].

Recently, the trend in development and improvement of microchip materials focuses on the miniaturization of the device. However, traditionally used materials for gate insulators in microchips based on Si have reached their fundamental size limits [1] resulting from their small dielectric constant. In this respect, oxides from rare earth metals have shown to be promising alternatives owing to their high stability in contact with Si and their high dielectric constants [2].

The magnetic properties of oxides doped with metal atoms such as Co also make them interesting materials for spintronic devices. Investigation of Co-doped TiO_2, ZnO and CeO_2 has revealed that the ferromagnetism of such materials is mainly affected by the host oxide [3]. Control of the ferromagnetism is desired to design materials for improved data storage devices [4].

Another interesting field for metal oxide-based materials is in gas sensing technology. Important specifications of technologically used gas sensors are a high sensitivity, selectivity and the miniaturization potential. Adsorption already of small amounts of molecules on semiconducting metal oxides (MO) changes the electronic properties of the system (conductivity) resulting in a high sensitivity towards a certain analyte of such materials. This is especially important in situations when the concentration of the analyte is very small, for example, in breath analysis where volatile compounds need to be detected down to ppb concentrations. Furthermore it has been shown that the signal of metal oxide based sensors can even be enhanced when the system size is reduced below twice the Debye length [13–15]. It is thus possible and even advantageous to reduce the size

of gas sensing metal oxides to the nanoscale. The reliability of the sensor signal is an important issue when the sensing device is exposed to an environment with competing species. It is limiting the performance of a gas sensor in particular in breath analysis where water vapor, a competing species with the actual analyte, is omnipresent and the relative humidity in the environment is changing arbitrarily. This is, for example, the case for SnO_2 exhibiting a high sensitivity towards several analytes [16], however, also suffering from a significant cross-sensitivity to background conditions [7]. Doping of SnO_2 nanoparticles with small amounts of Ti has been shown to improve the reliability of such chemoresistive gas sensors in the presence of relative humidity [17]. In this respect, doped and mixed metal oxides have a great potential to be specifically designed for enhanced sensing properties in a particular environment.

Semiconducting metal oxides such as TiO_2 and ZnO are also used as photocatalysts, for example for water and CO_2 splitting [10, 18, 19]. Early research in 1972 has demonstrated the photoinduced decomposition of H_2O on TiO_2 [10]. Since then intensive research has been done to optimize the photocatalytic behavior of TiO_2-based catalysts for hydrogen production from H_2O or hydrocarbons and for degradation of organic pollutants [20, 21]. In fact, it has been shown that doping of TiO_2 with substitutional or interstitial species, in particular nitrogen, significantly improves the performance of the photocatalyst [11, 22].

The wide range of technological applications for metal oxide based materials demonstrates their importance in our society. Recent research on the performance of metal oxide supported materials or mixed/doped metal oxides indicates the high potential to further improve and optimize the performance of MO based materials. Possibilities of such mixed metal oxides, however, are numerous. In this respect, theoretical simulations of such materials offer a great possibility to investigate and understand the material properties and to suggest novel compositions for high-performing materials.

First principles calculations, for example based on density functional theory (DFT), have been shown to be an adequate tool to determine the catalytic properties of transition metals based on their electronic structure and to screen for the best material [23, 24]. Similar strategies have been proposed for metal oxides [25, 26]. However, DFT suffers from serious errors in the electronic structure description of strongly correlated systems. This results from the self-interaction error of standard DFT and is in particular problematic for the simulation of transition and rare earth metal oxides where strong interactions between the d and f bands, respectively, are present. As a result, using DFT, certain insulating materials such as UO_2 [27], Ge [28] and reduced CeO_2 [29, 30] are predicted to be metallic and the band gap of wide band gap semiconductors is significantly underestimated [31, 32]. Thus, a careful evaluation of the structural and electronic properties of metal oxides obtained from DFT calculations is neccessary.

In this work, advanced metal oxide surfaces have been studied addressing their properties towards adsorption of small molecules. In particular, bulk and surface properties of CeO_2 have been determined and subsequent adsorption of small Ni clusters on the $CeO_2(111)$ surface has been investigated. Furthermore, the suitability of $CeO_2(111)$ as a CO_2 catalyst has been evaluated simulating adsorption of CO_2 at different coverages. The second part focuses on SnO_2-TiO_2 solid solutions including the stability of their (110) surfaces and their properties for H_2O adsorption. The goal is to understand the effect of Ti atoms in the SnO_2 structure on the adsorption of H_2O and to possibly explain the behavior of the cross-sensitivity to humidity of SnO_2-TiO_2 gas sensors. The content of chapters 5 to 7, is based on research articles published in connection with this thesis [33–35].

2

Theory

2.1 Density Functional Theory

Theoretical background of density functional theory is discussed here only briefly. A detailed description of the detailed background can be found elsewhere [32, 36–40].

2.1.1 Schrödinger Equation

Density functional theory is based on the Schrödinger equation which describes in principle the motion of a quantum mechanical system equivalent to the Newton equation in classical mechanics. The fundamental expression for the total energy of a quantum mechanical system is the time-independent Schrödinger equation (eq. (2.1)) which correlates the standing waves ψ (wavefunctions) of a system with its total energy E in an eigenvalue problem.

$$\hat{H}\psi = E\psi \tag{2.1}$$

The quantum mechanical picture of a molecular system typically assumes the light electrons to move around in the potential of the much heavier fixed nuclei. According to this assumption, known as the Born-Oppenheimer approximation [41], the Schrödinger equation can be solved for electrons moving in the static electric field of the nuclei represented in eq. (2.2).

$$\begin{aligned} \hat{H}_{el}\left(\mathbf{R}\right)\psi\left(\mathbf{r};\mathbf{R}\right) &= E_{el}\left(\mathbf{R}\right)\psi\left(\mathbf{r};\mathbf{R}\right) \\ \hat{H}_{el} &= \hat{T}_e + \hat{V}_{ee} + \hat{V}_{ext} \\ &= -\frac{1}{2}\sum_{i=1}^{N}\nabla_i^2 + \sum_{i<j}^{N}\frac{1}{|\mathbf{r}_i - \mathbf{r}_j|} + \sum_{i=1}^{N} v\left(\mathbf{r}_i, \mathbf{R}\right) \end{aligned} \tag{2.2}$$

2.1.2 Kohn-Sham Theorem

Hohenberg and Kohn proved in 1964 that the ground state properties of a system are uniquely defined by the electron density $\rho(\mathbf{r})$ [38]. Thus, eq. (2.2) can be rewritten according to eq. (2.3) and the total energy is expressed by eq. (2.4) where $T\left[\rho_0\right]$ and $E_{\mathrm{c}}\left[\rho_0\right]$ are the kinetic energy and the classical Coulomb energy, respectively. $E_{\mathrm{nc}}\left[\rho_0\right]$ represents the non-classical electron-electron interactions.

$$E\left[\rho\right] = \langle\psi\left[\rho\right]|\hat{H}|\psi\left[\rho\right]\rangle \tag{2.3}$$

$$E_0 = T\left[\rho_0\right] + \int V_{ext}(\mathbf{r})dr + E_{\mathrm{c}}\left[\rho_0\right] + E_{\mathrm{nc}}\left[\rho_0\right] \tag{2.4}$$

With the electron density ρ, all properties of the N-electron system are defined. However, an explicit form of the functionals is missing.

The Kohn-Sham theorem (1965) gives a solution to the N-particle problem expressed in eq. (2.4). Kohn and Sham separated the many-body problem into a non-interacting expression of the kinetic energy $T_s\left[\rho\right]$, the long-range Coulomb interactions and a remaining exchange correlation energy which includes all missing effects. The advantage of this approach is that the exchange correlation part can be approximated as a local or nearly local functional of the electron density. The total electronic energy of eq. (2.4) within the Kohn-Sham approach transforms to eq. (2.5).

$$\begin{aligned} E_{\mathrm{KS}} &= T_s\left[\rho\right] + \int V_{ext}(\mathbf{r})\rho(\mathbf{r})d\mathbf{r} + E_{\mathrm{c}}\left[\rho\right] + E_{\mathrm{xc}}\left[\rho\right] \\ E_{\mathrm{xc}}\left[\rho\right] &= \langle\hat{T}\rangle - T_s\left[\rho\right] + \langle\hat{V}_{\mathrm{int}}\rangle - E_{\mathrm{c}} \end{aligned} \tag{2.5}$$

2.1.3 Exchange Correlation Functionals

The Kohn-Sham exchange and correlation functionals are expressed by eq. (2.5). Common approaches to approximate the exchange and correlation interaction in the Kohn-Sham equations are the local density approximation (LDA) and the

generalized gradient approximation (GGA). In LDA, E_{xc} is defined according to eq. (2.6). It assumes a homogeneous electron gas. In other words, the exchange correlation potential only depends on the local electron density $\rho(r)$.

$$E_{\mathrm{xc}}\left[\rho\right] = \int \rho\left(\mathbf{r}\right) \epsilon_{\mathrm{xc}}\left[\rho\left(\mathbf{r}\right)\right] d\mathbf{r} \tag{2.6}$$

In GGA approaches, the effect of the density gradient is included (eq. (2.7)). The exchange and correlation functional depends here additionally on the density gradient $\nabla\rho(r)$.

$$E_{\mathrm{xc}}\left[\rho\right] = \int F_{\mathrm{xc}}\left[\rho\left(\mathbf{r}\right), \nabla\rho\right] d\mathbf{r} \tag{2.7}$$

The Kohn-Sham method within the LDA or GGA approach for exchange and correlation exhibits serious deficiencies in the description of systems in which electrons are highly localized and interact strongly which is, for example, the case in rare earth elements (and their oxides). This mainly results from the introduction of an unphysical self-interaction in many exchange correlation functionals. Several approaches have been proposed and (with limitations) successfully used to overcome this problem. This include, for example, the DFT+U method [42] and hybrid DFT approaches [43, 44] which are discussed in the following sections.

2.1.4 DFT+U

The purpose of the DFT+U approach is to improve the localization of d and f orbitals in transition metal oxides and rare earth metal compounds, respectively [45]. This is realized by the introduction of an on-site Hubbard-like interaction (U potential) to the Hamiltonian (eq. (2.8)) [42, 45].

$$E_{\mathrm{DFT+U}}\left[\rho(\mathbf{r})\right] = E_{\mathrm{DFT}}\left[\rho\left(\mathbf{r}\right)\right] + E_U\left[\{n_m^{I\sigma}\}\right] - E_{dc}\left[\{n^{I\sigma}\}\right] \tag{2.8}$$

In eq. (2.8), $\rho(\mathbf{r})$ represents the electronic density and $n_m^{I\sigma}$ identify the occupation numbers of the atomic orbitals of atom I with the magnetic quantum number m. Since the E_{U} is added additionally, the interaction of the corresponding electrons arising from the DFT total energy E_{dc} has to be subtracted to remove the double counting.

The model Hamiltonian introducing a Hubbard U potential can be summarized according to eq. (2.9) [46, 47] based on the description of Anisimov et al. [42, 45] with U and J beeing the screened Hubbard on-site repulsion and exchange interaction parameter, respectively.

$$\hat{H} = \frac{U}{2} \sum_{m,m',\sigma} \hat{n}_{m,\sigma}\hat{n}_{m',-\sigma} + \frac{U-J}{2} \sum_{m\neq m'\sigma} \hat{n}_{m,\sigma}\hat{n}_{m',\sigma} \tag{2.9}$$

Considering the double counting term $E_{dc} = \frac{U}{2} \sum_I n^I \left(n^I - 1\right)$ finally leads to eq. (2.10) for the description of E_{DFT}.

$$E_{\mathrm{DFT+U}}\left[\rho(\mathbf{r})\right] = E_{\mathrm{DFT}}\left[\rho(\mathbf{r})\right] + \frac{U}{2} \sum_{I,\sigma} Tr\left[\mathbf{n}^{I\sigma}\left(1 - \mathbf{n}^{I\sigma}\right)\right] \tag{2.10}$$

The introduction of the U potential to the LDA and GGA approach leads to a shift of unoccupied orbitals by $\frac{U}{2}$ and of occupied ones by $-\frac{U}{2}$ enforcing the localization of the affected orbitals. This approach has been shown to successfully improve the computational results for systems such as NiO [45] and CoO [48] where standard DFT calculations predicted an incorrect metallic behavior.

The DFT+U method in CP2K is implemented accoridng to Dudarev et al. [27, 47].

2.1.5 Hybrid DFT

In the hybrid formalism, the exchange correlation energy of the Kohn-Sham equations (eq. (2.5)) includes a portion of exact Hartree-Fock exchange. This leads to a reduction of the self-interaction of electrons and results in an improved description of the electronic structure in strongly interacting systems.

Becke [43] has suggested to add exact exchange (E_x^{HF}) and density functional exchange correlation ($E_{\mathrm{xc}}^{\mathrm{DF}}$) in same parts (half and half) to the total exchange correlation energy (eq. (2.11)).

$$E_{\mathrm{xc}} = \frac{1}{2}\left(E_x^{\mathrm{HF}} - E_{\mathrm{xc}}^{\mathrm{DF}}\right) \tag{2.11}$$

More commonly used, however, is the B3LYP formalism which mixes exact exchange, the exchange functional of Becke (B88) and the Lee-Yang-Parr (LYP) [49] correlation (eq. (2.12)).

$$E_{\mathrm{xc}} = E_{\mathrm{xc}}^{\mathrm{DF}} + a_0\left(E_x^{\mathrm{HF}} - E_x^{\mathrm{DF}}\right) + a_x E_x^{\mathrm{Becke}} + a_c E_c \tag{2.12}$$

Another variation is the formalism of Perdew, Ernzerhof and Burke (PBE0) [44] who derived the mixing parameter theoretically, resulting in an exchange correlation energy with 25% of exact exchange (eq. (2.13)).

$$E_{\mathrm{xc}} = E_{\mathrm{xc}}^{\mathrm{DF}} + a_{pbe0}\left(E_x^{\mathrm{HF}} - E_x^{\mathrm{DF}}\right) \tag{2.13}$$

$$a_{pbe0} = \frac{1}{4} \tag{2.14}$$

Here, we basically used the hybrid approach of Perdew et al. [44]. However, the mixing parameter has been adjusted to the physical parameters of the system. In the case of CeO_2, we used a mixing parameter a_{pbe0}=0.2.

2.2 Methods

2.2.1 Wannier Functions

Wannier functions are widely used to determine electronic and dielectric properties in solid-state materials, equivalent to localized molecular orbitals used to describe chemical properties in molecular systems. Typically, in electronic structure calculations of periodic solids, eigenstates of the system are defined in the reciprocal space, in terms of a quantum number $\mathbf{k}$ for the crystal momentum and a band index n. The Wannier representation [50–52] translates the single-particle orbitals of the reciprocal space to real-space localized orbitals assigned to the lattice vector $\mathbf{R}$ where the orbital is localized [53].

Resulting from the periodic nature of solid state crystals, eigenstates of the Hamiltonian $\hat{H}$ are also eigenstates of the translation operator $\hat{T}_n$ (Bloch theorem). It follows that Wannier functions are Fourier transforms of the Bloch eigenstates according to eq. (2.15).

$$w_n\rangle = \frac{V_{\text{cell}}}{(2\pi)^3}\int_{\text{BZ}} \psi_{n\mathbf{k}}\rangle \mathrm{e}^{i\phi_n(\mathbf{k})-i\mathbf{k}\mathbf{R}} d\mathbf{k} = \frac{V_{\text{cell}}}{(2\pi)^3}\int_{\text{BZ}} \sum_{m=1}^{N} U_{mn}^{(\mathbf{k})}\psi_{m\mathbf{k}}\rangle \mathrm{e}^{-i\mathbf{k}\cdot\mathbf{R}} d\mathbf{k} \tag{2.15}$$

In this term, V_{cell} is the real-space primitive cell volume and $\psi_{m\mathbf{k}}$ are the Bloch orbitals of the system for different bands m.

The periodicity of the solid crystal introduces the arbitrary factor $\phi_n(\mathbf{k})$. As a result, the Wannier representation is non-unique. Several approaches exist to describe the latter. One of which is the use of a localization criterion (eq. (2.16)) introduced by Marzari et al. [54].

$$\Omega = \sum_n \left[\langle r^2\rangle_n - \langle \mathbf{r}\rangle_n^2\right] \tag{2.16}$$

Minimization of eq. (2.16) leads to maximally localized Wannier functions (MLWF). Ω can be separated in $\Omega_{\text{I}} + \tilde{\Omega}$ where Ω_{I} is invariant under arbitrary transformation of Bloch orbitals.

When the wavefunctions are only sampled at the Γ-point, MLWF are expressed by eq. (2.17).

$$\omega_n(\mathbf{r}) = \sum_m \left[\Pi_i \mathrm{e}^{-A^{(i)}}\right]_{mn} \psi_m(\mathbf{r}) \tag{2.17}$$

MLWF are a common strategy to investigate properties of solid state materials including the characterization of chemical bonds, electric polarization and orbital magnetization [55]. In general, the centers of Wannier functions can be regarded

as the position of electron pairs, thus characterizing chemical bonds or lone pairs. Analysis of Wannier functions gives information, for example, about polarization of electrons upon bond formation between multiple atoms.

2.2.2 Nudged Elastic Band Calculations

In order to determine chemical reaction kinetics, the total energy of the transition state is required. The transition state defines the highest energy point a system has to overcome to arrive from the initial to the final state. It is the maximum of the minimum energy path (MEP) of the reaction. Thus, the identification of the MEP is necessary to find the transition state. Optimization of the MEP, however, is not trivial. Several methods exist to sample the hyperspace of the potential energy. Here, the nudged elastic band (NEB) approach [56, 57] has been applied.

In the NEB formalism, the transition path is optimized between given initial and final states of a reaction. First, intermediate states or "images" are estimated between initial and final configuration. Often this is realized by linear interpolation of the coordinates of initial and final state. The energy of these states is then minimized considering both their internal potential energy and the interaction with their neighboring states. The interaction between states can be described as springs. It follows, that the objective function is a combination of the potential energy of the states and the contribution of such spring interactions to their adjacent states (eq. (2.18)).

$$S = \sum_{i=0}^{P} V\left(\mathbf{R}_i\right) + \sum_{i=0}^{P} \frac{Pk}{2} \left(\mathbf{R_i} - \mathbf{R_{i-1}}\right)^2 \tag{2.18}$$

In eq. (2.18), P indicates the number of examined states, $V\left(\mathbf{R}_i\right)$ the potential energy of state i, and k the spring constant. In the NEB method, forces acting on the examined states are separated into a component perpendicular and a component tangential to the MEP. Within this scheme, the spring constant k does not affect the shape of the MEP and can thus be used to control the resolution of the MEP.

2.2.3 Computational Details

All computations have been carried out with the Quickstep [58] module of the CP2K program package [59]. CP2K is a suite of programs implemented in Fortran 95 and developed to efficiently perform electronic structure and molecular dynamics simulations of solid state, liquid, molecular and biological systems. Density functional theory calculations in CP2K are based on the Gaussian and

plane waves (GPW) formalism allowing for quasi-linear scaling of computational performance with system size.

Valence electrons of involved atoms are treated explicitly whereas interactions of these electrons with the frozen core are described with norm-conserving pseudopotentials [60]. Details about the valence electrons considered and the adopted basis sets for specific atoms are described separately in each chapter. The utilized contracted Gaussian-type basis sets are optimized either in the atomic ground state of the atom [61] or in the electronic configuration that the atom exhibits in selected molecules [62]. The latter strategy will be identified as the Mol-Opt method in the following.

Depending on the basis sets used, the cutoff for auxiliary plane wave expansion of the charge density has been optimized. Obviously, the cutoff required for an accurate description of the electronic structure increased with increasing exponents of the basis set (sharpness). The applied values are separately documented in each chapter. Exchange correlation potentials are modeled within the generalized gradient approximation using the Perdew-Burke-Ernzerhof (PBE) functional [63]. The total energy of the systems has been optimized in self-consistent field (SCF) cycles using the orbital transformation method [64]. In order to optimize the geometry, the Broyden-Fletcher-Goldfarb-Shanno minimization algorithm (BFGS) [65–68] has been applied. The structures have been optimized until the forces were lower than $10^{-4} \frac{\text{Ha}}{\text{Bohr}}$ and the atomic displacements were smaller than $3 \cdot 10^{-3}$ Bohr.

3

The Rare Earth Metal Oxide CeO_2

3.1 Introduction

Rare earth metal oxides are highly interesting materials in numerous technological applications [69], including automobile exhaust-gas conversion [70], materials for optical glasses, ceramics and superconductors [71–73]. Recent studies have demonstrated the capability of rare earth metal oxides such as La_2O_3, Pr_2O_3 and Y_2O_3 [1, 2, 74] to be used as high performing gate insulators as a result of their high dielectric constants and excellent thermodynamic stability in contact with Si.

One of the most widely used and investigated rare earth metal oxides is CeO_2. Scientific interest in this particular metal oxide increased remarkably at the end of the last century with publications related to CeO_2 increasing from 29 in 1980 to 216 in 1994 [75]. Owing to its exceptional redox behavior ceria is in particular interesting in catalytic applications including the use in three-way-catalysts (TWC) in automobiles [70, 76, 77], for methane steam reforming in solid oxide fuel cells [78] or for CO_2 activation [79]. The unique capability of CeO_2 to readily release and take up oxygen results from the uncomplicated reduction of Ce^{4+} to Ce^{3+} and vice versa. Moreover, the fluorite structure of CeO_2 is maintained even after remarkable reduction [75], facilitating the reoxidation.

Experimental studies have proven the eligibility of CeO_2 for CO oxidation, soot combustion and as TWC [80, 81]. Doping of CeO_2 with zircona has resulted in a higher catalytic activity for such reactions [80, 81]. Enhanced oxygen mobility has been proposed as a possible explanation for the improved performance of the mixed metal oxide [80]. It has further been shown that small metal particles

supported on CeO_2 provide improved catalytic activity, for example, in the case of the water gas shift (WGS) reaction [82, 83], which can possibly be attributed to the interaction between metal and metal oxide. However, a detailed understanding of the underlying processes leading to enhanced performance of CeO_2-based catalysts is still missing. In this respect, computational analysis of the system is an important and necessary task for development and design of new catalysts.

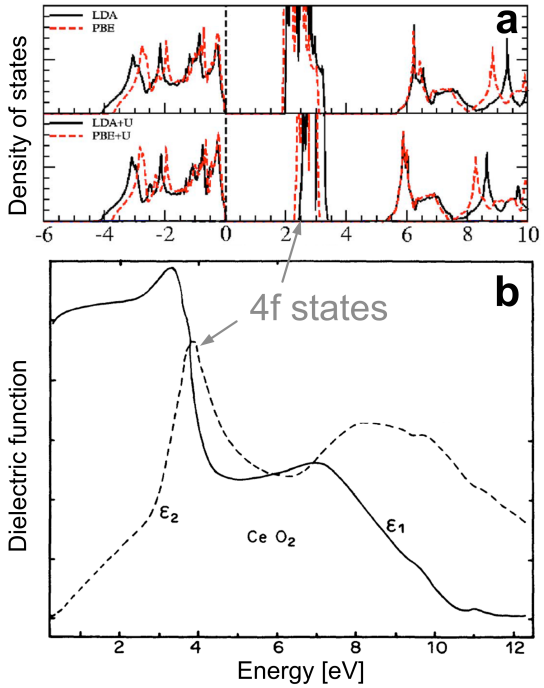

Figure 3.1: (a) Total density of states of CeO_2 from density functional theory calculations [30] and (b) dielectric function derived from optical reflectivity measurements [84]. Both standard DFT (a, top) and DFT+U (a, bottom) have been shown to be capable to capture the localized 4f states of Ce observed experimentally (b). Marginal differences occurred for the position of the 4f states between DFT and DFT+U calculations.

An accurate description of the CeO_2 crystal by first principles calculations, however, is challenging due to its strongly correlated electronic structure, mainly represented by highly localized empty 4f states of Ce. Experimentally, these states have been found to be 2.9-4.4 eV above the valence band [84–88]. For stoichiometric CeO_2, standard DFT has been shown to describe the electronic structure and the localized unoccupied 4f states in reasonable agreement (E=2.9 eV) [30] with experiments (Figure 3.1) [84, 87]. However, this is not the case for systems where reduction of Ce^{4+} to Ce^{3+} is involved, for example, in Ce_2O_3 or reduced

CeO_2 surfaces [29, 30]. Hybrid DFT as well as DFT+U are possible solutions for an improved description of such systems [30, 88–90].

To minimize errors in the description of the properties of CeO_2, here, bulk and surface properties of CeO_2 have been investigated carefully using different pseudopotentials (q12 and q30) and different computational methods, namely standard DFT, DFT+U and PBE0 [44].

3.2 Methods

Pseudopotentials and Basis Sets Standard DFT calculations of this chapter have been carried out according to section 2.2.3. For oxygen atoms, six electrons, namely 2s and 2p, are treated explicitly in the valence shell. The interaction with the frozen core is described by a GTH-type pseudopotential, denominated as GTH-PBE-q6 in the CP2K repository [59]. Two different kinds of pseudopotentials have been utilized for Ce. In the first one, twelve electrons (5s, 5p, 5d, 4f and 6s), are treated explicitly in the valence shell, referred to as q12 in the following. For the second one, additionally 4s, 4p and 4d electrons are considered in the valence shell increasing the number of explicitly calculated electrons to 30. The latter is denominated as q30.

Several tests have been carried out using both triple- and double-ζ valence basis sets for oxygen optimized according to the Mol-Opt method [62]. Only marginal differences have been observed between the two. Thus, results are shown here only for a selected choice of O-basis sets. When using the q12 pseudopotential for Ce, a triple-ζ valence plus double polarization basis set has been adopted for O. In the interest of computational efficiency, a double-ζ valence plus polarization basis set has been adopted in simulations with the q30 pseudopotential of Ce. The double- and triple-ζ basis sets used here are denominated as DZVP-MOLOPT-GTH and TZV2P-MOLOPT-GTH, respectively, in the CP2K repository [59].

Basis sets for Ce have been optimized in the atomic ground state using the atomic calculations in CP2K. For q12, the optimized double-ζ basis set (DZV-q12) has six contraction coefficients and provides three primitive functions for s and p electrons and two primitives for d and f electrons. Different basis sets have been optimized for the q30 pseudopotential and evaluated on the CeO_2 molecule. The results are shown in Table 3.1. The optimized double-ζ basis set used for the q30 pseudopotential (DZV-GTH-q30-3) has nine coefficients with four primitives for s and p electrons and three and two for d and f electrons, respectively.

The cutoff for the auxiliary plane wave expansion of the electronic density has been set to 1000 Ry and 1200 Ry for calculations with the q12 and q30 pseudopotential, respectively.

Table 3.1: Geometrical (Ce-O bond length $d_{\mathrm{Ce-O}}$ and O-Ce-O angle α) properties and total energy E_{tot} of the CeO_2 molecule in its ground state calculated with different basis sets. n_{coeff} indicates the number of coefficients of the basis set. Based on its accuracy and computational costs (calculated on 8 processors), the "DZV-GTH-q30-3" is being used for further calculations of the CeO_2 crystal.

Basis Set	n_{coeff}	$d_{\mathrm{Ce-O}}$ [Å]	α [°]	E_{tot} [Ha]	SCF time [sec]
SZV-GTH-q30	6	1.866	180	-501.19	33.8
SZV-GTH-q30-2	10	1.849	180	-501.33	34.4
SZV-GTH-q30-3	9	1.850	180	-501.30	34.6
DZV-GTH-q30	6	1.819	180	-501.23	34.2
DZV-GTH-q30-2	10	1.833	180	-501.34	36.5
DZV-GTH-q30-3	9	1.830	180	-501.32	35.7

Extended DFT Calculations DFT calculations have been extended with a Hubbard-U potential (DFT+U) and consideration of exact exchange in the framework of hybrid PBE0 [44] calculations. The U potential as been used on the f orbitals of Ce atoms and has been varied from 0 to 16 eV. If not stated else the U potential used in DFT+U calculations with the q12 pseudopotential has been set to 16 eV. When using the q30, the U potential has been set to 4.5 eV.

In PBE0 calculations, an exact exchange of 20% has been introduced. For the results reported here special basis sets according to Auxiliary Density Matrix Method (ADMM) [91] have been used.

Bulk and Surface Properties The stoichiometric CeO_2 exhibits the fluorite (face-centered cubic, $Fm\bar{3}m$) crystal structure. All atomic positions in the fluorite structure are defined by its symmetry and the lattice parameter a (Figure 3.2).

The progression of the total energy E as a function of the lattice parameter (crystal volume V) can be described according to the Murnaghan equation of state (eq. (3.1)) [92], where V_0 and E_0 are the equilibrium volume and total energy, respectively, and B_0 and B_0' indicate the bulk modulus and its pressure derivative.

$$E = E_0 + \frac{B_0 V}{B_0'}\left[\frac{(V_0/V)^{B_0'}}{B_0' - 1} + 1\right] - \frac{V_0 B_0}{B_0' - 1} \tag{3.1}$$

The Murnaghan equation of state is used in the following to determine the

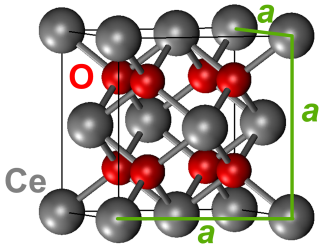

Figure 3.2: Fluorite unit cell of CeO_2. Atomic positions of Ce (grey spheres) and O (red spheres) are fully constraint by its space group ($Fm\bar{3}m$) symmetry and the lattice parameter a.

bulk modulus and the equilibrium lattice parameter of CeO_2 calculated with different computational settings.

Exposed crystallographic planes (surfaces) of CeO_2 have been shown computationally to be most stable in the order (111)>(110)>(100) [93]. This is in agreement with experiments applying x-ray photoelectron spectroscopy (XPS) and low-energy electron diffraction (LEED) techniques showing the (111) surface to be most stable [94]. Based on this, surface properties have been investigated here of the (111) surface of CeO_2 focusing on relaxation of surface atoms and the stability (surface energy) of CeO_2(111). The surface energy E_S has been calculated according to eq. (3.2), where E_{bulk} and E_{surf} are the total energy of the bulk CeO_2 and the CeO_2 surface slab, respectively, and A is the exposed surface area on one side of the slab [95].

$$E_S = \frac{E_{surf} - E_{bulk}}{2A} \tag{3.2}$$

In the calculations performed here, the slabs of bulk and surface CeO_2 consist of the same amount of atoms.

3.3 Bulk Properties

An accurate description of the electronic structure of CeO_2 is problematic within the framework of DFT calculations as it has been described in the introduction (section 3.1). Thus, the electronic structure of bulk CeO_2 including analysis of the density of states (DOS), bulk modulus and equilibrium lattice parameters has been carefully evaluated.

Density of States The DOS projected on the Ce and O atoms, respectively, calculated with the q12 pseudopotential and different DFT-based methods, are

shown in Figure 3.3. The CeO_2 bulk has been simulated with DFT+U (U=16 eV), PBE0 (20% exact exchange) and standard DFT using the PBE exchange correlation functional. If not stated differently, the results in the following have been obtained with spin-unrestricted calculations. The valence band extends to ca. 4 eV below the highest occupied state (0 eV) and is mostly populated by O-2p orbitals (Figure 3.4). Its structure is comparable between all methods and similar to previous DFT studies [30, 96] (Figure 3.1).

Remarkable variances in the projected density of states (PDOS) between the different methods, however, is observed in the unoccupied states. Most critical for the description of CeO_2 in this respect is the accurate representation of the characteristic peak of Ce_{4f} states located in between the fundamental band gap (between O_{2p} and Ce_{5d}). Experimental studies have yielded a value of 6.0 eV for the fundamental band gap [87] whereas the empty 4f states have been measured to be 2.6-3.9 eV above the valence band [87, 88]. In the calculations conducted here using DFT+U with U=16 eV, these states are sharply localized, however, at significantly higher energies than experiments predict. Resulting from the high value of U, these 4f states are shifted to 6 eV above the valence band and they are found to be at even higher energies than the Ce_{5d} states (4 eV above the valence band). A reasonable electronic structure is found utilizing the PBE0 method with 20% of exact exchange. Here, the Ce_{4f} states are located 4 eV above the valence band and the Ce_{5d} states are located 7 eV above the valence band (Figure 3.3).

A similar structure is obtained with standard DFT calculations and restricted spin population (Figure 3.5). The fundamental band gap results in 5.95 eV while the Ce_{4f} states are highly localized at 2.0 eV above the valence band. However, when the spin population is allowed to relax (UKS) and the symmetry of the spin-density has been broken initially, the system terminates in a spin-polarized state. This leads to a delocalization of the empty 4f states and a decrease of the O_{2p}/Ce_{5d} band gap to 0.7 eV (Figure 3.3, bottom and Figure 3.5).

For further investigation, the DOS has been projected additionally on the angular momenta (s-, p-, d- and f-orbitals) of one Ce atom (Figure 3.6). Using UKS, f-type orbitals in the valence band are partially occupied in the α-spin leading to a polarization of the empty f-type orbitals in the α-channel. As a result, the empty 4f states delocalize and shift to lower energies (0.41 eV above the valence band). Furthermore, the f-type orbitals in the valence band are less occupied with β-spin electrons than in the restricted calculation leading to a shift of the empty 4f states to higher energies (4 eV above the valence band). These specific features of the electronic structure in each of the two spin-channels is observed in the respective other channel as well for different Ce atoms. Summation of the PDOS of all atoms of the system thus results in a spread of 4f states (from 0.4 - 4 eV above the valence band).

Bulk Modulus and Lattice Parameters The progression of the total energy E as a function of the lattice parameter (crystal volume V) can be described according to the Murnaghan equation of state (eq. (3.1)) [92].

Figure 3.7 shows the total energy E as a function of the crystal volume V calculated here with different methods and pseudopotentials. A non-physical behavior is observed when the CeO_2 bulk is simulated by standard DFT using the q12 pseudopotential similar to the behavior of the PDOS (Figure 3.5). The integrated spin-density decreases rapidly with the lattice parameter leading to lower energies at larger a.

Fitting the total energy to the Murnaghan equation of states (eq. (3.1)) a lattice parameter a of 5.57 Å is obtained for simulations using UKS calculations with the q12 pseudopotential. This is by 3% larger than the experimental lattice parameter (5.41 Å [85]). Furthermore, the bulk modulus B_0 obtained from the Murnaghan equation (95 GPa) underestimates the experimental value (220 GPa [85]) by 57% (see Table 3.2).

A better description of the bulk structure of CeO_2 has been obtained with RKS where the lattice structure is not influenced by spin polarization. The lattice parameter is found to be 5.48 Å in reasonable agreement with experiments and previous calculations (5.37-5.48 Å [96–98], Table 3.2). With these simulations, the underestimation of the bulk modulus can be reduced to 21%.

When using unrestricted spin calculations, the accuracy of the crystal structure could be improved applying the DFT+U method. Here, the rapid decrease in energy resulting from the evolution of a spin-polarized electronic structure is shifted to higher a. At a U value of 16 eV, the drifting into a spin-polarized state could be omitted resulting in a lattice parameter of a=5.46 Å being again in good agreement (+0.9%) with previous results (Table 3.2 [85, 96–98]).

Considering more valence electrons (q30 pseudopotential), the discrepancy between standard DFT calculations and the extended DFT+U method can be eliminated. Here, no spin-polarization is observed when asymmetric spin population is allowed and the equilibrium lattice parameter a is found to be in close agreement to previous results (see Table 3.2) for both standard DFT (5.42 eV) and DFT+U (5.41 eV) using a U value of 4.5 eV.

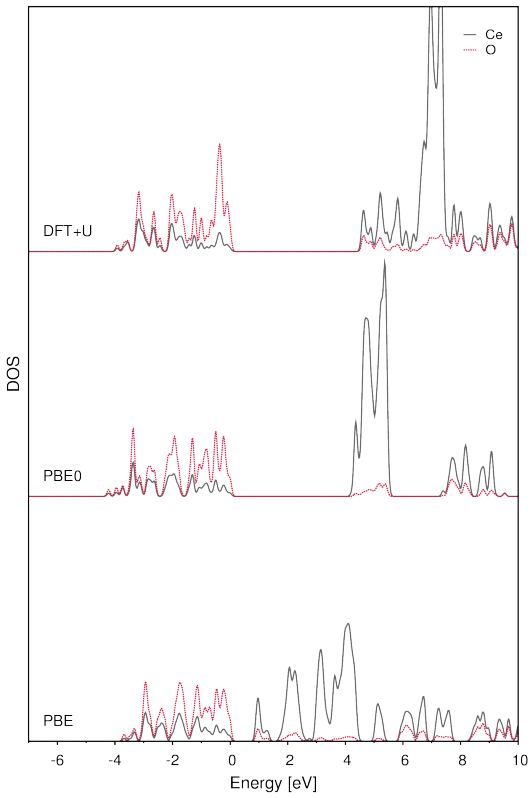

Figure 3.3: PDOS of bulk CeO_2 projected on the orbitals of Ce and O atom using extended DFT (DFT+U), hybrid DFT (PBE0) and standard DFT (PBE) calculations. Unrestricted spin-population (UKS) has been considered with all methods and the PBE exchange correlation functional has been used. In the DFT+U scheme, a U potential of 16 eV has been utilized. An exact exchange of 20% has been considered for PBE0 calculations.

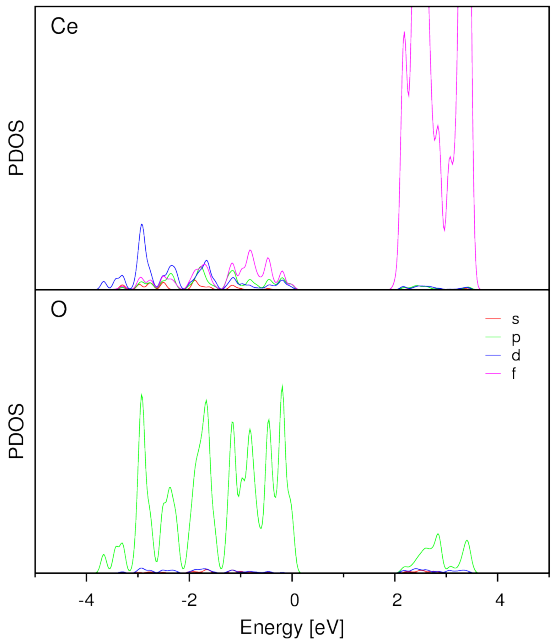

Figure 3.4: PDOS of bulk CeO_2 projected on the angular momentum of the orbitals of Ce and O atom using standard DFT (PBE) calculations.

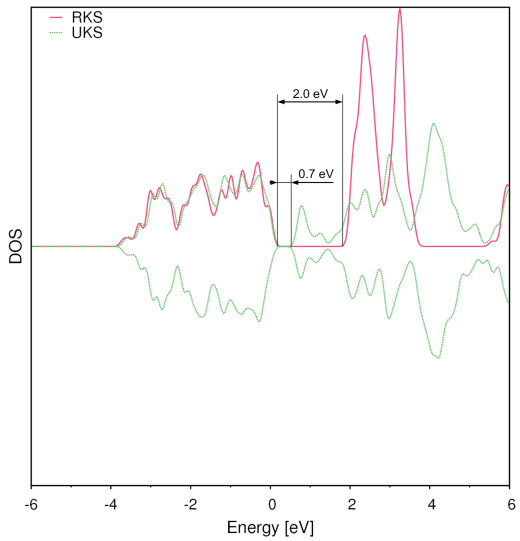

Figure 3.5: Total DOS of bulk CeO_2 obtained with the q12 pseudopotential and RKS (red) and UKS (green) calculations.

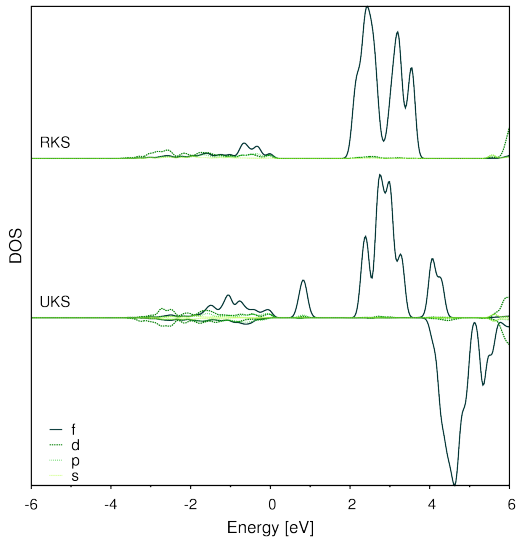

Figure 3.6: PDOS of bulk CeO_2 projected on s-, p-, d- and f-type orbitals of one Ce atom for RKS and UKS simulations. Partial population of f-type orbitals in the α-spin leads to a delocalization of empty Ce_{4f} orbitals.

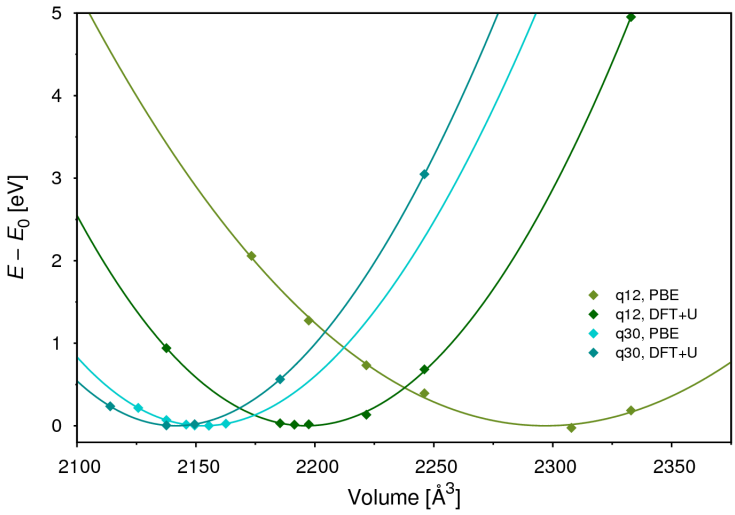

Figure 3.7: Difference between total energy (E) and energy at the equilibrium volume (E_0) as a function of the unit cell volume. Artificial spin-polarization resulted in a non-physical behavior of the energy of the system as a function of its volume and an overestimated equilibrium lattice parameter (q12, PBE: a=5.54 Å) when using the q12 pseudopotential. Using DFT+U (U=16 eV), this artifact could be eliminated resulting in a lattice parameter a=5.46 Å. Using the q30 pseudopotential, only marginal differences have been observed for the energy to volume behavior between standard DFT (a=5.42 Å) and DFT+U (a=5.41 Å) using a U value of 4.5 eV.

Table 3.2: Bulk modulus B_0 and lattice parameter a of stoichiometric bulk CeO_2 and surface energy E_S of its (111) surface. RKS indicates spin-restricted calculations, no specification indicates UKS calculations.

Method	B_0 [GPa]	B_0'	a [Å]	$E_{O_{2p}-Ce_{4f}}$ [eV]	$E_{O_{2p}-Ce_{5d}}$[eV]	E_S [J/m^2]	Reference
PBE (RKS)	174	4.6	5.48	2.03	5.95	0.73	this work
PBE	95	0.72	5.75	0.40	5.61	-	this work
DFT+U	194	1.01	5.46	5.91	4.65	0.97	this work
PBE0	202	2.01	5.42	4.22	7.40	0.88	this work
PBE	195	3.97	5.42	2.38	6.05	0.69	this work
DFT+U	208	4.47	5.41	3.02	5.66	0.76	this work
GGA (PW91)	172	-	5.47	1.00	5.00	0.68	[97]
LDA	-	-	5.37	-	-	1.04	[98]
GGA+U (PBE)	-	-	5.48	-	-	0.72	[96]
exp.	220	4.4	5.41	2.9-4.4	6-8	-	[84–88]

q12

q30

3.4 Surface Properties

Surface Energy The surface energy required to form the (111) surface of CeO_2 has been calculated using both q12 and q30 pseudopotentials with different methods (DFT, DFT+U and PBE0) and the results are summarized in Table 3.2. Despite the non-physical representation of virtual states with the q12 pseudopotential (section 3.3) the calculated surface energy is in fairly good agreement with previous results (Table 3.2). Simulations utilizing the q12 pseudopotentials (RKS) yield surface energies of 0.73-0.78 J/m^2 depending on the slab surface, thickness and vacuum added between periodic images of the slab. It converges towards a value of 0.73 ± 0.01 J/m^2 using a p(3x3) surface, a slab with six O-Ce-O trilayers and a vacuum of 10 Å. Applying the q30 pseudopotential, a surface energy of 0.69 ± 0.07 J/m^2 has been calculated using the p(3x3) surface, six trilayers and a vacuum of 15 Å.

The basis set superposition error (BSSE) has been determined simulating the surface with the same amount of so-called "ghost-atoms" as there were "real" atoms in the bulk calculation. The purpose of "ghost-atoms" is to provide the basis sets for surface calculation that are by default present in bulk calculation. The BSSE for a p(3x3) surface consisting of six O-Ce-O trilayers when all layers are allowed to relax is calculated to be 0.07 J/m^2 with the q12 and 0.05 J/m^2 with the q30 pseudopotential.

Surface Relaxation Formation of the CeO_2(111) surface has been been shown to have little effect on the relaxation of surface atoms [96–98]. This is verified by our calculations where a displacement of less than 0.1 Å in [111] direction is found for all surface atoms. Figure 3.8 shows the change in distance between adjacent layers upon creation of the (111) surface. Surface relaxation obtained here using the q12 (RKS) is in very good agreement with previous calculations by Skorodumova et al. [98]. The first layer of O atoms is shown to slightly move towards the surface. Ce atoms, on the other hand, rather move outwards. Subsequent layers of both Ce and O atoms only show marginal changes with respect to their bulk position. Similar results are obtained using the q30 pseudopotential (Figure 3.8).

3.5 Surface Vacancies

Formation of O vacancies on the CeO_2 surface is crucial using DFT calculations since it leads to the reduction of specific Ce atoms to Ce^{3+}. Reduction of Ce involves the occupation of the 4f orbitals that are unoccupied in stoichiometric CeO_2. Using standard DFT [99], this has been shown to evolve into a metallic

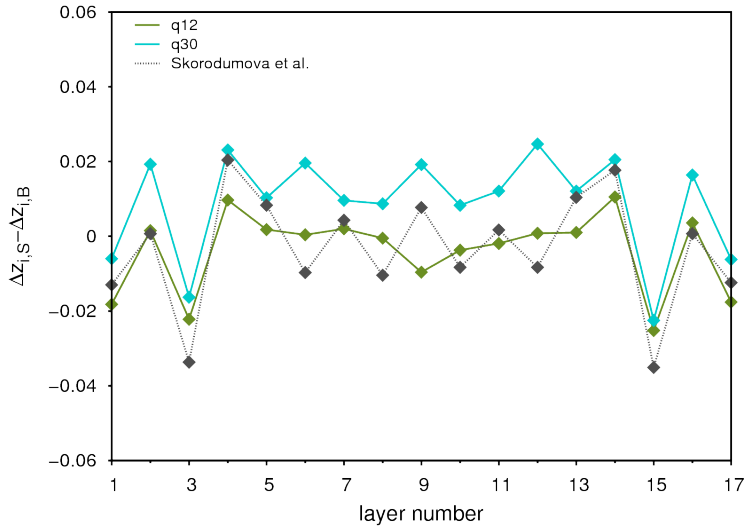

Figure 3.8: Changes in interplanar spacings due to the relaxation of the (111) surface of CeO_2 calculated here (solid line) with both the q12 and q30 pseudopotential compared to previous calculations (dotted line) [98]. $\Delta z_{i,S}$ indicates the interplanar spacing between atomic layers i and i+1 of the surface and $\Delta z_{i,B}$ indicates the interplanar spacing in the bulk.

behavior of the reduced CeO_2 surface in disagreement with experimental results [86, 100, 101]. This artifact can be overcome using DFT+U calculations [99, 102]. Gironccoli et al. described a linear response method to determine the value of U [103]. Using DFT+U calculations with U=5 eV the formation of a O vacancies in the surface layer has been described previously to be accompanied by the occupation of 4f states 0.9 eV above the valence band [97]. Here, the use of standard DFT (U=0 eV) calculations with the q30 pseudopotential resulted in a metallic description of the (partially) reduced CeO_2 surface (Figure 3.9) demonstrating the deficiencies of this method in agreement with previous DFT studies [99]. Additional electrons provided by oxygen vacancies occupy the 4f orbitals of Ce electrons 2.27 eV above the valence band. These states are found on the lower edge of the conduction band resulting in a metallic behavior of the reduced CeO_2(111) surface. The effect of the value of U on the density of states upon formation of a surface O vacancy (1/9 ML) has been investigated for U values ranging from 0 to 5 eV (Figure 3.9). Increasing the value of U leads to a shift of occupied 4f states (Ce^{3+} atoms) to lower energies. Using a U value of 4.5 eV, occupied 4f states of Ce^{3+} atoms are found 1.48 eV above the surface in agreement with experimental results (1-1.4 eV [104]).

The vacancy formation enthalpy E_{vac} has been calculated according to eq. (3.3),

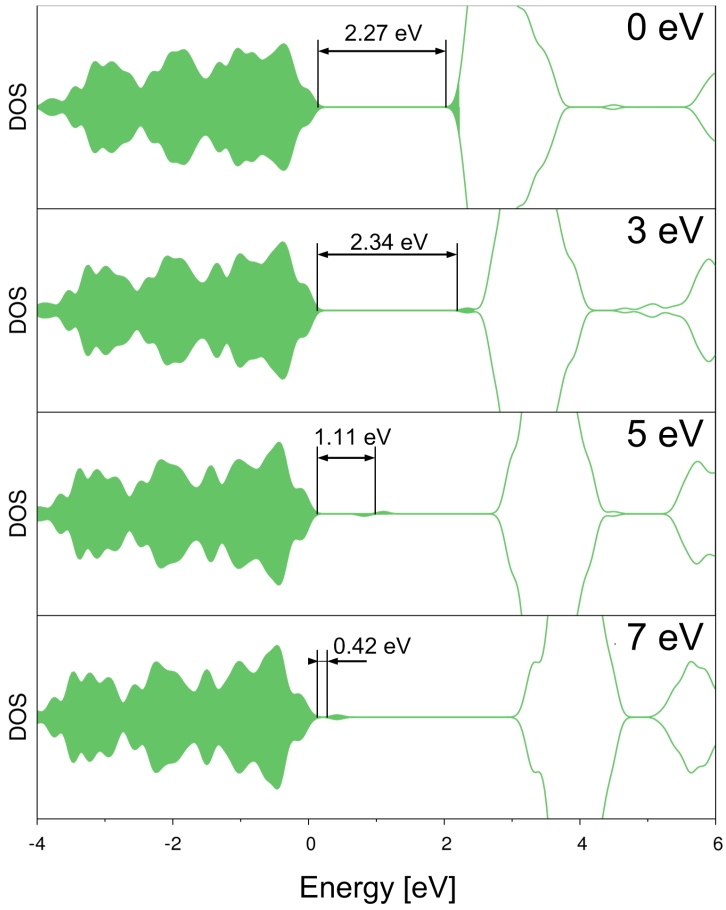

Figure 3.9: DOS of reduced CeO_2 simulated with DFT+U with U ranging from 0 to 7 eV. Occupied 4f states of Ce^{3+} move closer to the valence band with increasing U.

where E_{CeO_2} and $E_{CeO_{(2-x)}}$ signify the total energy of the stoichiometric and reduced surface, respectively, and $E_{O_2,g}$ is the gas phase energy of an oxygen molecule in the triplet state. N_{vac} gives the number of vacancies.

$$E_{vac} = \frac{E_{CeO_{(2-x)}} + \frac{x}{2}E_{O_2,g} - E_{CeO_2}}{N_{vac}} \tag{3.3}$$

The energy required to create O vacancies in the surface layer has been calculated to be 3.67 and 3.37 eV with standard DFT and DFT+U calculations, respectively, in good agreement with DFT calculations performed previously (3.39-3.98 eV [93], Table 3.3). Other calculations utilizing the DFT+U method have reported lower enthalpies for surface vacancy formation (2.15-2.92 eV [96, 105]).

Table 3.3: Vacancy formation energy of surface (E_{vac}) and subsurface ($E_{vac,sub}$) vacancies calculated here and in previous DFT studies [93, 96, 105, 106].

Method	E_{vac}	$E_{vac,sub}$	Reference
PBE	3.67	-	this work
DFT+U	3.37	3.74	this work
GGA+U	2.15	1.89	[96]
LDA+U	2.92	2.95	[96]
GGA+U	2.34-2.50	1.87-2.40	[105]
PBE	3.39-3.98	3.21-3.80	[93]
exp.	4.7-5.0	-	[106]

However, the energies calculated here, are closer to what has been measured experimentally (4.7-5.0 eV [106]). Similarly, the enthalpy of formation of subsurface vacancies (3.74 eV) is overestimated with respect to previous calculations using the DFT+U method (1.87-2.95 eV [96, 105]). Furthermore, here, we have found subsurface vacancies to be less stable compared to surface vacancies. Previous computational studies showed the contrary [93, 96, 105]. A possible explanation of this discrepancy between ours and previous calculations is the location of Ce^{3+} sites. This has been shown to affect the stability of O vacancies by up to 0.53 eV [105].

A detailed study on the location of Ce^{3+} sites, however, is tedious and was not feasible in this study. Nevertheless, we have simulated specific electronic configurations for surface O vacancies and have found similar results as have been calculated previously. The most stable configuration has been found when Ce^{3+} localize on next-nearest neighbor (NNN) positions (Figure 3.10). The divergence of reduced Ce atoms away from the vacancy is found to stabilize the surface by 0.43 eV. A similar trend has been found previously where the divergence of one Ce^{3+} site away from the vacancy has been found to stabilize the system by 0.16 eV compared to the nearest neighbor (NN) configuration (Figure 3.10).

3.6 Conclusions

Different DFT-based methods, namely standard DFT, DFT+U and PBE0, have been utilized to characterize CeO_2 bulk and its (111) surface. For Ce atoms, either twelve or 30 electrons have been considered in the valence shell. An accurate description of the unoccupied 4f-orbitals is the most crucial task when

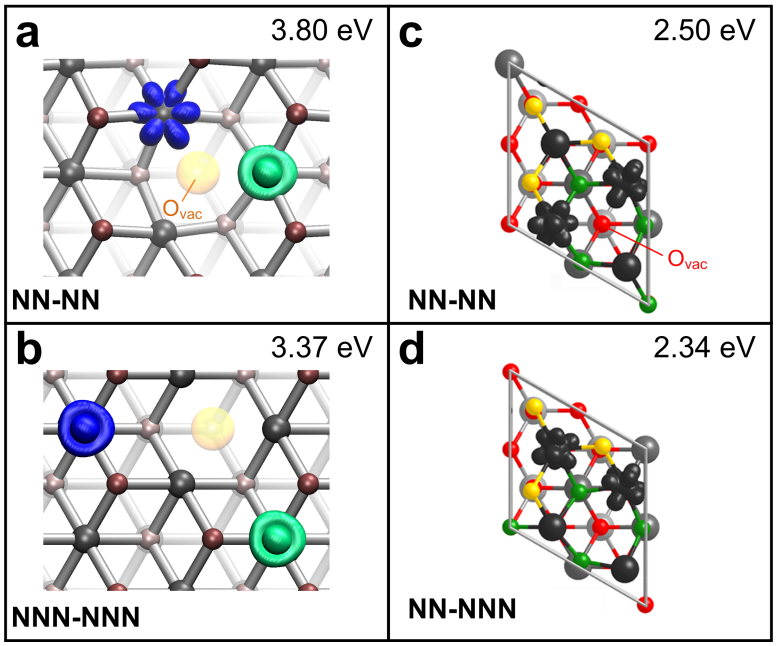

Figure 3.10: Isosurfaces of the spin-density resulting from oxygen vacancy formation in the surface layer of CeO_2 calculated in (a,b) this and (c,d) previous studies [105]. The system has been found to stabilize when reduced Ce-sites drift away from the vacancy. NN indicates a nearest neighbor position and NNN a next-nearest neighbor position.

using ab initio calculations to describe the electronic structure of CeO_2. Using spin-restricted standard DFT calculations and a pseudopotential that considers twelve valence electrons (q12) the density of states of stoichiometric CeO_2 could be accurately described. However, when the spin is allowed to relax (UKS), an asymmetric occupation of f-type orbitals in the valence band is found to be the most stable state leading to a delocalization of the unoccupied 4f states of Ce and an unphysical behavior of the bulk modulus, equilibrium lattice parameter and surface relaxation of CeO_2. This problem can be overcome using the DFT+U approach with a U value of 16 eV or the PBE0 method considering an exact exchange of 20%. Another solution has been found when using a pseudopotential for 30 valence electrons. In this case, even unrestricted standard DFT calculations are capable to accurately describe the electronic structure of stoichiometric CeO_2. Structural parameters such as bulk modulus (195 GPa), equilibrium lattice parameter (5.42 Å) and surface relaxation (<0.1 Å) have been found to be in reasonable agreement with previous calculations and experiments [85, 86, 96–98].

The surface energy has been found to converge to a value of 0.73±0.01 J/m^2

using a p(3x3) surface slab with six O-Ce-O trilayers and a vacuum of 10 Å with the q12 pseudopotential. Considering 30 valence electrons (q30 pseudopotential) for the simulation of the same slab with 15 Å vacuum, a surface energy of 0.69 J/m^2 is calculated. The BSSE has shown minor effects on the surface energy. With the q12 and the q30 pseudopotential, the BSSE has been calculated to be 0.07 and 0.05 J/m^2, respectively.

Only little reconstruction of slab atoms compared to their bulk equilibrium position has been observed when the (111) crystallographic plane of CeO_2 is exposed (<0.1 Å) in agreement with previous calculations [96, 98]. Most pronounced is the contraction of adjacent O layers of the surface and subsurface O-Ce-O trilayer (-0.02 Å).

Surface vacancy formation (of O atoms) as been investigated with the q30 pseudopotential focusing on the effect of the Hubbard U value in the DFT+U formalism. For U=0 eV (standard DFT), excess electrons, stemming from the removed surface O atoms, occupy Ce_{4f} states leading to a metallic description of the electronic structure. Increasing U, these occupied states shift to lower energies. Using a U value of 4.5 eV, the electronic structure of reduced CeO_2 has been described in good agreement with experimental results showing a gap between valence band and occupied 4f states and between occupied and unoccupied 4f states of 1.48 eV and 1.37 eV, respectively.

4

Adsorption of Ni Clusters on $CeO_2(111)$

4.1 Introduction

Combined metal - metal oxide systems are important materials for numerous technological applications such as microelectronics, photovoltaics, gas sensors and in particular in oxide-supported metal catalysts [107]. In this respect, enhanced catalytic activity of the water gas shift reaction ($CO + H_2O \rightarrow CO_2 + H_2$) on Pt has been observed when Pt particles are deposited on metal oxides such as Al_2O_3, CeO_2 and TiO_2 [108–110]. Pt nanoparticles on ceria have also been shown to assist the oxygen transfer in the CeO_2 support [111] leading to improved catalytic activation of CO oxidation.

Another interesting oxide-supported metal system is Ni on CeO_2. In fact, ceria-supported Ni particles have shown improved activity for the methanation of CO_2 [112]. More recently, the catalytic activity of Ni-CeO_2 could even be increased by changing the morphology of Ni from nanopolyhedra to nanorods [113].

Several reasons are proposed for the improved catalytic activity of metal oxide supported metal clusters. These include the supply of reactants through surface diffusion, the change of electronic properties and the modified morphology of the metal clusters compared to extended surfaces [114]. In particular, the morphology of the metal is decisive for the catalyst's activity. In this respect, it is known that the binding energy of reactants, such as CO in the case of the WGS reaction, is increased on a more open structure where edges and corners are present leading to higher reaction rates of, for example, CO oxidation [114]. The choice and structure of the metal oxide support can directly control the morphology of the

deposited metal particles [115]. Nevertheless, the changes in electronic structure can also lead to significant alteration in the catalytic performance of the oxide-metal system. The effect of so-called electronic metal support interactions (EMSI) has been discussed in detail recently [116].

Reliable production of metal/metal-oxide systems with controlled morphological properties, however, is difficult. Furthermore, experimental tools such as scanning tunneling microscopy (STM) or atomic force microscopy (AFM) utilized to characterize these materials are limited in temperature and pressure. In this regard, ab initio simulations offer a great possibility to study the formation and morphology of (small) metal structures on metal oxides and, in addition, describe the electronic structure of such systems providing insight in the underlying driving mechanism of a specific reaction.

In fact, DFT calculations revealed a facilitated cleavage of O-H on the corner atoms of small Pt particles on CeO_2(111) resulting in an improved catalytic activity of the Pt/CeO_2 system for the dissociation of H_2O in agreement with experiments [117]. Another theoretical study has investigated the interaction of Ni atoms with CeO_2- ZrO_2 surfaces [118]. Previously, experiments have shown higher catalytic activities of Ni when deposited on the CeO_2- ZrO_2 solid solution compared to Ni particles deposited on the pure oxides [119] attributed to their higher surface area and the strong metal-support interaction (SMSI). This has been confirmed by DFT calculations indicating a stronger interaction between Ni and the support on Zr sites [118].

Nevertheless, Ni particles on pure CeO_2 have been shown to be a promising catalyst for several reactions such as the WGS reaction [120, 121], CO methanation [121] and steam reforming of ethanol [122–125]. Characterization of the Ni/CeO_2 system using STM measurements displayed Ni to form particles on the (111) surface of CeO_{1-x} with a particle size of 1.5 to 4.5 nm depending on the stoichiometry and the annealing temperature [126].

However, a consistent description of atomic and multiatomic Ni on CeO_2 based on ab initio calculations is still missing. Using DFT calculations with the PW exchange-correlation functional [127], it has been shown that Ni atoms are most stable on top of surface O atoms of CeO_2(111) [128]. The contrary has been observed by Lu et al. who found hollow and bridge O sites to be favored over O top sites for Ni adsorption on CeO_2(111) [129]. A possible explanation for this discrepancy is the utilization of a different description of the electronic structure of Ce. Chafi et al. considered 6s, 5d and 4f electrons in the Ce valence shell [128] whereas Lu et al. additionally included 5s and 5p electrons [129]. The different results could also arise from different locations of excess electrons in CeO_2. Recently, it has been shown that the position of reduced Ce sites (Ce^{3+}) can affect the Ni binding energy by up to 0.5 eV [130].

Here, we have investigated the stability and geometry of Ni clusters in the gas

phase. Subsequently, adsorption of Ni clusters on CeO_2(111) has been simulated and analyzed in terms of energetic (binding energy), structural (Ni-Ni bond length and gyration radius) and electronic (density of states) properties. Ni clusters have been investigated up to a size of 13 atoms.

4.2 Methods

The calculations of this chapter have been carried out using the q30 pseudopotential for Ce (see section 3.2) considering 30 electrons in the valence shell. A double-ζ basis set has been adopted to describe the valence electrons, optimized in the atomic ground state. Six and 18 electrons have been treated explicitly for O and Ni atoms, respectively. Mol-Opt double-ζ basis sets [62] with polarization have been used for the latter atoms, identified as DZVP-MOLOPT-GTH (oxygen) and DZVP-MOLOPT-SR-GTH (nickel) in the CP2K repository [59]. A cutoff of 1200 Ry has been used for the auxiliary plane wave expansion of the charge density. For all calculations, the DFT+U method has been adopted using a U value of 4.5 eV on the 4f electrons of Ce.

The optimized lattice parameter of CeO_2 with these specifications has been calculated to be 5.41 Å in excellent agreement with experiments (5.41 Å [84–88]). The CeO_2(111) surface has been simulated using a slab of six O-Ce-O trilayers of which the top three have been allowed to relax and the bottom three have been fixed in their bulk position. To avoid interactions with its periodic images, a vacuum of 15 Å has been introduced along the [111] direction. A surface dimension of p(3x3) has been used corresponding to a total of nine active surface Ce sites in the simulation cell.

Simulation of Ni clusters in the gas phase consisting of two to ten atoms has been carried out in a periodically repeated box of 15x15x15 Å. The energy of formation E_F of such clusters has been calculated according to eq. (4.1), where n_Ni defines the number of Ni atoms in the cluster and E_cluster and $E_\mathrm{Ni,g}$ refer to the total energy of the Ni cluster and the Ni atom in the gas phase (triplet), respectively. A negative value of E_F thus indicates the cluster formation to be an exothermic reaction.

$$E_\mathrm{F} = \frac{E_\mathrm{cluster} - n_\mathrm{Ni} \cdot E_\mathrm{Ni,g}}{n_\mathrm{Ni}} \tag{4.1}$$

The binding energy of Ni clusters on CeO_2(111) has been calculated in analogy to the formation energy according to eq. (4.2), where $E_{\mathrm{slab}+n_\mathrm{Ni}}$ is the total energy of the CeO_2(111) slab with an adsorbed Ni cluster containing n_Ni atoms. E_slab refers to the total energy of the clean CeO_2(111) surface.

$$E_{\mathrm{B}} = \frac{E_{\mathrm{slab}+n_{\mathrm{Ni}}} - (n_{\mathrm{Ni}} \cdot E_{\mathrm{Ni}} - E_{\mathrm{slab}})}{n_{\mathrm{Ni}}} \tag{4.2}$$

4.3 Ni Clusters in Gas Phase

Ni clusters in the gas phase have been investigated with a size of 2, 3, 4, 5, 9 and 10 Ni atoms (Figure 4.1). At a size of five and nine Ni atoms, both a flat and a three-dimensional (3D) initial configuration of the cluster have been considered. Nevertheless, energy optimization of both initial configurations of Ni clusters with nine atoms resulted in a 3D structure. Results are thus presented only for the most stable structure with nine atoms. All simulated configurations have been assumed to exist in a singlet state.

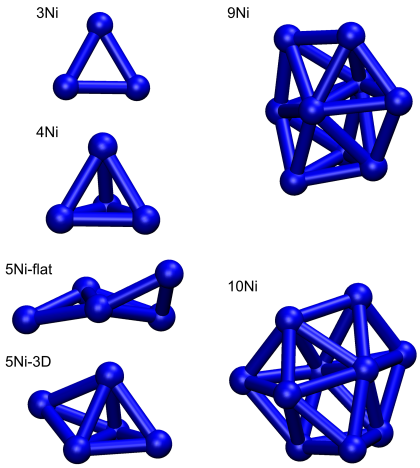

Figure 4.1: Stable configurations of Ni clusters in gas phase with a particle size of 3, 4, 5, 9 and 10 atoms. Formation energy and geometrical properties are reported in Table 4.1.

The formation energy E_{F} has been calculated referring to the energy of a single Ni atom (gas phase) in the triplet state. The absolut value of E_{F} increases with increasing number of Ni atoms in the cluster (Table 4.1, Figure 4.2) and converges towards a value of ca. -3 eV. This behavior is consistent with what has been shown previously using molecular orbital theory [131] and DFT [132]. The three-dimensional configuration of a cluster with five Ni atoms is found to be favored over the flat configuration by an energy of 0.08 eV. The same has been observed previously by Lu et al. [132]. However, there, the energy difference between the two configurations was significantly higher ($\Delta E_{\mathrm{F}} = 0.54$ eV) [132].

Table 4.1: Formation energy E_{F}, average Ni-Ni bond length $d_{\mathrm{Ni-Ni}}$ and radius of gyration r_{G} of Ni clusters with varying number of atoms.

configuration	E_{F} [eV]	$d_{\mathrm{Ni-Ni}}$ [Å]	r_{G} [Å]
2Ni	-1.27	2.11	1.05
3Ni	-1.76	2.22	1.28
4Ni	-2.09	2.31	1.41
5Ni-flat	-2.26	2.29	1.83
5Ni-3D	-2.34	2.34	1.59
9Ni	-2.88	2.39	2.08
10Ni	-2.95	2.38	2.15

A similar trend is observed for the average bond length of Ni atoms. The Ni-Ni bondlength ($d_{\mathrm{Ni-Ni}}$) increases from 2.11 Å for the Ni-dimer to 2.39 Å in a cluster with nine Ni atoms (Table 4.1, Figure 4.2). This is again in excellent agreement with previous calculations [131, 132]. In the flat cluster with five Ni atoms, $d_{\mathrm{Ni-Ni}}$ is found to be smaller (2.29 Å) compared to its 3D isomer (2.34 Å).

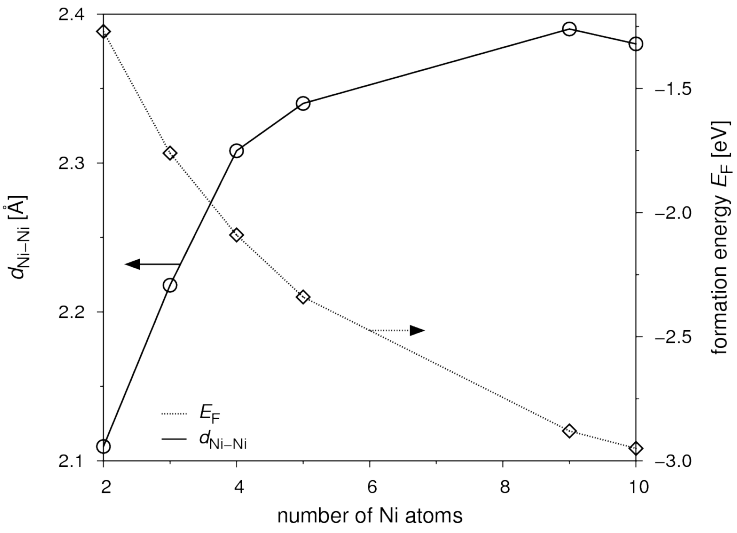

Figure 4.2: Average Ni-Ni bond length $d_{\mathrm{Ni-Ni}}$ and formation energy E_{F} of Ni clusters as a function of the cluster size (number of Ni atoms).

4.4 Adsorption of Atomic Ni on CeO_2(111)

Stability Adsorption of a single Ni atom on CeO_2 has been simulated on three different high-symmetrical surface sites: (i) on-top of a surface O atom (*top*), (ii) on a hollow site (*hol*) and (iii) on a bridge site (*bri*). The resulting optimized configurations are shown in Figure 4.3. Ni is found to be most stable on a *bri* site (Figure 4.3 c) with a binding energy of -2.37 eV (Table 4.2). On a *hol* site, it is slightly less stable with E_B=-2.18 eV. The least stable adsorption site is on-top of a surface oxygen atom (*top*) resulting in a binding energy of -1.87 eV. No stable configuration is found for Ni adsorbed on-top of Ce.

Contradictory results have been reported in previous computational studies for atomic adsorption of Ni on CeO_2(111). Using standard DFT calculations with the exchange correlation functional proposed by Perdew and Wang [127], Chafi et al. found Ni to be most stable on a *top* site with a binding energy of -2.64 eV [128]. Adsorption on *hol* was less stable with a binding energy of -2.42 eV (Table 4.2). This is in contrast to the results of Lu et al. [129] where Ni was least stable on a *top* site in agreement with our calculations. However, Lu et al. [132] found Ni to be most stable on a *hol* site whereas we observed *bri* to be the favored adsorption site. A possible explanation for this discrepancy is that the various positions of Ce^{3+} atoms, formed upon Ni adsorption, have not been considered explicitly in our calculations. The location of Ce^{3+} has been shown to vary the stability of adsorbed Ni by up to 0.5 eV [130].

Table 4.2: Binding energy E_B in eV of one Ni atom adsorbed on CeO_2(111) on top of a surface O atom (*top*), on a hollow site (*hol*), on a O bridge site (*bri*) and on top of a Ce atom (top_{Ce}).

reference	*top*	*hol*	*bri*	top_{Ce}
this work	-1.87	-2.18	**-2.37**	not stable
Chafi et al. [128]	**-2.46**	-2.43	–	-1.92
Lu et al. [129]	-0.35	**-1.51**	-1.18	–
Carrasco et al. [130]	–	**-3.68**	–	–

Geometry In the least stable configuration on a *top* site, the Ni atom binds to a surface O atom (O_{surf}) with a Ni-O bond length of 1.73 Å (Table 4.3). This is slightly smaller than what has been reported in previous computational studies (1.76 Å [129]) and 1.77 Å [128]). The adsorption of Ni on *top* causes only marginal reconstruction of the CeO_2 surface. The active O_{surf} moves away from the surface by 0.04 Å compared to its position on the clean CeO_2(111) surface. At the same

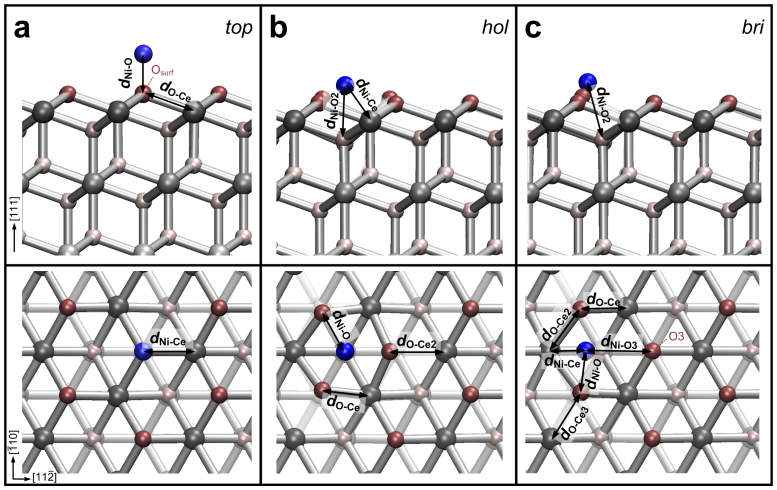

Figure 4.3: Stable configurations of one Ni atom adsorbed on a (a) *top*, (b) *hol* and (c) *bri* site. Ni is found to be most stable on *bri* with a binding energy of -2.37 eV.

time, this leads to an elongation of the O_{surf}-Ce bondlength from 2.34 Å (clean CeO_2) to 2.41 Å.

In the three-fold coordinated configuration of Ni on a *hol* site, the Ni-O bond length is significantly larger (2.06 Å) and identical to previous calculations (2.06 Å [129]). Adsorption of Ni causes a contraction of the surface O atoms bound to the adsorbate resulting in a significant elongation of the O-Ce bond length to the next nearest Ce atom (d_{O-Ce2}, Figure 4.3) to 2.66 Å. This is in reasonable agreement with what has been observed previously (2.72 Å [129]). Furthermore, the adsorption of Ni leads to a shift of the neighboring surface O atoms away from the surface by 0.20 Å compared to their position on the clean CeO_2(111) surface.

The Ni atom on a *bri* site is two-fold coordinated to the O atoms of the CeO_2 slab. Accordingly, the Ni-O bond length (d_{Ni-O}) is with 1.96 Å in between the one of one- (*top*, 1.73 Å) and three- (*hol*, 2.06 Å) fold coordinated Ni. In contrast to the one-fold coordination, here, d_{Ni-O} is slightly overestimated compared to previous results (1.89 Å [129]). The distance to the next nearest O atom (O3, Figure 4.3) is found to be 3.07 Å certifying the absence of a bond between Ni and O3. Adsorption on *bri* causes a shift of the interacting surface O atoms outward of the surface by 0.29 Å similar to what is observed on *hol* (0.20 Å). Additional specifications of the geometry are listed in Table 4.3.

Electronic Structure Analysis of the projected density of states (PDOS) for all three stable configurations (Figure 4.4) revealed the evolution of occupied d-

Table 4.3: Geometrical properties in Å of one Ni atom adsorbed on CeO_2(111) on top of a surface O atom (*top*), on a hollow (*hol*) and on a O bridge site (*bri*). A graphical description of the distances is shown in Figure 4.3.

site	d_{Ni-O}	d_{Ni-O2}	d_{Ni-O3}	d_{Ni-Ce}	d_{O-Ce}	d_{O-Ce2}	d_{O-Ce3}	reference
top	1.73	–	–	3.41	2.41	–	–	this work
	1.76	–	–	–	–	–	–	[129]
	1.77	–	–	3.48	–	–	–	[128]
hol	2.06	2.56	–	2.73	2.32	2.66	–	this work
	2.06	–	–	–	–	2.72	–	[129]
bri	1.96	2.71	3.07	2.40	2.28	2.56	2.63	this work
	1.89	–	–	–	–	–	–	[129]

type orbitals of Ni above the valence band of CeO_2 when Ni atoms are adsorbed on the surface. The position of these states is similar on a *top* and *hol* site located at 1.77 eV (Figure 4.4 a) and 1.76 eV (Figure 4.4 b), respectively, above the valence band of CeO_2. When Ni is adsorbed on a *bri* site, these states are found at remarkably lower energy (1.20 eV above the CeO_2 valence band, Figure 4.4 b). This indicates a stabilization of Ni on *bri* compared to the other two adsorption sites and is in agreement with its lower binding energy. A detailed analysis of the PDOS (Figure 4.4 d) shows degenerated states in the highly symmetric *hol* configuration. A shift of the Ni atom to a *bri* site breaks the symmetry and leads to a splitting of the degenerated states and a shift of the latter two lower energies explaining the stabilization of Ni on *bri*.

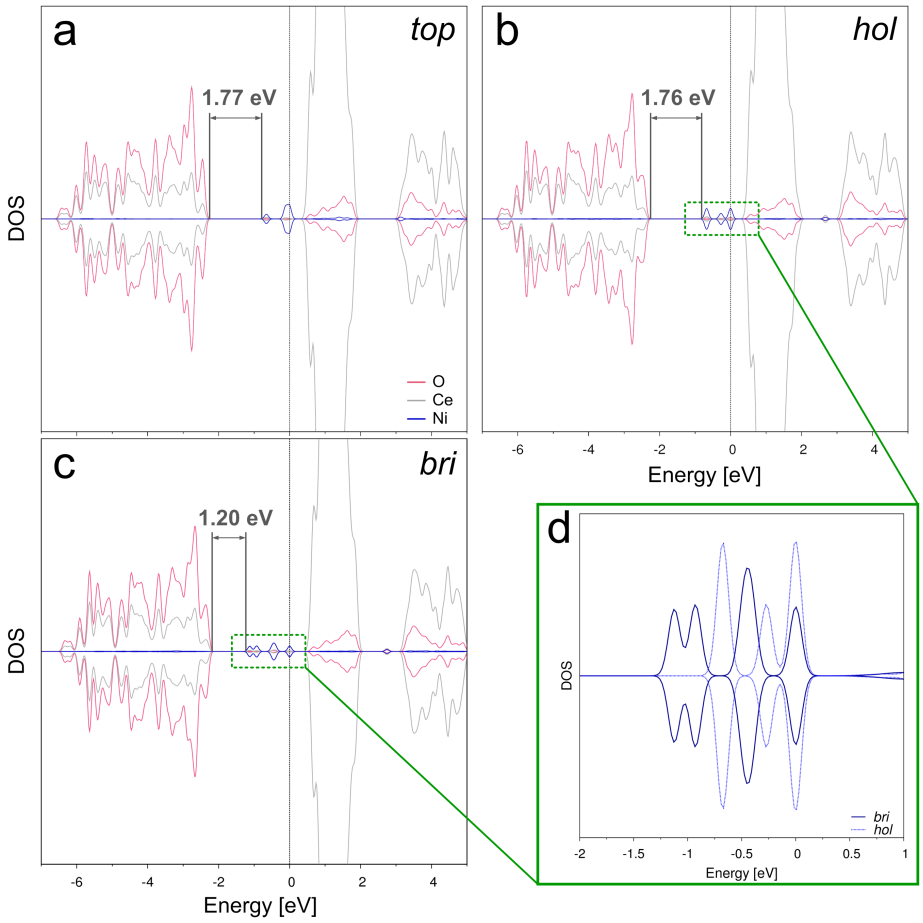

Figure 4.4: PDOS of Ni adsorbed on a (a) *top*, (b) *hol* and (c) *bri* site. The inlet (d) shows a magnification of the occupied d-type orbitals of Ni on *hol* and *bri* demonstrating a shift of these orbitals to lower energies when Ni is adsorbed on a *bri* site.

4.5 Adsorption of Multiatomic Ni Clusters on CeO_2(111)

Stability The binding energy E_B of Ni clusters on CeO_2 has been calculated referring to the gas phase energy of a single Ni atom (triplet). The effect of the number of Ni atoms on the stability of the clusters adsorbed on CeO_2 is similar to what has been observed in the gas phase: the absolute value of the binding energy increases with the number of Ni atoms (Figure 4.6). Various configurations have been investigated at each cluster size (number of Ni atoms) demonstrating three-dimensional (3D) configurations to be favored over flat ones. Selected configurations of stable structures are shown in Figure 4.5. The binding energy of the most stable configuration converges to a value of ca. -3.7 eV.

Table 4.4: Binding energy E_B, average Ni-Ni bond length d_{Ni-Ni} and radius of gyration r_G of Ni clusters with different numbers of Ni atoms adsorbed on CeO_2.

configuration	E_B [eV]	d_{Ni-Ni} [Å]	r_G [Å]
3Ni	-3.15	2.29	1.32
5Ni-flat	-3.28	2.42	2.02
5Ni-3D	-3.40	2.35	1.70
9Ni-flat	-3.31	2.44	2.83
9Ni-3D	-3.55	2.42	2.25
10Ni	-3.60	2.44	2.26
13Ni	-3.64	2.39	2.68

It has to be noted that the simulated configurations have been assumed to exist in a singlet state. Changes in the spin configuration can possibly have a considerable effect on the stability of the systems as it has been shown for the adsorption of single Ni atoms on CeO_2(111) [130]. An explicit elaboration of all possible spin states, however, is complex and not feasible within this study. Nevertheless, the here presented results are expected to give an accurate qualitative trend for the stability of Ni clusters adsorbed on CeO_2(111).

Geometry The morphology of Ni clusters can be described by the radius of gyration r_G. It has been calculated according to eq. (4.3), where r_i is the position of atom i, r_{CM} is the center of mass of the Ni cluster and n_{Ni} is the number of Ni atoms.

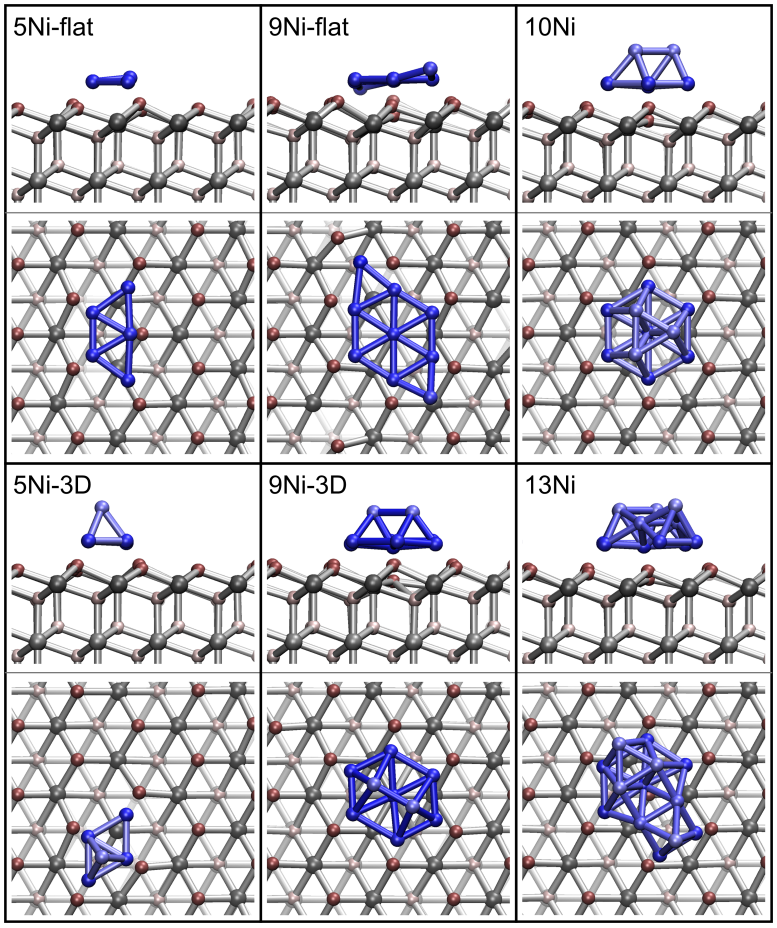

Figure 4.5: Selected stable configurations of Ni clusters adsorbed on CeO_2(111). Corresponding binding energy and structural properties of the shown configurations are reported in Table 4.4.

$$r_{\mathrm{G}}^2 = \frac{\sum_i^{n_{\mathrm{Ni}}} \left(\vec{r}_i - \vec{r}_{CM}\right)^2}{n_{\mathrm{Ni}}} \tag{4.3}$$

A smaller radius of gyration indicates a more compact structure of the cluster. This is verified comparing the radius of gyration for flat and 3D structures: r_{G} of flat structures is always greater than the one of 3D structures (Table 4.4, Figure 4.7). The stabilization of the 3D structure over the flat one is additionally reflected in the smaller average Ni-Ni bond length ($d_{\mathrm{Ni-Ni}}$). This is especially pronounced at a cluster size of five Ni atoms, where $d_{\mathrm{Ni-Ni}}$ in the 3D structure is by 0.07 Å smaller than in the flat structure.

The interaction of Ni atoms with the CeO_2 surface leads to a small opening

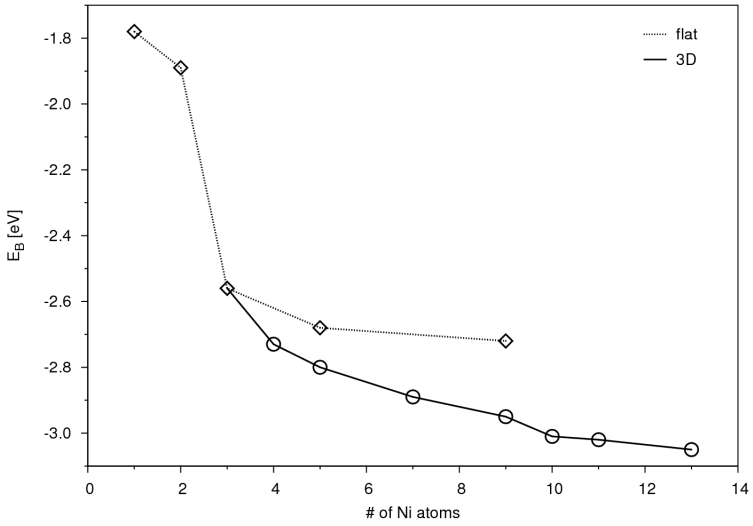

Figure 4.6: Binding energy E_B of Ni clusters adsorbed on CeO_2(111) in a flat (dashed line) and three-dimensional (3D, solid line) configuration. 3D structures are favored over flat ones at all calculated cluster sizes.

of the cluster structure, displayed by a larger r_G and longer d_{Ni-Ni} compared to Ni clusters in the gas phase (Table 4.1). This suggests that the accessibility of Ni clusters supported on CeO_2 is enhanced compared to gas phase clusters and can possibly lead to facilitated reaction mechanisms of adsorbing molecules such as CO_2.

The radius of gyration r_G naturally increases with the number of particles. In order to compare the radius of gyration of clusters formed from different numbers of Ni atoms, r_G has thus been normalized to the number of Ni atoms ($\frac{r_G}{n_{Ni}}$). The evolution of the normalized radius of gyration with increasing number of atoms of the cluster is represented in Figure 4.7. The normalized r_G decreases monotonously with the number of Ni atoms (Figure 4.7) for 3D structures indicating the formation of compact Ni clusters and it converges towards a value of 0.2 Å for clusters with more than eleven atoms.

The quantitative description of the stability of CeO_2-supported Ni clusters depending on their morphology is an interesting task since it can give an estimation of the spontaneous formation of Ni clusters on CeO_2(111) when produced experimentally. Here, we have analyzed the evolution of the binding energy of Ni clusters as a function of their normalized radius of gyration (Figure 4.8) for all investigated configurations. The binding energy shows a linear trend with the radius of gyration. Linear regression estimates a binding energy of -3.96 eV at a the hypothetical limit of r_G=0 Å. This is reasonably close to the binding energy

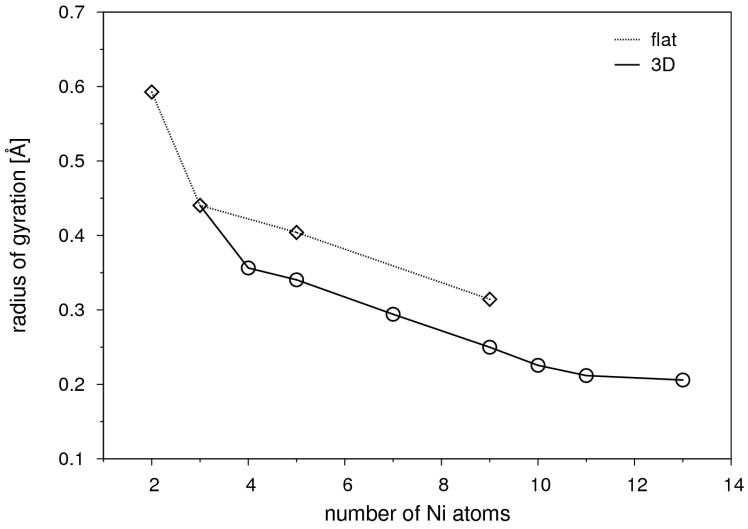

Figure 4.7: Evolution of the radius of gyration r_G of Ni clusters adsorbed on CeO_2(111) with the number of atoms in the cluster. r_G has been normalized to the number of Ni atoms ($\frac{r_G}{n_{Ni}}$).

calculated here of Ni clusters with ten to 13 atoms ($|E_B|$ =3.60-3.64 eV) proposing that the stability of the clusters will enhance only marginally with further addition of Ni atoms.

Moreover, with this approximation, the maximum r_G can be estimated where Ni adsorption becomes thermodynamically unfavorable (E_B>0 eV). With the linear behavior found here, the maximum value of the normalized radius of gyration is calculated to be 1.87 Å. This is consistent with simulations we have performed for Ni layers extended on CeO_2. These configurations are not stable, instead, depending on the Ni coverage, the adsorbed atoms are forming either clusters or structurally rearrange to multilayers.

Electronic Structure As discussed before, adsorption of single Ni atoms leads to the formation of occupied d-type Ni orbitals in the band gap of the CeO_2 semiconductor (section 4.4). This effect becomes more pronounced upon adsorption of multiatomic Ni clusters. Figure 4.9 shows the evolution of such states with the number of Ni atoms in the cluster. With increasing number of Ni atoms, more and more d-type orbitals are occupied and the distinguishable peaks reform into a band between the valence band of CeO_2 and the unoccupied Ce-4f states. This behavior leads to a decrease of the band gap and suggests a metallic character of the surface at a certain number of Ni atoms. In fact, at a cluster size of 13 Ni the band gap vanishes completely.

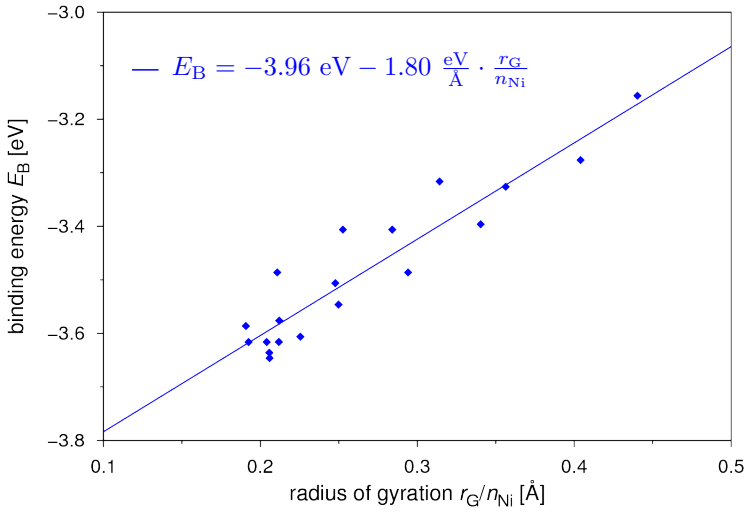

Figure 4.8: Binding energy E_B of Ni clusters adsorbed on CeO_2(111) as a function of the gyration radius normalized to the number of Ni atoms ($\frac{r_G}{n_{Ni}}$).

A similar electronic structure is observed in both a flat and a three-dimensional configuration of the cluster. The PDOS of Ni clusters with nine atoms of the two configurations is depicted in Figure 4.10. In the case of the 3D cluster, the occupation of α and β spin is more symmetric.

Figure 4.11 shows the spin density of a Ni cluster with ten atoms adsorbed on the CeO_2 surface. Green and yellow lobes indicate α and β spin density, respectively. It is remarkable that the same spin states accumulate on neighboring Ni atoms leading to a spatial separation of the spin density to opposite sites of the cluster. The system calculated here has been constrained to exist in a singlet state implying that a multiplicity higher than 1 is not allowed. However, the accumulation of the spin density suggests that a ferromagnetic state with higher multiplicity is favorable. This is in agreement with previous calculations of Ni clusters in the gas phase demonstrating a stabilization of the cluster at a multiplicity >1 [133–135]. The geometric configuration of such Ni clusters, however, has been shown to be hardly affected by the spin ordering [135].

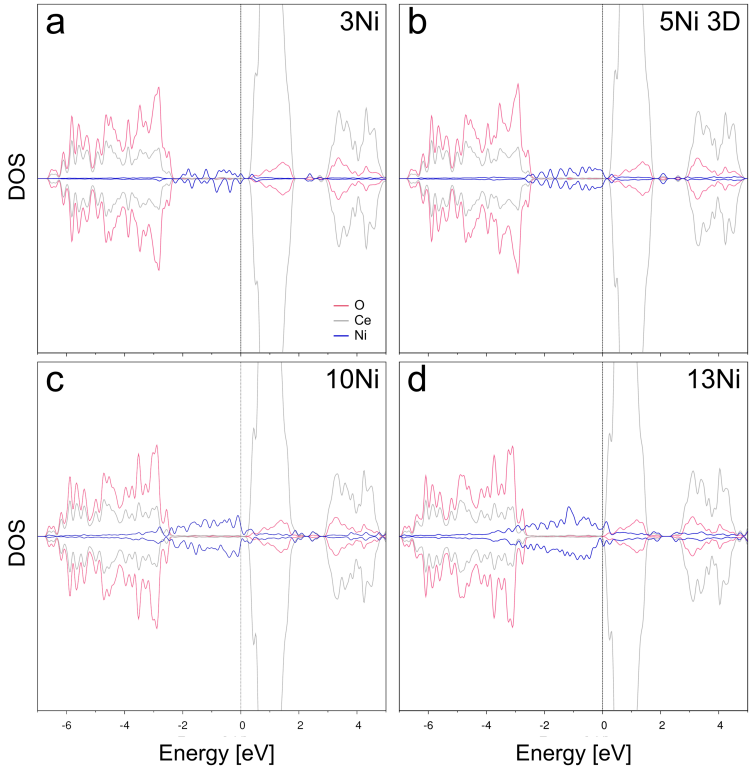

Figure 4.9: PDOS of Ni clusters with (a) 3, (b) 5, (c) 10 and (d) 13 atoms adsorbed on CeO_2(111).

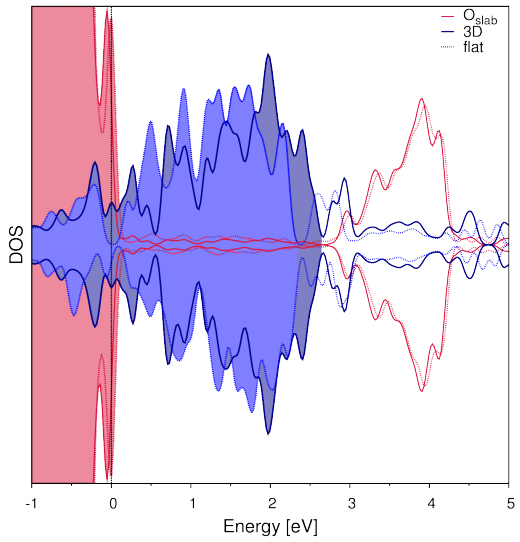

Figure 4.10: PDOS of Ni clusters with nine atoms in a flat (dotted line) and in a three-dimensional (solid line) configuration. For better comparison, the upper edge of the valence band of CeO_2 has been set to 0 eV. Filled curves indicate occupied orbitals.

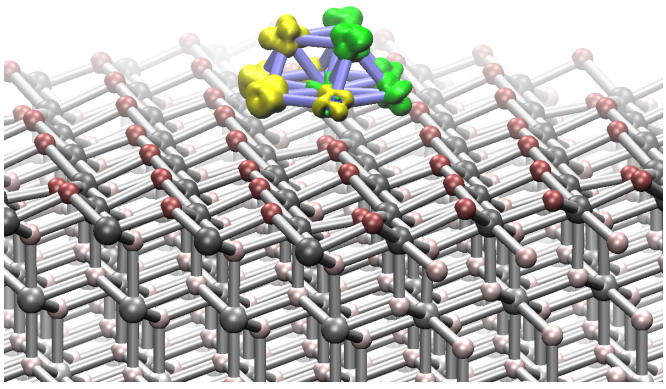

Figure 4.11: Spin density of Ni cluster containing ten atoms adsorbed on CeO_2(111).

4.6 Conclusions

Structural and electronic properties of small Ni clusters in the gas phase have been investigated with DFT calculations for cluster sizes up to ten atoms. Ni clusters have been shown to stabilize with increasing amount of atoms in agreement with previous studies [131, 132]. For a cluster size of five atoms, two different configurations have been calculated demonstrating a higher stability of a three dimensional structure than a flat one. The average Ni-Ni bond length has been shown to increase with the number of atoms in the cluster converging to a value of 2.38 Å at a cluster size of nine atoms confirming previously calculated results [131, 132].

Three stable configurations of single Ni atoms adsorbed on CeO_2(111) have been investigated: on (i) a *top*, (ii) a *hol* and a (iii) *bri* site. *bri* has been identified to be the favored adsorption site. The least stable configuration has been found on a *top* site. Minor differences in the stability of the calculated configurations exist between our results and results of previous computational studies. This can possibly result from the fact that, here, only a singlet state of the system has been calculated and no specific distribution of excess electrons, i. e. the position of Ce^{3+} atoms, has been considered. However, structural properties have been found to be in very good agreement with previous results regardless of the electronic configuration. The Ni-O bond length increases with increasing coordination of Ni ($d_{\mathrm{Ni-Ni}}\,(top) < d_{\mathrm{Ni-Ni}}\,(bri) < d_{\mathrm{Ni-Ni}}\,(hol)$). At the same time, a contraction of neighboring surface O atoms has been observed leading to an elongation of the O-Ce bond length of nearby slab atoms.

The behavior of the stability of Ni clusters adsorbed on CeO_2(111) is comparable to the progression of the stability of Ni clusters in gas phase. The absolute value of the binding energy increases with the number of atoms converging to ca. -3.7 eV at a cluster size of ten atoms. Stability of three-dimensional (3D) and flat configurations has been compared showing 3D structures to be thermodynamically favorable. The average Ni-Ni bond length ($d_{\mathrm{Ni-Ni}}$) and the gyration radius (r_{G}) increase with the number of Ni atoms analogous to the behavior in the gas phase. However, both $d_{\mathrm{Ni-Ni}}$ and r_{G} are slightly larger when Ni clusters are adsorbed on CeO_2 indicating an opening of the structure. This suggests that the accessibility of CeO_2-supported Ni clusters is improved leading to enhanced catalytic properties compared to pure Ni particles.

Analysis of the density of states has identified the occupation of d-type Ni orbitals in between the band gap of CeO_2 when Ni is adsorbed on its surface. These orbitals show distinguishable peaks between 1.2 and 1.8 eV above the CeO_2 valence band in the case of single atom adsorption. With increasing cluster size, these peaks evolve into a band of occupied states filling completely the band gap of the CeO_2 surface. At a cluster size of 13 atoms, the band gap vanishes

completely.

For a Ni cluster of ten atoms, the spin density has been investigated showing a separation of α and β spin density to opposite sites of the cluster. The spatial accumulation of spin density points to a ferromagnetic ground state of the cluster. However, within this study, only singlet states have been investigated. Thus, it has not been possible to verify the stability of high-spin states of Ni clusters. A detailed analysis of high-spin states of Ni clusters adsorbed on CeO_2 could provide a deeper understanding of the influence of the CeO_2 support on the electronic configuration of the adsorbed Ni clusters.

5

CO_2 Adsorption on CeO_2

5.1 Introduction

The rare earth metal oxide ceria (CeO_2) has been shown to be an excellent catalyst for CO oxidation and NO_x reduction reactions [75, 89, 136] but also for hydrogenation of CO_2 [137, 138] owing to its unique potential to store and release oxygen depending on the process conditions.

Hydrocarbon production from CO_2 is in particular interesting since it provides high energy density fuel from CO_2 which is omnipresent in our environment. The dominating mechanism for this process is the Sabatier reaction (eq. (5.1)). The reaction itself is exothermic (-252 $\frac{\text{kJ}}{\text{mol}}$ [112]). However, remarkable activation barriers are present due to the high thermodynamic stability of CO_2 [139].

$$CO_2 + 4H_2 \longrightarrow CH_4 + 2H_2O \quad (-252\frac{\text{kJ}}{\text{mol}}) \tag{5.1}$$

The activation barriers can be decreased if the linear CO_2 molecule transforms into a bent, anionic configuration prior to the hydrogenation reaction. The bent CO_2^- is ca. 0.5 eV [139] less stable than the linear molecule facilitating subsequent reactions such as CO_2 dissociation or hydrogenation.

Numerous studies have been conducted on the adsorption and activation of CO_2 on metal surfaces such as Cu [140–143], Pt [144, 145], Pd [146, 147] and Fe [143, 148, 149] where the Fe(110) surface has been identified to be most suitable for CO_2 activation [150]. This has been attributed to a remarkable charge transfer (0.83 e^-) from the surface to the CO_2 molecule and to the elongation of one of the C-O bonds (to ca. 1.30 Å) including bending of the CO_2 molecule [150]. The most widely used metals for CO_2 methanation, however, are Ni and Rh [112]. Using DFT calculations, it has been verified, that the reaction on Ni also involves the formation of the bent CO_2 intermediate [151].

DFT calculations of the adsorption mechanism on metal oxides have revealed that CO_2 adsorbs preferably in a linear configuration on most monoxides such as TiO, CrO, VO and MnO [152]. The same behavior has been observed on TiO_2 [153, 154] and $LaMnO_3$ [155]. In contrast, favorable bent geometries have been determined on CaO and FeO [152]. The different adsorption mechanisms can be attributed to the acidity of the metal oxide surface [156, 157]. In this scheme, the metal oxide surface is regarded as Lewis acid when the adsorbing molecule reacts with the surface on the metal cation and as Lewis base when it reacts on the O^{2-} site. Most metal oxide surfaces react as Lewis acids on which organic molecules are adsorbed without dissociation. Basic metal oxides, on the other hand, rather lead to dissociation of molecules and, in the case of CO_2, promote the formation of a bent CO_2^- species including a charge transfer from O^{2-} sites to the CO_2 species.

In experimental studies using IR and XPS the presence of bent carbonate species on CeO_2 upon CO_2 adsorption has been observed [158] suggesting the CeO_2 surface to react as Lewis base in the CO_2 adsorption process. Theoretical evidence from DFT calculations on the adsorption processes on CeO_2, however, is rare. This is mainly due to the complex electronic structure of CeO_2 exhibiting highly localized 4f states about 3 eV above the valence band [84, 87]. Upon reduction of Ce^{4+} to Ce^{3+} these states become occupied [86, 104, 159] and an accurate description of the electronic structure with standard DFT becomes problematic [30]. Nevertheless, standard DFT calculations have shown to correctly describe the stoichiometric CeO_2 bulk and surface [30, 97, 98] as long as no reduction of Ce^{4+} to Ce^{3+} is involved.

In fact, comparing standard DFT with DFT+U calculations it has been shown that even CO adsorption on the (111) and (110) surface can be accurately treated with standard DFT [89]. Results using both the standard DFT and the DFT+U method were in reasonable agreement with experimental studies [160, 161]. While CO physisorbs on the (111) surface, a carbonate species with two adjacent surface O atoms is formed when adsorbed on the (110) surface [89]. Calculations based on the DFT+U method have been applied recently for the investigation of CO_2 adsorption on stoichiometric and reduced CeO_2(110) showing the formation of a bent CO_2 species on the reduced surface [162]. Only weak adsorption without geometric deformation has been observed on the stoichiometric surface [162].

In this chapter, CO_2 adsorption has been investigated on the CeO_2(111) surface using standard DFT calculations. Different adsorption mechanisms are examined for CO_2 molecules at coverages ranging from 1/9 to 1 monolayer (ML). The coverage effect on the most stable configurations is discussed in terms of stability, geometry and electronic structure. The results are compared to CO_2 adsorption on other metal and metal oxide surfaces in order to give an estimate of the degree of CO_2 activation. Selected adsorption modes are additionally simu-

lated using hybrid functional (PBE0 [44]) and DFT+U calculations and compared to the results of standard DFT verifying the qualitative accuracy of the latter.

5.2 Methods

The calculations of this chapter have been carried out with spin-restricted DFT calculations if not stated differently. The q12 pseudopotential (see chapter 3) has been used to describe the interactions of the frozen Ce core explicitly considering twelve valence electrons. The basis set for Ce has been optimized in the atomic ground state [61] and has the form of a double-ζ valence (DZV) basis set without polarization. In the valence shell of C and O atoms, four and six electrons, respectively, are calculated explicitly. A triple-ζ valence plus double polarization (TZV2P) basis set, optimized according to the Mol-Opt method [62] is adopted for C and O atoms. For auxiliary plane wave expansion of the charge density, the energy cutoff is set to 1000 Ry.

The GGA formalism has been shown to yield reasonably accurate results for the CeO_2 bulk [30] and its (111) surface [97, 98]. To confirm the suitability of the standard DFT method for the simulation of CO_2 adsorption on CeO_2(111), selected configurations are additionally calculated using the PBE0 [44] hybrid functional with 20% exact exchange and DFT+U calculations with the PBE functional and a U value of 5 eV. Some configurations are further optimized introducing a Grimme D2 potential [163] to account for van der Waals interactions between adsorbates and surface slab.

All calculations are performed with periodic boundary conditions. The size of the simulated supercell is a critical parameter in real space calculations. It directs the accuracy of the physical properties of the system and the computational time needed. The supercell size has been optimized to reach convergence of the bulk properties such as lattice parameter and total energy per CeO_2 unit. A supercell containing 81 atoms has been found to be sufficient for the evaluated bulk properties. In this supercell, the primitive unit cell of fluorite CeO_2 is repeated three times in all spatial directions. The optimized lattice parameter for this setup has been calculated to be 5.48 Å, which is in good agreement with previous calculations (5.47 Å) [30] and experiments (5.41 Å) [84–88] (Table 3.2). The (111) surface is realized by introducing a vacuum of 15 Å along the [111] direction to avoid interaction with the periodic images of the slab. It has been verified that the amount of vacuum used (15 Å) is also sufficient to eliminate effects on the binding energy that result from van der Waals interactions between the images of the slab.

Convergence of the surface energy within 0.02 J/m^2 with respect to the slab thickness is reached with six O-Ce-O trilayers. In a p(3x3) expansion of the

(111) surface unit cell, the surface energy is calculated to be 0.73 J/m^2, in excellent agreement with previous calculations using the DFT+U method (0.72 J/m^2 [96], Table 3.2). The band gap between the O 2p and Ce 4f states of the clean CeO_2(111) slab is calculated to be 1.99 eV, which is again in good agreement with previous calculations using the PBE exchange correlation functional (2 eV) [30].

Depending on the CO_2 coverage, different surface dimensions are used: slabs with p(3x3), p(4x3), and p(4x4) expansions of the surface unit cell corresponding to a total of nine, twelve, and 16 active Ce sites, respectively. In all cases, the slab consists of six trilayers of which the top three are allowed to relax while the three bottom trilayers are fixed to simulate the bulk properties. Adsorption of CO_2 is simulated on one exposed surface. The CO_2 binding energy (E_B) is calculated according to eq. (5.2), where E_{slab} and $E_{CO_2,g}$ denote the total energy of the clean CeO_2 slab and the CO_2 molecule in gas phase, respectively. $E_{slab+nCO_2}$ is the energy of the surface slab plus n adsorbates. Equation (5.2) implies that negative values of E_B refer to an exothermic adsorption.

$$E_B = \frac{E_{slab+nCO_2} - (E_{slab} + nE_{CO_2,g})}{n} \tag{5.2}$$

The energy of an isolated CO_2 molecule ($E_{CO_2,g}$) has been calculated in a periodically repeated cell of 15x15x15 Å.

Optimization of the geometry of the CO_2 molecule in gas phase resulted in an O-C-O angle (α_{OCO}) of 180° and a C-O bond length (d_{CO}) of 1.17 Å, in good agreement with experiments (1.16 Å [164], Table 5.1). Geometrical properties of adsorbed CO_2 are characterized by α_{OCO}, the CO bond length (d_{CO} or d_{C-O1} and d_{C-O2}), and the adsorption height which is indicated by the distance of C to the closest surface O atom (d_{C-O}) for carbonate species and by the height of C above the first layer of Ce surface atoms (Δz_{CO_2}) for linear species (Figure 5.1).

Mulliken population analysis [165] is used to determine the charge transfer between surface and adsorbate. Further analysis of the electronic structure is carried out by projection of the Kohn-Sham orbitals at single atoms (projected density of states, PDOS) and the summation of the projections at the relevant atoms when multiatomic groups are of interest such as the CO_2 molecule or selected slab atoms. In this respect, the PDOS denoted as total in Figures 5.4 and 5.14 corresponds to the summation of the projections at all atoms of the system. The DOS is shifted so that the upper edge of the valence band of the CeO_2(111) slab is positioned at 0 eV.

5.3 Adsorption Mechanisms of Isolated CO_2

Stability and Geometry The adsorption mechanism of isolated CO_2 has been simulated on a CeO_2(111) slab with a p(3x3) surface unit cell at a CO_2 coverage of 1/9 ML. At this coverage, it is expected that interactions between adsorbates are negligible and the adsorbed species can be assumed to be isolated. Optimization of the geometry has led to three stable configurations: (i) mono- (Figure 5.1 a,d) and (ii) bidentate (Figure 5.1 b,e) carbonate species in a bent conformation and (iii) linearly adsorbed CO_2 (Figure 5.1 c,f). Starting from a linear configuration located 1.7 Å above the surface, the CO_2 molecule spontaneously transforms into the bent monodentate configuration indicating that no activation energy is required for the formation of the bent CO_2 molecule. However, starting from a stable linear configuration 3.5 Å above the surface, an energy barrier of 0.2 eV is observed for the transition from the linear to the monodentate configuration. The energy barrier has been determined using nudged elastic band (NEB) calculations (Figure 5.2). In the transition state the O-C-O angle decreases to 152.1° and the C-O bond length elongates to 1.20 Å.

Among the calculated configurations, the monodentate species is most stable with a binding energy of -0.31 eV, followed by the bidentate one with E_B=-0.12 eV. Both mono- and bidentate configurations have been optimized additionally with PBE0 resulting in a binding energy of -0.68 eV and -0.42 eV, respectively (Table 5.1, Figure 5.3). The lower values of the binding energy indicate stronger binding compared to standard DFT calculations. Using the DFT+U approach, binding energies have been determined to be -0.28 and -0.04 eV for the mono- and bidentate species, respectively, and thus reasonably close to the PBE results (Table 5.1, Figure 5.3). Results of the three methods are in qualitative agreement with the monodentate species being more stable than the bidentate one and it can be concluded that the results obtained with standard DFT calculations are qualitatively correct. Moreover, no reduced cerium ions are involved in the CO_2 adsorption on stoichiometric CeO_2(111) thus no Ce^{3+} atoms are present, additionally justifying the use of standard DFT calculations.

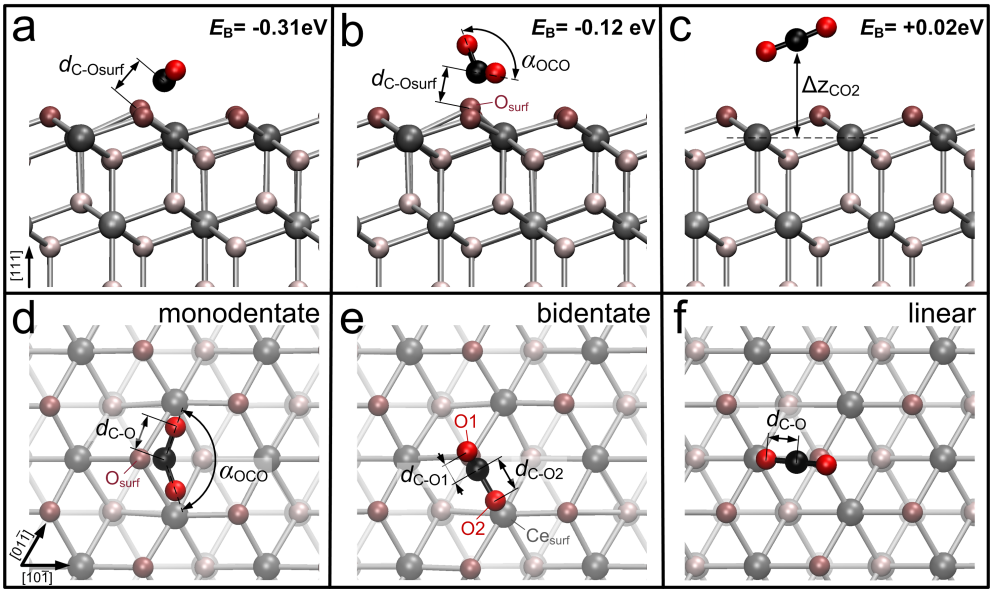

Figure 5.1: (a,b,c) Cross-sectional and (d,e,f) top view of stable configurations of isolated CO_2 adsorbed on a CeO_2(111) surface. In the most stable configuration (a,d), CO_2 forms a monodentate carbonate with the surface O atom resulting in a binding energy of -0.31 eV.

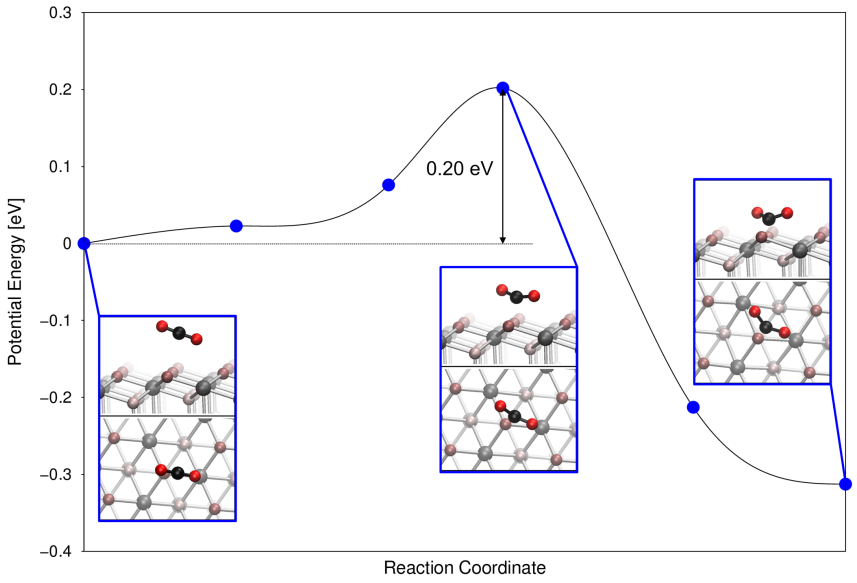

Figure 5.2: Potential energy surface for the transition of the linear CO_2 molecule at 3.5 Å above the surface to the monodentate configuration of CO_2 obtained from nudged elastic band calculations. For the adsorption of CO_2 in the bent monodentate configuration, an activation energy of 0.2 eV has been determined. In the transition state, the O-C-O angle decreases to 152.1° and the C-O bond length elongates to 1.20 Å.

Table 5.1: Average binding energy (E_B), geometric properties (explained in Figure 5.1), and total charge of CO_2 in the gas phase and adsorbed in different single-phase configurations on the $CeO_2(111)$ surface at 1/9, 1/2, and 2/3 ML coverage.

coverage	configuration	E_B [eV]	d_{C-O1} (d_{C-O2}) [Å]	$d_{C-O_{surf}}$ [Å]	Δz_{CO_2} [Å]	α_{OCO}[°]	charge
gasphase		-	1.17	-	-	180.0	0.00
1/9 ML	monodentate	-0.31	1.27	1.38	-	129.7	-0.46
	DFT+U	-0.28	1.27	1.38	-	129.5	-0.47
	PBE0 (20%)	-0.65	1.26	1.36	-	129.4	-0.54
	bidentate	-0.12	1.22 (1.30)	1.41	-	129.2	-0.40
	DFT+U	-0.04	1.22 (1.30)	1.43	-	130.3	-0.41
	PBE0 (20%)	-0.42	1.21 (1.29)	1.40	-	129.7	-0.48
	linear	0.02	1.17	-	3.52	177.6	0.03
1/2 ML	monodentate	-0.08	1.26	1.40	-	131.8	-0.34
	bidentate	0.19	1.21 (1.30)	1.44	-	131.0	-0.26
	linear	0.00	1.17	-	3.43	177.8	0.03
2/3 ML	monodentate	0.36	1.25	1.41	-	131.4	-0.27
	bidentate	0.43	1.20 (1.29)	1.46	-	131.6	-0.19
	linear	0.03	1.17	-	3.92	178.6	0.01

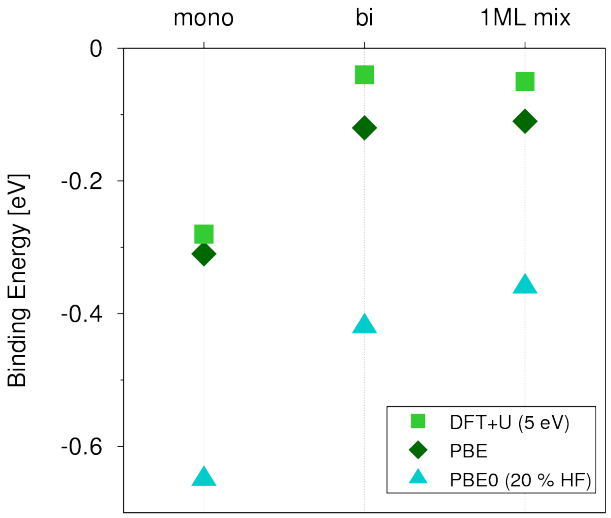

Figure 5.3: Binding energy of selected configurations (mono- and bidentate at 1/9 ML and mixed configuration of monodentate and linear species at 1 ML) of CO_2 adsorbed on CeO_2(111) calculated with DFT+U (U=5 eV), standard DFT using the PBE functional and PBE0. PBE0 calculations have been performed using 20% exact exchange. All methods show the same trends for the stability of different adsorption mechanisms.

Remarkable conformational changes are observed in the bent configurations compared to the linear CO_2 molecule in gas phase (Table 5.1). In the mono- and bidentate configuration, α_{OCO} decreases to 130° and 129° (Table 5.1), respectively. At the same time, both C-O bonds elongate to 1.27 Å in the monodentate configuration which is close to the literature value of a regular C=O bond of carbonyl (1.23-1.26 Å) [166]. Asymmetric bond elongation is observed in the bidentate configuration with 1.22 Å for d_{C-O1} and 1.30 Å for d_{C-O2} (see Figure 5.1 for definition of geometrical quantities). Both distances are in the range of a (partial) double C-O bond. Due to the longer d_{C-O2}, we suggest that, in this case, separation of one O atom is facilitated.

Previously, it has been shown that CO_2 is highly activated and adsorbs exothermically on Fe, whereas endothermic binding energies have been determined for various other metal surfaces such as Rh, Co and Pd [150]. The negative binding energies found here for mono- and bidentate configurations indicate exothermic adsorption of CO_2 also on CeO_2 and suggest similar bond strength as on Fe(110). Furthermore, the geometry of the monodentate configuration is similar to the most stable one found on a Ni(110) surface [167]. In contrast to metal surfaces, most metal oxides such as TiO_2 [168], TiO, ScO and MnO [152] favor

a linear CO_2 adsorption over the formation of bent mono- or bidentate species. Different behavior has only been shown on FeO where monodentate and on CaO where bidentate adsorption was favored [152]. It is thus suggested, that CeO_2 induces catalytic reaction mechanisms similar to the latter oxides.

The distance of C ($d_{C-O_{surf}}$) to the closest surface O atom (O_{surf}) in the monodentate configuration is found to be 1.38 Å indicating a partial double bond between the C atom and the surface O atom. For bidentate species, it is 1.41 Å, thereby somewhat larger and corresponding to a single C-O bond. This explains its weaker bond strength. Computational investigation of CO adsorption on CeO_2(110) [89] has revealed bond characteristics comparable to the one found here in the monodentate configuration. There, carbon monoxide has been shown to form a carbonate species with two surface O atoms, where the bond length between the C atom and the O atoms of the surface has been determined to be 1.35 Å [89]. Geometrical properties obtained with PBE0 and DFT+U are represented in Table 5.1. Using hybrid functional calculations the bond lengths tend to be smaller compared to PBE results. However, in general, only marginal deviations have been observed between the different methods.

Adsorption of linear CO_2 (Figure 5.1 c,f) is found to be endothermic with a binding energy of +0.02 eV. This result is obtained without consideration of dispersion interactions. Introducing a D2 Grimme-potential [163] to account for van der Waals interactions, the binding energy of the reoptimized linear configuration is found to be -0.07 eV indicating the adsorption of linear CO_2 to be exothermic. Hardly any changes in geometry compared to the gas phase CO_2 molecule have been observed for the linear configuration. In the simulation without D2, the O-C-O angle decreases slightly to 177.6° whereas d_{C-O} remains at 1.17 Å for both C-O bonds. The height of the molecule above the surface (Δz_{CO_2}, Figure 5.1 c) is 3.52 Å (Table 5.1). These results indicate weak interactions between the linear CO_2 molecule and the CeO_2(111) surface.

Electronic Structure A significant charge transfer from the CeO_2 surface to the CO_2 group is observed in both carbonate configurations resulting in a total charge of -0.46 and -0.40 for the mono- and bidentate species, respectively (Table 5.1). This is comparable to the charge transfer observed from Pd and Cu surfaces to CO_2 [150] and is an indication of the basic character of the CeO_2 surface [156]. On various other metal oxides such as TiO_2 [168], TiO, ScO and MnO [152] a different behavior has been observed. Linear adsorption has been found to be favored demonstrating an acidic character of these surfaces. Similar characteristics are observed here on CeO_2(111) when CO_2 adsorbs in a linear configuration where the CO_2 molecule has a minor positive charge (+0.03). In other words, depending on the adsorption mechanism, the CeO_2(111) surface can

act both as Lewis base or weak acid, however, its basic character is predominant.

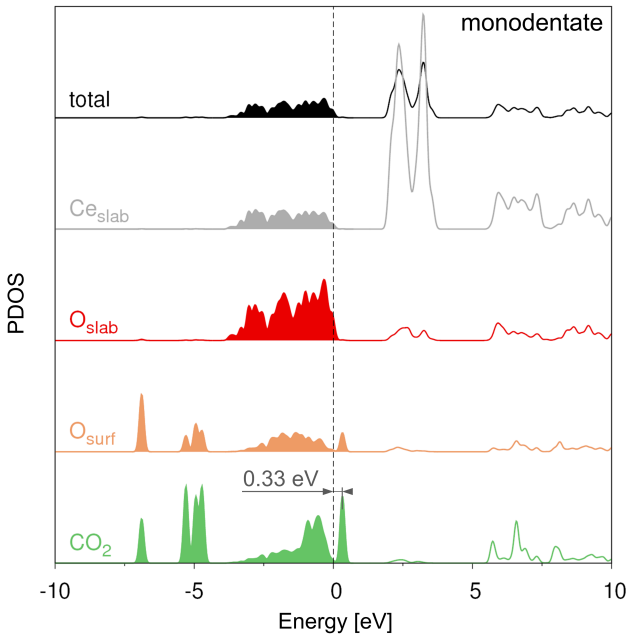

Figure 5.4: PDOS summed over all atoms (black) and on specific species (Ce_{slab}, O_{slab}, O_{surf} and CO_2) of isolated (1/9 ML) CO_2 adsorbed on CeO_2(111) in a monodentate configuration. Ce_{slab} and O_{slab} indicate the PDOS projected on the orbitals of Ce and O slab atoms, respectively. Filled curves indicate occupied orbitals. The reference 0 eV energy has been set to the edge of the valence band of the CeO_2(111) slab. Upon adsorption, the HOMO of the CO_2 molecule forming a carbonate species with the O_{surf} atom, has been found at 0.33 eV above the valence band of CeO_2(111).

Further analysis has been done on the DOS, shown in Figure 5.4 for monodentate adsorption. The adsorption leads to the evolution of one additional state at the top of the valence band attributed to hybridization of the p-type orbitals of the surface O atom with the orbitals of the CO_2 molecule (Figure 5.5). In the monodentate configuration, this state is located 0.33 eV above the valence band (Figure 5.4). The existence of this state is confirmed by PBE0 calculations where it is found 0.21 eV above the valence band (Figure 5.6).

Upon formation of a bidentate species, this state is found at higher energy (0.62 eV above the valence band), rationalizing the weaker bond of bidentate CO_2 on the CeO_2(111) surface. The evolution of additional CO_2 states above the CeO_2 valence band has been reported previously as well for the adsorption of CO

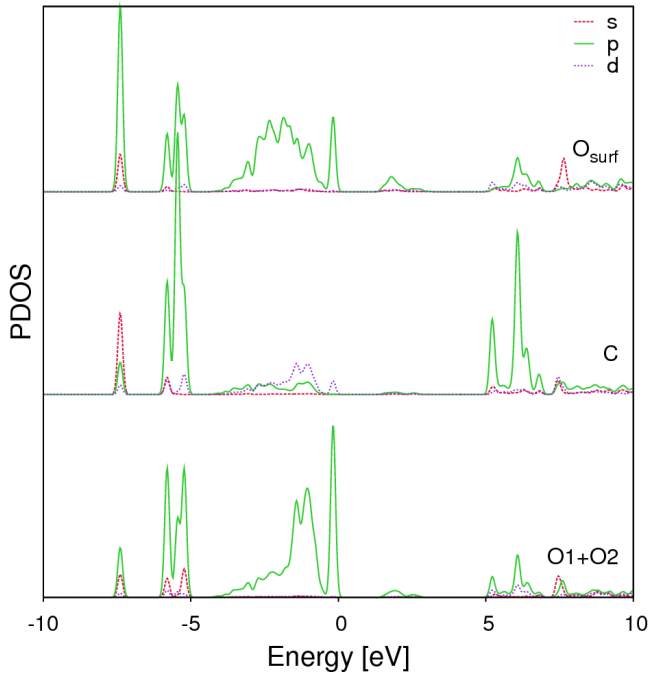

Figure 5.5: PDOS on s- (red lines), p- (green lines) and d-type (violet lines) orbitals of the O_{surf} atoms and the C and O (O1 and O2) atoms of the CO_2 molecule adsorbed on $CeO_2(111)$ in a monodentate configuration at 1/9 ML coverage. Binding of the CO_2 molecule at the valence band to the O_{surf} atom takes place through p-type orbitals of O_{surf} and hybridized orbitals of the C atom with d-character.

on $CeO_2(110)$ [89]. In the latter case, the additional states are formed 0.3 eV above the valence band. The acidic nature of the bent CO_2 molecule has been described previously [139] and its formation is promoted by the basic character of the CeO_2 surface.

Bending of the CO_2 molecule leads to a splitting of the unoccupied 2π orbital (LUMO) of the linear CO_2 molecule, holding $C_{2\infty}$ symmetry, into two orbitals, one of which is found at remarkably lower energy [139]. This favors the transfer of substrate electrons to the CO_2 molecule accompanied by the occupation of this orbital. The DOS of gas phase CO_2 and adsorbed species obtained from our calculations confirm this behavior (Figure 5.7): the LUMO splits into two distinguishable orbitals. The splitting results in a significant shift of one of the non-degenerate orbitals to lower energies (Figure 5.7 a, state 2). HOMO and LUMO of the bent gas phase CO_2 are shown in Figure 5.7 b (state 1 and 2). When CO_2 is adsorbed on $CeO_2(111)$ as either of the bent species, the shape of the HOMO (Figure 5.7 b, state 3) is similar to the one of the gas phase (Figure 5.7

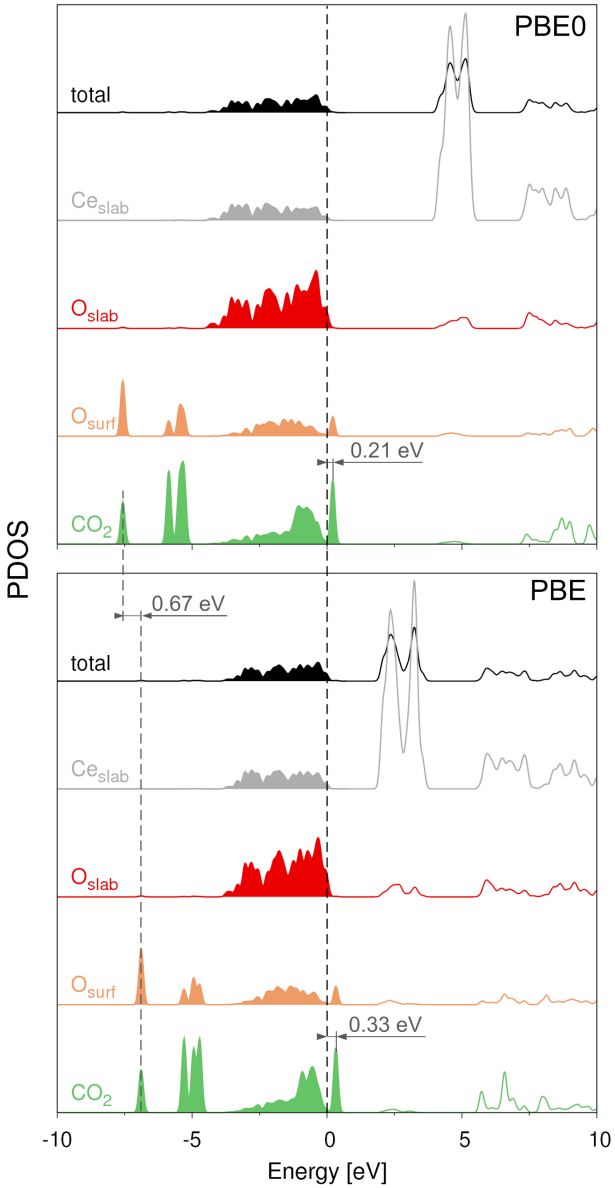

Figure 5.6: PDOS summed over all atoms (black) and on specific species (Ce_{slab}, O_{slab} and CO_2) of isolated (1/9 ML) CO_2 adsorbed on CeO_2(111) in a monodentate configuration calculated with PBE0 (top) and standard DFT (PBE, bottom). CO_2 orbitals ca. 6 eV below the valence band are found at lower energies (by 0.67 eV) for PBE0 than for PBE. Additional CO_2 states formed upon adsorption are found at 0.21 and 0.33 eV above the valence band of CeO_2 for PBE0 and PBE calculations, respectively.

b, state 1). However, several states of the valence band resemble the shape of the LUMO of CO_2 and can be attributed to hybridized carbonate states.

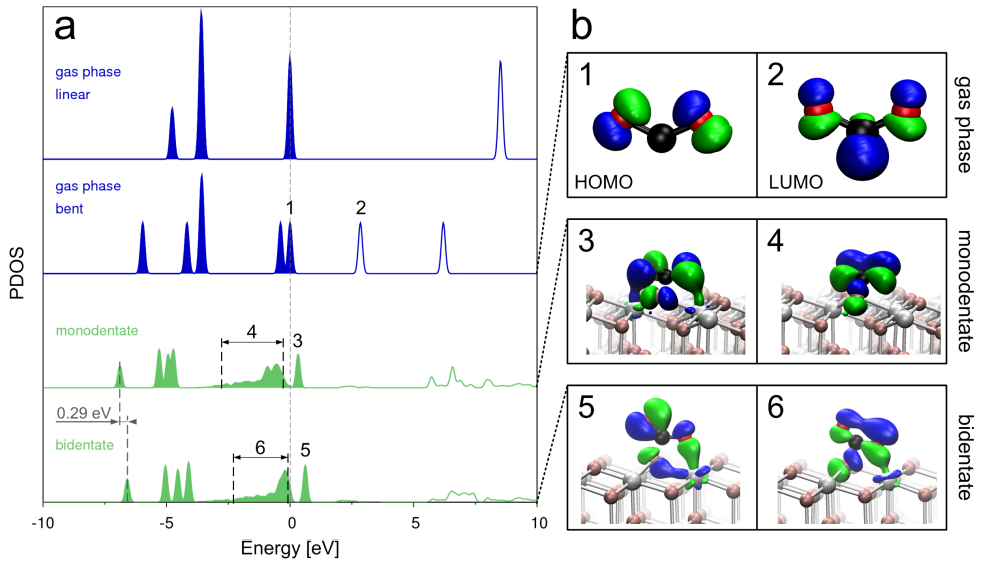

Figure 5.7: (a) PDOS of linear CO_2 in gas phase, bent CO_2 in gas phase and of CO_2 adsorbed on CeO_2(111) as mono- and bidentate species and (b) selected electronic states derived from the molecular orbitals of the CO_2 species. Upon adsorption, the LUMO (2) of gas phase CO_2 hybridizes and the binding orbital becomes occupied. Occupied molecular orbitals in both carbonate configurations resembling the LUMO of the gas phase CO_2 are found in the valence band between -2.5 and 0 eV (4,6).

The DOS of the monodentate configuration obtained with the PBE0 method is in general comparable to the one obtained with PBE (Figure 5.6). However, the binding orbital between C and O_{surf} found about 6 eV below the valence band are shifted by 0.67 eV to lower energies. Furthermore, the splitting between binding and anti-binding CO_2 orbitals is enlarged using the PBE0 method. This agrees with the binding energy for the monodentate configuration being lower (stronger binding) with PBE0 than with PBE. The PDOS of the adsorbed CO_2 species shows that the orbitals of the bidentate species are by 0.29 eV at higher energies compared to the monodentate species (Figure 5.7 a). This value is similar to the difference in binding energy of the two adsorption mechanisms (0.19 eV) verifying that these effects are related. The binding mechanism of the two configurations, however, is identical. It has been proposed previously that charge transfer to the bent CO_2 molecule and thus formation of an anionic species leads to the occupation of the hybridized LUMO [139]. The resulting orbitals have bonding

character between C and O_{surf} and anti-bonding character between C and the O atoms of the molecule. The anti-bonding character leads to the elongation of the intramolecular C-O bonds which has been found for both mono- and bidentate species and is responsible for the activation of the CO_2 molecule [150].

Bond formation between O_{surf} and C is additionally confirmed by the charge density difference shown in Figure 5.8. Yellow lobes represent excess of electrons which are mainly found between O_{surf} and C and suggest the occupation of the LUMO of the bent gas phase CO_2 (Figure 5.7 b, state 2). This is further supported by the electron excess around the O atoms of the CO_2 molecule, which resembles the shape of the gas phase LUMO. On Ni(110), being one of the best metal-based catalysts for CO_2 methanation, similar bond characteristics between CO_2 and the surface have been reported based on charge density differences [151]. This demonstrates comparable chemical interaction of Ni and CeO_2 with CO_2 and it is thus proposed that mechanisms and properties of reactions involving CO_2 are similar on these surfaces. The charge density difference of the bidentate species observed between O_{surf} and C (Figure 5.8 b) is comparable to the one of the monodentate species (Figure 5.8 a). Additionally, the electron excess around the O2 atom is shifted towards the interacting surface Ce atom (Ce_{surf}) indicating polarization of O2 and Ce_{surf} orbitals. However, no chemical bond between O2 and Ce_{surf} is evident from the charge density difference. In contrast to the bent CO_2 species, the PDOS of the linearly adsorbed CO_2 is identical to the one of the free molecule lacking any indication of hybridization with the surface orbitals. Thus it can be concluded that the linearly adsorbed molecule does not form chemical bonds and does not cause any perturbation to the surface.

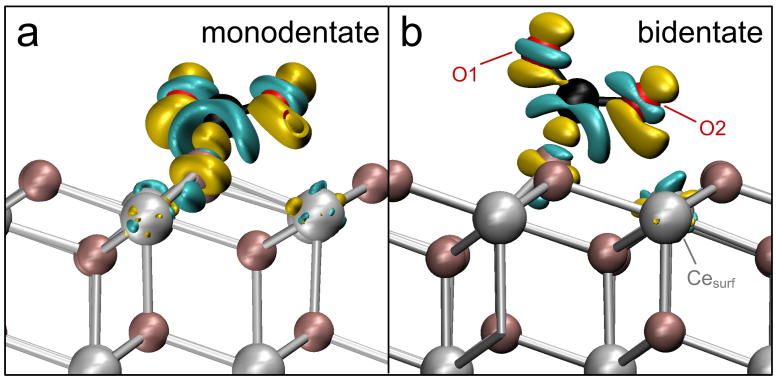

Figure 5.8: Isosurface of the charge density difference at 0.067 e/Å^3 for (a) monodentate and (b) bidentate CO_2 species. Yellow lobes indicate electron excess and cyan lobes indicate loss of electron density. The excess of electrons between O_{surf} and C demonstrates the filling of the LUMO (see Figure 5.7) of gas phase CO_2 and the binding character of the orbitals between the two atoms.

5.4 Coverage Effect on Single-Phase Adsorption Mechanisms

Stability and Geometry In addition to the investigation of mechanisms of isolated CO_2 at 1/9 ML, adsorption has been simulated at higher coverages (1/4, 1/3, 1/2, 2/3, 1 ML) in the mono-, bidentate and linear configuration. The resulting binding energies as a function of the CO_2 coverage are shown in Figure 5.9 a. No coverage effect is observed when CO_2 is exclusively physisorbed in a linear configuration. The binding energy is between 0.0 and +0.05 eV for all calculated coverages (1/9-1 ML). The intramolecular geometry of linear CO_2 is not affected by the coverage. However, an increase of the average distance (Δz_{CO_2}) from the surface (Table 5.1) is noticeable with increasing coverage from 1/2 (3.43 Å) to 1 ML (3.92 Å), which can be attributed to repulsive interactions between adsorbates and the formation of a second partial layer of linear CO_2.

In contrast to linearly adsorbed CO_2, a significant influence of the coverage on the binding energy is observed in both carbonate configurations. The bond strength for monodentate species decreases monotonously from E_B=-0.31 to +0.36 eV with increasing coverage from 1/9 to 2/3 ML. This is, similar to the case of linear adsorption, an indication of repulsive interactions between the adsorbates. In fact, no stable configuration for monodentate species at 1 ML is found. Relaxing the geometry of such a configuration results in a mixed state including linear and bent CO_2 species. The change in binding energy of the monodentate configuration is nearly linearly dependent on the coverage up to 1/2 ML (E_B=-0.08 eV) followed by a remarkable increase (loss of bond strength) at 2/3 ML (E_B=+0.36 eV) (Figure 5.8). The diminishing bond strength is accompanied by notable changes in the geometry of the configurations. This is in particular observable in the monodentate configuration at 2/3 ML due to the oversaturation of Ce surface sites. In the stable monodentate configuration, CO_2 interacts with two Ce surface atoms (Figure 5.1 d). Thus, all active sites are occupied already at a coverage of 1/2 ML resulting in a rotation of adsorbed CO_2 away from the corporate surface Ce atom ($Ce_{surf,2}$) at 2/3 ML (Figure 5.10 d) and a drastic decrease in bond strength (increase in E_B, Figure 5.9 a). Furthermore, the distance between the C atom and O_{surf} ($d_{C-O_{surf}}$) of monodentate species increases from 1.38 Å (1/3 ML) to 1.41 Å (2/3 ML) (Figure 5.9 b). No change in $d_{C-O_{surf}}$ is observed at lower coverages. Thus, we conclude that no interactions between adjacent adsorbates are present at coverages <1/3 ML.

Similar trends have been observed in binding energy and geometry of the bidentate species. Here, E_B increases linearly from -0.12 to +0.71 eV with increasing coverage from 1/9 to 1 ML corresponding to a loss in bond strength at high coverages. This indicates repulsive interactions between adsorbates and

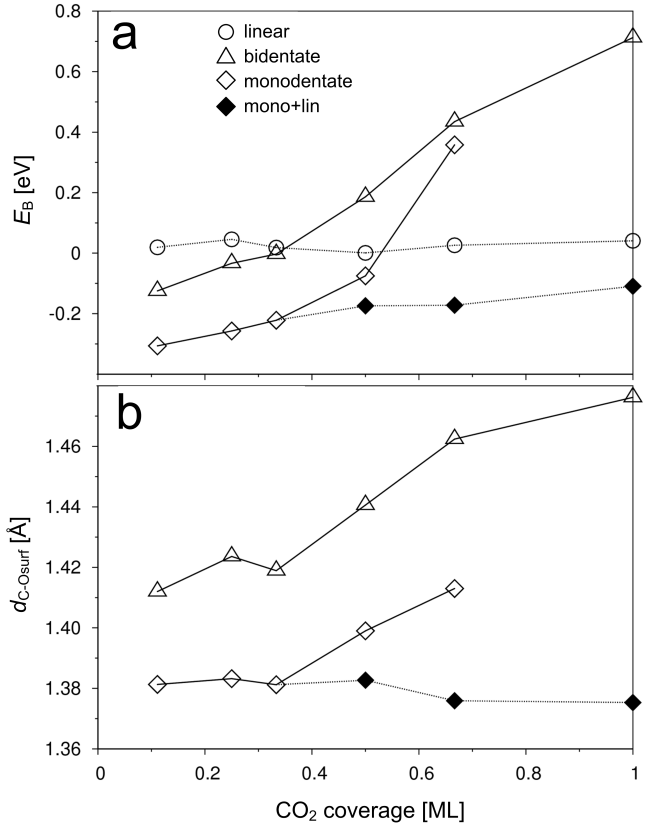

Figure 5.9: (a) Average binding energy E_B and (b) $d_{C-O_{surf}}$ distance as a function of the CO_2 coverage of linear, bidentate and monodentate species and for a mixed configuration with 1/3 ML monodentate species and additional linear CO_2. At 1 ML, the most stable configuration consists of 1/3 ML monodentate and 2/3 ML linear species.

leads to a change from exothermic to endothermic adsorption between 1/3 and 1/2 ML coverage (Figure 5.9 a). Bidentate species interact only with one Ce surface atom which implicates saturation of active sites not until 1 ML coverage and allows for a stable configuration even at 1 ML (Figure 5.10 b,e). In the bidentate configuration, $d_{C-O_{surf}}$ increases only marginally up to 1/3 ML (1.41-1.42 Å) followed by a remarkable increase to 1.48 Å at 1 ML. This suggests a limited capacity of the $CeO_2(111)$ surface to interact with CO_2 molecules.

Electronic Structure The charge transfer between CeO_2 surface and CO_2 adsorbates as a function of the coverage is depicted in Figure 5.11. When CO_2 is adsorbed as monodentate species the charge transferred per CeO_2 surface unit

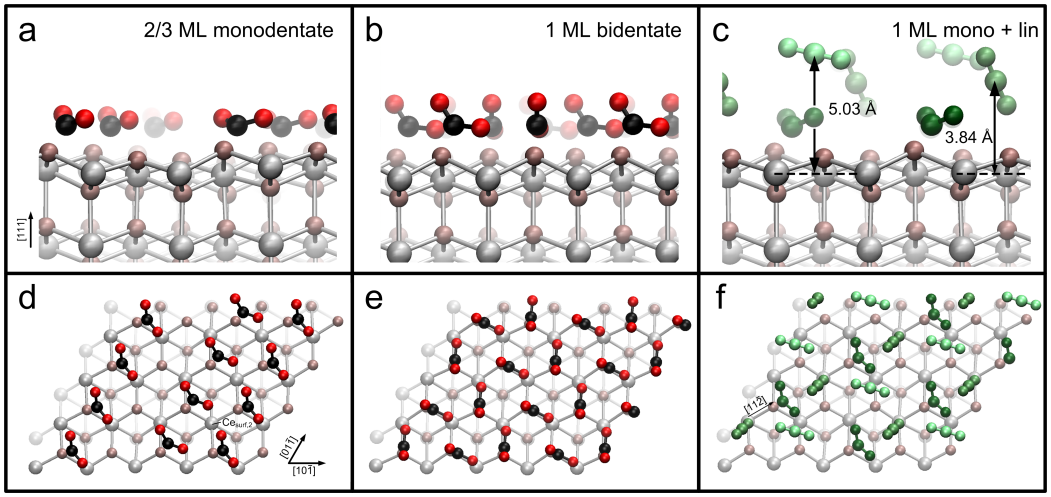

Figure 5.10: (a,b,c) Cross-sectional and (d,e,f) top view of (a,d) monodentate species at 2/3 ML and (b,e) bidentate species and (c,f) a mixed configuration of mondentate and linear species at 1 ML. The two adjacent rows in [01$\bar{1}$] direction of monodentate species at 2/3 ML in (d) share one surface Ce site ($Ce_{surf,2}$) leading to a rotation of the CO_2 molecules away from this Ce atom. When CO_2 adsorbs in a bidentate configuration at 1 ML, the molecules arrange in a zig-zag pattern (e). CO_2 molecules of the mixed configuration are represented with different green spheres to differentiate between various species. The CO_2 molecules of the first partial layer of linear species arrange in [11$\bar{2}$] direction in between the monodentate species at Δz_{CO_2}=3.84 Å. Linear CO_2 adsorbed in a second partial layer are found at Δz_{CO_2}=5.01 Å.

increases linearly with the coverage up to 1/3 ML. At higher coverages, it shows a convex behavior converging towards ca. 0.18 e^-/CeO_2 and demonstrating the limits of CeO_2 as e^- donor. Thus, at coverages >1/3 ML, the CeO_2 substrate is no longer capable of donating the optimal amount of electrons to each adsorbed CO_2 species which contribute to the occupation of LUMO of the unbound species (Figure 5.7 b, state 2), resulting in a loss of bond strength (Figure 5.9 a). It is suggested that interactions between CO_2 adsorbates influence the capacity of each single CO_2 to uptake electrons and thus additionally contribute to a limited charge transfer. This is further supported by the behavior of bidentate species. At low coverage (1/9 ML), basically the same charge is transferred to mono- and bidentate species. However, the convex curvature of the charge transfer already at low coverages causes the curve of bidentate species to lie below the one of monodentate species. Moreover, the charge transfer to bidentate species

converges to 0.13 e^-/CeO_2 at higher coverages which is about 0.05 e^-/CeO_2 lower compared to monodentate species.

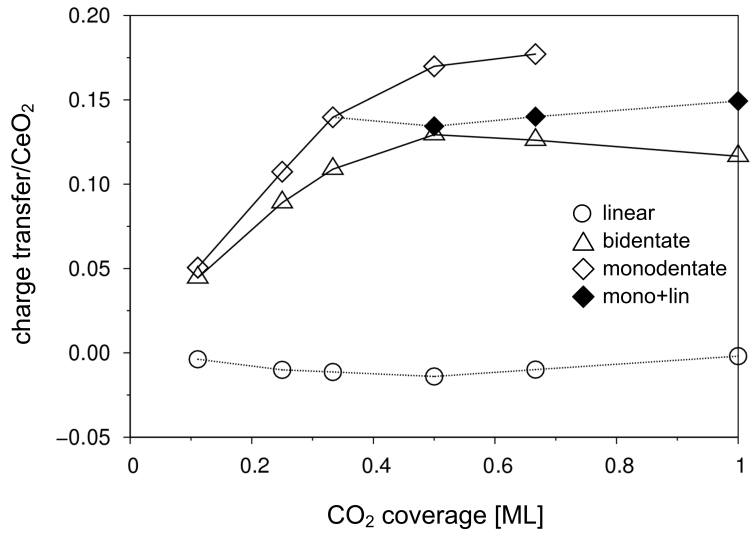

Figure 5.11: Charge transfer per surface CeO_2 unit from the surface to CO_2 adsorbates as a function of the CO_2 coverage for linear (circles), mono- (diamonds) and bidentate (triangles) species and for a mixed configuration (filled diamonds) with monodentate and linear species.

In summary, a CO_2 molecule adsorbed in a bent configuration (mono- and bidentate) acts as Lewis acid accepting electronic charge from the surface at all coverages. The limitation of charge transfer given by the converged value at high coverage can act as a measure of the degree of basicity of the CeO_2 surface. In contrast, in linear adsorption, minor charge transfer (0.009±0.005) is observed from the CO_2 molecule towards the CeO_2 surface. In this case, the surface acts as a weak acid.

5.5 Mixed Adsorption Mechanisms at High Coverage

Stability In addition to the simulations where all CO_2 species adsorb in the same configuration, calculations have been performed at coverages >1/4 ML for mixed adsorption mechanisms where different configurations of CO_2 existed at the same time. At 1/4, 1/2 and 2/3 ML coverage, mixed configurations with monodentate and either linear (mono+lin) or bidentate (mono+bi) species have

been simulated. At 1 ML, additional configurations have been investigated with all three adsorption configurations present simultaneously. The average binding energy for both types of mixed configurations at 1/4 ML shows a linear behavior with increasing fraction of CO_2 adsorbed as monodentate species (Figure 5.12 a). In fact, the pure monodentate adsorption is found to be the most stable configuration at 1/4 ML. The linear decrease in binding energy (increase in bond strength) with increasing amount of monodentate species evidences unperturbed superposition of the binding energies of single-phase configurations (monodentate ratio equal to 0 or 1) indicating negligible interactions between adsorbates.

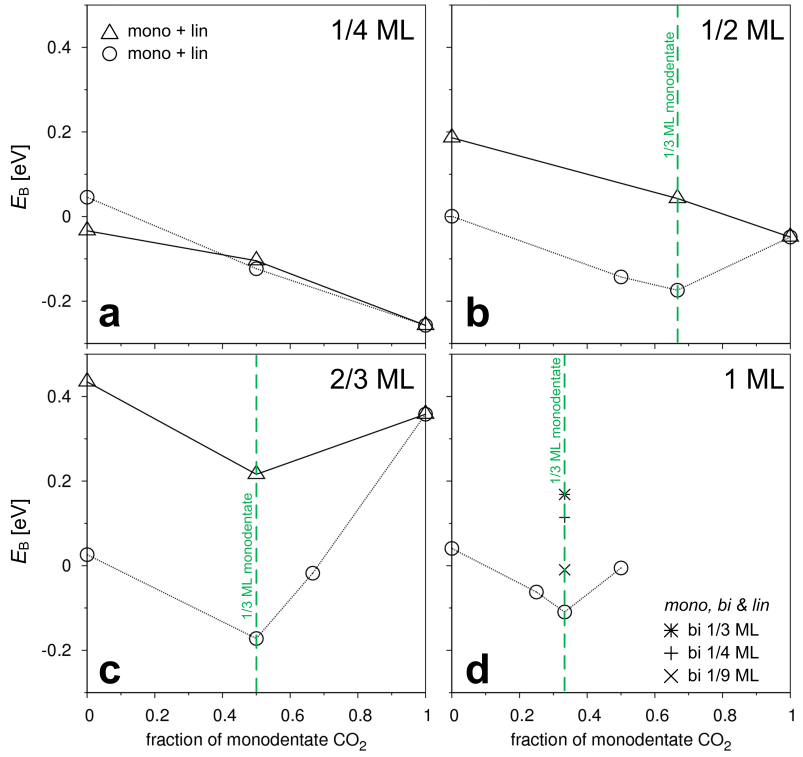

Figure 5.12: Average binding energy of CO_2 adsorbed simultaneously in different configurations at a total CO_2 coverage θ of (a) 1/4, (b) 1/2. (c) 2/3 and (d) 1 ML. The binding energy is shown as a function of the fraction of CO_2 adsorbed as monodentate species at each specific total coverage. At θ >1/2 ML, the binding energy had a minimum when 1/3 ML (green line) of CO_2 adsorbed as monodentate species. At 1 ML (d), the presence of all mono-, bidentate and linear species has been considered with the amount of monodentate species fixed at 1/3 ML.

A similar behavior has been observed at 1/2 ML coverage in the mono+bi con-

figuration (Figure 5.12 b, triangles). In contrast, in the mono+lin (Figure 5.12 b, circles) configuration, the bond strength is maximal (minimum in E_B) when 2/3 of the CO_2 molecules are adsorbed in a monodentate configuration, having a binding energy of -0.17 eV. This ratio of monodentate species corresponds to a coverage of 1/3 ML. It is identical to what is found at 2/3 (Figure 5.12 c) and 1 ML (Figure 5.12 d) for the mixed configurations: the bond strength is maximal for a fraction of monodentate species of 1/2 and 1/3, respectively. Again, in both cases, this fraction corresponds to a total of 1/3 ML of monodentate species. At 1 ML, additional configurations have been calculated at the minimum of E_B, where 1/3 ML monodentate species are adsorbed together with both bidentate and linear species. The coverage of bidentate species in these configurations is 1/9, 1/4 and 1/3 ML. The highest value of E_B (least stable) is found at 1/3 ML of bidentate species and it decreases monotonously with decreasing amount of bidentate species.

In summary, at all investigated coverages a configuration with 1/3 ML monodentate species and additional linear adsorption is found to be most stable. This suggests that CO_2 initially binds as monodentate carbonate to the $CeO_2(111)$ surface up to 1/3 ML and further CO_2 adsorption results in the formation of linear species.

Geometry The geometry of mixed adsorption mechanisms will be discussed here only for the most stable configurations. These are the mixed configurations where 1/3 ML CO_2 is adsorbed as monodentate carbonate and additional CO_2 is adsorbed linearly (Table 5.2). For completeness, results for the configuration with monodentate and linear species at 1/4 ML total coverage are reported as well in Table 5.2.

Table 5.2: Average binding energy (E_B), geometric properties (explained in Figure 5.1), and total charge of CO_2 molecules adsorbed in mixed configurations (mono+lin) on $CeO_2(111)$ at different coverages.

coverage [ML]			E_B [eV]	d_{C-O} [Å]		α_{OCO}[°]		charge	
total	mono	lin		mono	lin	mono	lin	mono	lin
1/4	1/8	1/8	-0.12	1.27	1.17	129.8	178.4	-0.45	0.04
1/2	1/3	1/6	-0.17	1.26	1.17	130.0	177.5	-0.43	0.06
2/3	1/3	1/3	-0.17	1.27	1.17	129.3	177.4	-0.48	0.06
1	1/3	2/3	-0.11	1.27	1.17	129.3	178.6	-0.50	0.03

The C-O bond length (d_{C-O}, Figure 5.1) is significantly larger in the monodentate (1.27 Å) than the linear (1.17 Å) configuration at all coverages, similar to the results in the homogenous adsorption mechanisms. It is independent of the total CO_2 coverage demonstrating that the monodentate species remain in an activated conformation upon further adsorption of linear CO_2 species. Linear species adsorb at different heights depending on the coverage. Linearly adsorbed CO_2 molecules in the first partial layer (1/3 ML) align along the $[11\overline{2}]$ direction in between the monodentate species (Figure 5.10 f) and are on average $\Delta z_{CO_2} \approx 4$ Å above the surface. Starting the optimization from different initial configurations of the first partial layer of linear CO_2 always results in this configuration demonstrating attractive interactions with the monodentate species. Additional CO_2 molecules adsorb at ca. 5 Å above the surface.

As discussed above, the $d_{C-O_{surf}}$ distance for homogeneous adsorption of monodentate species remarkably increases from 1.38 to 1.41 Å with increasing coverage from 1/3 to 2/3 ML (Figure 5.9 b). In contrast, in a mixed adsorption of monodentate and linear species, it remains constant at 1.38 Å. This again indicates that the additional linear molecules do not affect the configuration of the chemisorbed monodentate species.

Electronic Structure In a single-phase monodentate configuration, the average charge of a CO_2 molecule increases steadily with increasing coverage. In contrast, in the mixed mono+lin configuration, the average charge of CO_2 in a monodentate configuration decreases slightly when linear species are additionally adsorbed (Figure 5.13) at a total coverage >1/3 ML. This is accompanied by a small increase in charge of the linear CO_2 species and indicates a charge transfer from the linear to the monodentate species.

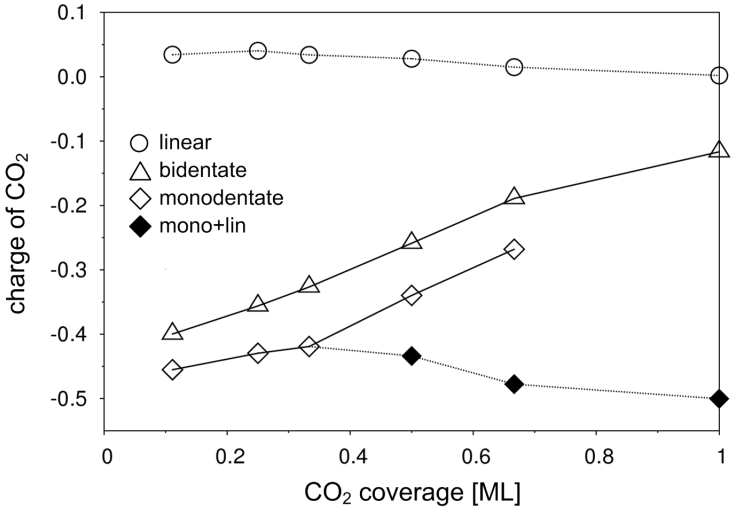

Figure 5.13: Average charge per CO_2 molecule adsorbed linearly (circles) and as bidentate (trianlges) and monodentate (diamonds) species as a function of the CO_2 coverage. Filled diamonds show the charge of the monodentate species (1/3 ML) when additional CO_2 is adsorbed as linear species. In this case, the charge of the monodentate species even decreases slightly with increasing amount of linear CO_2 indicating an additional charge transfer from linear to monodentate CO_2 species.

Figure 5.14 shows the PDOS on the orbitals of the different CO_2 species observed in the most stable mixed (mono+lin) configuration at 1 ML (Figure 5.10 c,f) where 1/3 ML is adsorbed as monodentate species and two partial layers of linear CO_2 are formed. The orbitals of monodentate CO_2 are at the same position as the ones in the isolated monodentate configuration (Figure 5.4). On the other hand, the PDOS of the two different linear species shows the characteristic bands of the gas phase CO_2 molecule. Interestingly, the bands of the linear CO_2 molecules closer to the surface are shifted to slightly lower energies compared to the more distant CO_2 species by ca. 0.4 eV. This demonstrates a stabilization of the first partial layer of linearly adsorbed CO_2 molecules due to the pre-adsorption of monodentate carbonate species and is confirmed by the charge transfer from

linear CO_2 to the bent species and the alignment of the linear species along the axes (Figure 5.10 f).

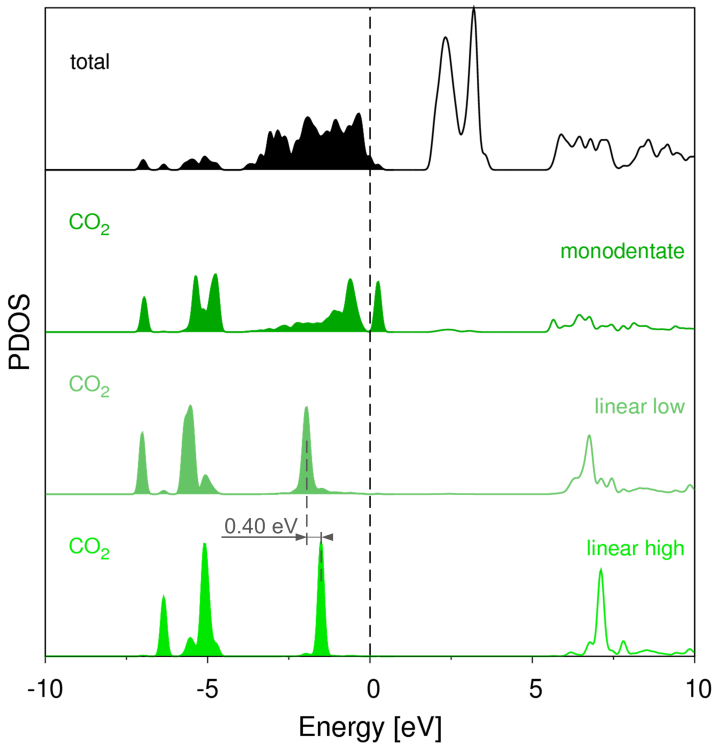

Figure 5.14: PDOS for the mixed configuration with monodentate (1/3 ML) and linear (2/3 ML) species at 1 ML. The PDOS of monodentate CO_2 is identical to the one of the corresponding isolated species (Figure 5.4) while linear CO_2 showed the same bands as the gas phase molecule (Figure 5.7). Molecular orbitals of linear CO_2 adsorbed in the first partial layer (linear low) are located 0.4 eV below the ones of linear species in the second partial layer (linear high).

5.6 Conclusions

Adsorption properties of CO_2 on a $CeO_2(111)$ surface have been investigated with standard DFT calculations using the PBE exchange correlation functional. The capability of standard DFT to properly describe the simulated system has been verified for selected CO_2 configurations on $CeO_2(111)$ using PBE0 and DFT+U calculations. Three stable configurations have been distinguished of isolated CO_2 (1/9 ML) adsorbed on the CeO_2 surface: (i) monodentate carbonate, (ii) bidentate carbonate and (iii) linear species. In both carbonate configurations the CO_2 molecule is bent with the C atom forming a chemical bond with a surface O atom. The chemical bond formation has been confirmed by the change of geometry of the CO_2 molecule and the hybridization of its orbitals with the orbitals of the surface O atom.

Analysis of the PDOS and the differential charge distribution suggest the (partial) occupation of the LUMO of a bent gas phase CO_2 upon adsorption. In contrast to the bent configurations, the linear species is physisorbed without any evidence of hybridization of the CO_2 gas phase orbitals. Geometry and electronic structure of the latter have been found to be identical to the ones of a gas phase CO_2 molecule. Among the three configurations, the monodentate species is the most stable with a binding energy of -0.31 eV.

Upon formation of monodentate carbonate, the C-O bonds elongate to 1.27 Å. This bond length is comparable to the one found for bent CO_2 on several metal surfaces such as Rh, Pd and Pt, indicating a similar CO_2 activation. A charge transfer of 0.46 e^- has been observed from the $CeO_2(111)$ to the monodentate CO_2 species demonstrating the basic character of the $CeO_2(111)$ surface. It is in contrast to what has been reported on some other metal oxides such as TiO_2 [168] where linear adsorption is favored.

The coverage effect has been investigated for the three stable configurations. A decrease in the bond strength with increasing coverage of CO_2 is found in both the monodentate and the bidentate configuration, which can be attributed to the restricted charge transfer capacity of the CeO_2 substrate. This leads to a drastic loss of bond strength at coverages >1/3 ML. The limit for electron donation per CeO_2 surface unit from the substrate to the adsorbate is lower for bidentate than for monodentate species.

Furthermore, mixed configurations have been investigated at coverages >1/4 ML, where monodentate and either bidentate or linear species are adsorbed simultaneously. At 1 ML, additional tri-structural configurations have been examined where mono-, bidentate and linear species are present at the same time. Mixed configurations with monodentate and linear species are found to be most stable at all coverages. Different fractions of monodentate species have been simulated yielding a minimum of the binding energy when an absolute amount of 1/3 ML

of monodentate species is present on the surface.

These results lead us to the conclusion that CO_2 adsorbs as monodentate carbonate on the CeO_2(111) surface up to a coverage of 1/3 ML. At higher coverages, mixed CO_2 configurations are formed where multilayers of linear species adsorb above the monodentate species. The average binding energy in such configurations has been shown to increase marginally to -0.11 eV at 1 ML. Analysis of the density of states has revealed that the first partial layer of linear CO_2 is stabilized by the pre-adsorbed monodentate species.

This study provides fundamental insight in the adsorption properties of CO_2 on CeO_2(111) demonstrating that the CeO_2 surface is capable of activating CO_2 up to a certain coverage (1/3 ML). It is a basis for further investigation of CO_2 reaction mechanisms with hydrogen on CeO_2-based catalytic surfaces. Furthermore, dynamic studies, such as molecular dynamics or meta-dynamics simulations, are planned for direct comparison to experimental results of IR spectroscopy at finite temperature and pressure [158]. These are expected to give a more realistic picture of the different adsorption mechanisms and properties of mixed adsorption at specific process parameters than the static calculations presented in this study.

6

TiO_2-SnO_2 Solid Solutions

6.1 Introduction

Wide band gap semiconductors are used in a wide range of industrially important applications. Tin oxide, for example, is a key component for chemo-resistive gas sensors [8, 9], solar cells (as transparent conductive oxide) [5, 6] and catalysts [169, 170]. Titanium dioxide has found great application as white pigment [171], UV-absorber [172] and photo-catalyst [171]. Both metal oxides exist in the rutile crystal structure at room temperature. The crystal structure of the pure oxides is preserved in $Sn_{1-x}Ti_xO_2$ solid solutions which have demonstrated unique properties with remarkable potential in several applications.

More specifically, the photo-catalytic activity of TiO_2 nanoparticles was enhanced by formation of substitutional solid solution with Sn [173–175]. The distribution of the heteroatom was found to affect catalyst deactivation [176]. More recently Sn-doped TiO_2 was found to exhibit enhanced visible region photocatalytic activity as compared with undoped material in dye degradation experiments [176]. The improved performance was attributed to narrowing of the bulk band gap at low doping levels coupled with the introduction of surface states associated with segregated Sn ions in divalent state. Similarly, the gas sensing performance of SnO_2 nanoparticles, the most widely used sensing oxide, were remarkably improved by Ti doping at low content [17]. In particular, the cross-sensitivity to humidity (a major drawback) of SnO_2-based gas sensors was minimized by Ti-doping at x=4.6 at% content [17]. This is a key step toward the application of chemoresistive gas sensors in breath analysis and thus to non-invasive medical diagnostics as water vapor is omnipresent in the breath.

Application of Ti-doping of other important gas sensing metal oxides requires further understanding of the resulting surface composition and chemical prop-

erties. However, the determination of the surface composition of $Sn_{1-x}Ti_xO_2$ solid solutions and especially of such nanoparticles is still not very advanced. In fact, the spatial distribution of the dopant in the host lattice greatly affects the materials performance and its experimental determination is a challenging and demanding task for nanoparticles. Theoretical investigations may therefore greatly help and pave the way towards a rational design of novel nanomaterials with enhanced performance and optimal composition.

In contrast to pure SnO_2 and TiO_2 crystals, the composition of the rutile $Sn_{1-x}Ti_xO_2$ surface has been barely investigated yet. Density functional theory (DFT) studies have been performed for bulk $Sn_{1-x}Ti_xO_2$ [177] and for very limited contents of Ti-doped SnO_2 [178] and Sn-doped TiO_2 [179], investigating surface relaxation upon substitution on five-fold or six-fold metal sites. Both for SnO_2 [180] and TiO_2 [181], the (110) surface is the thermodynamically most stable and active plane with respect to gas sensing. The computed surface energy (0.53 J/m^2) [182] for rutile TiO_2(110) is considerably lower than that (1.03 J/m^2) [182] of rutile SnO_2(110). Studies on substitutional doping of the rutile SnO_2(110) surface have shown that six-fold metal sites are preferred for substitution in the case of Ru-doping [183], whereas five-fold sites were preferred for Pd-doping [184].

Oxide surfaces have often been simulated effectively by density functional theory using plane-wave formalism with small supercells at k-points convergence [178, 179, 183–186]. However, this limited the minimal surface and total doping content to relatively high values, such as 25 at% and 8.3 at% [178], respectively. Furthermore, symmetric and uniform impurity distributions are forced due to the application of periodic boundary conditions [177] in comparison to the real materials. To investigate the properties of $Sn_{1-x}Ti_xO_2$ solid solutions with low Ti contents ($\leq$4.6 at%), relatively large supercells are required and thus more size efficient formalism such as mixed Gaussian and plane wave (GPW) are required [61, 187]. In fact, the application of the GPW scheme to solve the Kohn-Sham equations allows investigation of metal oxides with several hundreds of atoms with high efficiency [188]. The use of approximated local (LDA) and semilocal (GGA) exchange correlation potentials in DFT limits the accuracy of the calculations. This is in particular apparent in the band gap energy of semiconducting materials which can differ remarkably from experimental results [189, 190, 190], leading, for example, to the incorrect prediction of a metallic character of Ge [28]. However, LDA and GGA are known to well predict ground state properties, such as lattice parameters, surface geometrical displacements, surface energy and adsorption properties [32]. The use of hybrid functionals improves the calculations of band gaps for some semiconductors. However, hybrid functionals are computationally more demanding than LDA or GGA and sometimes less accurate than GGA functionals, for example in the prediction of cohesive energies of metals [32].

Here, DFT calculations based on the GPW method [61, 187] have been used

to determine the lattice parameters and adsorption properties of ideal (without defects) rutile $SnO_{1-x}Ti_xO_2(110)$ surfaces as a function of the Ti distribution. In this way, it has been possible to investigate the properties of highly asymmetric systems from high to very low Ti content (x=1.3 at%). Three types of Ti atoms distributions have been investigated: (i) homogeneous Ti distribution in the bulk, (ii) homogeneous distribution in the surface layer, and (iii) segregated distribution in the surface layer. The restructuring of the surface has been quantified by the structural changes of the metal and oxygen atoms at the surface with respect to the bulk. The thermodynamic stability of the resulting crystals has been evaluated based on their surface energy.

6.2 Methods

DFT calculations have been carried out based on the description in section section 2.2.3. For Sn and Ti atoms, four and twelve electrons, respectively, are explicitly considered in the valence shell. A double-ζ valence plus polarization (DZVP) basis set, optimized according to the Mol-Opt method [62], is adopted for the metal atoms. For O atoms, six valence electrons are considered and a triple-ζ valence basis set with polarization (TZVP) is used. For auxiliary PW expansion of the charge density, an energy cutoff of 400 Ry has been determined to be necessary to achieve the energy convergence in the reciprocal space.

The bulk supercell is obtained by multiplication of the orthorhombic rutile primitive cell (Figure 6.1) in all spatial directions. Convergence of the wave function has been reached with three, four and ten unit cells in the x-, y- and z-direction, respectively. This expansion roughly corresponds to the use of an unshifted (3x4x10) k-points grid. The resulting supercell consists of 720 atoms (240 metal (Me) and 480 oxygen atoms).

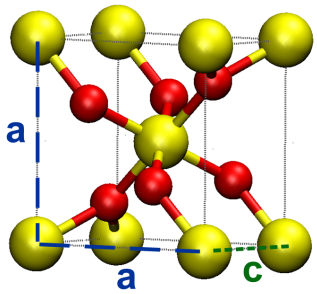

Figure 6.1: Orthorhombic unit cell of the rutile crystal structure, phase group $P4_2mnm$, with lattice parameters a and c.

All simulations have been performed with periodic boundary conditions. Determination of the optimal lattice parameters a and c and the internal parameter u (Table 6.1) has been carried out by self-consistent wave function calculations for different lattice values until the convergence in the total energy has been lower than 10^{-3} eV per O_2-metal atom unit of the super cell. The optimization of the lattice parameters has been done for different cell sizes (96, 216 and 720 atoms). For pure SnO_2, the lattice constant a increases from 4.80 to 4.86 Å, while c decreases from 3.32 to 3.28 Å with increasing cell size from 96 to 720 atoms. To determine the total energy of the bulk, all atom positions are allowed to relax starting from the optimal lattice parameters.

Surface calculations are performed using the supercell optimized for bulk calculations. In addition, 20 Å of vacuum have been added along the z-direction in order to avoid any interaction of the slab with its periodic images. The surface explicitly contains 60 atoms (including bridging oxygen atoms), 24 of which are metallic. Five metal atom layers are sufficient for simulation of the $SnO_2(110)$ surface [191–193]. Here, ten Me atom layers have been used to obtain convergence of the systems electronic properties. Three atomic layers on the top and the bottom of the slab are allowed to relax in all dimensions, while the four central layers are fixed in order to simulate the bulk properties.

For $Sn_{1-x}Ti_xO_2$ solid solutions, three different distributions of Ti atoms in the rutile SnO_2 crystal have been considered: (i) homogeneous distribution in the bulk, (ii) homogeneous distribution in the surface layer, and (iii) segregated in the surface layer. One possible configuration has been calculated for each Ti content and distribution in the bulk. For surface enriched distributions, (i) and (ii), the amount of substituted Sn_{5c} and Sn_{6c} atoms is the same. Additional calculations have been performed for Ti located only on 5c or 6c sites. The percentages given always refer to the atomic percentage.

The surface energy E_S has been calculated according to eq. (6.1), where E_{bulk} and E_{surf} is the total energy of the bulk metal oxide and its (110) surface slab, respectively, and the exposed surface area on one side of the slab is A (here, $12ac$) [95].

$$E_S = \frac{E_{surf} - E_{bulk}}{2A} \tag{6.1}$$

The total energy of the relaxed bulk E_{bulk} is always calculated for a random distribution of Ti atoms in bulk SnO_2. Therefore, E_S for surface enriched (ii and iii) solid solutions represents the difference in energy of the bulk and the state after creation of the surface and diffusion of Ti atoms to the surface per unit surface area. The thermodynamically most favorable Ti distribution is determined by comparison of the surface energies of the different configurations. This approach has been used previously for other mixed metal oxide systems such as Ru-doped

[183] and Pd-doped SnO_2 [184].

6.3 Bulk Structure of $Sn_{1-x}Ti_xO_2$ Rutile Crystals

The rutile crystal structure of the pure metal oxides and their solid solutions with varying Ti content has been optimized determining bulk modulus and lattice parameter. Table 6.1 reports experimental lattice parameters (a, c, u) and the ones computed here and in other DFT studies. The calculated values are in good agreement with other DFT studies utilizing the same [182] and other [193] exchange correlation potentials (Figure 6.2). The calculations overestimate the experimental lattice values (Table 6.1) for all systems [17, 194, 195]. However, the difference between experimental and DFT values, computed here, was lower than 5% (Table 6.1, Figure 6.2). This shift is commonly observed in DFT calculations of periodically repeated crystal slabs as they experience an artificial stress by the periodic boundary conditions, even after relaxation [191]. Additionally, even with the same boundary conditions, the use of different exchange correlation functionals leads to slight variations of the computed lattice parameters (Figure 6.2).

Table 6.1: Lattice parameters of SnO_2, TiO_2 and their solid solutions.

	x [%]	a [Å]	c [Å]	u	reference
SnO_2	0	4.856	3.278	0.3069	this work
		4.828	3.245	0.3065	PW-PBE [182]
		4.737	3.186	0.3056	experimental [194]
$Sn_{1-x}Ti_xO_2$	1.7	4.856	3.278	0.3069	this work
	3.3	4.856	3.278	0.3069	this work
	6.7	4.836	3.260	0.3069	this work
	14	4.836	3.260	0.3069	this work
	20	4.810	3.220	0.3061	this work
TiO_2	100	4.640	2.980	0.3053	this work
		4.653	2.972	0.3049	PW-PBE [182]
		4.594	2.959	0.3050	experimental [194]

Here, the use of a large supercell with 720 atoms allowed to map the evolution of the solid solution properties from very low (1.7%) to high (20%) Ti content.

Up to 3.3% Ti, the optimized lattice parameters (Table 6.1) did not diverge from those of pure SnO_2. Increasing further the Ti content (>3.3% Ti) both lattice constants (a and c) decrease (Table 6.1) in agreement with the smaller ionic radius of Ti (0.6 Å) compared to Sn (0.7 Å) [196]. However, both lattice parameters (Figure 6.2 and Table 6.1) did not decrease linearly with increasing Ti content. This variation from Vegard's law (i.e. a linear relationship between the values of pure oxides) has been reported previously in experimental [8, 176] and computational studies [177]. A similar behavior has been observed for other Sn-based systems (e.g. $Sn_{1-x}Sb_xO_2$) [197]. Previously, it has been attributed to the different compressibilities and thermal expansivities of the constituents, SnO_2 and TiO_2 [198, 199]. The small differences (<5%) between the lattice parameters computed here (Figure 6.2, filled triangles) and those previously reported using the PW formalism and a ten times smaller supercell (72 atoms) (Figure 6.2 squares) [177] are within the variation reported for different DFT studies.

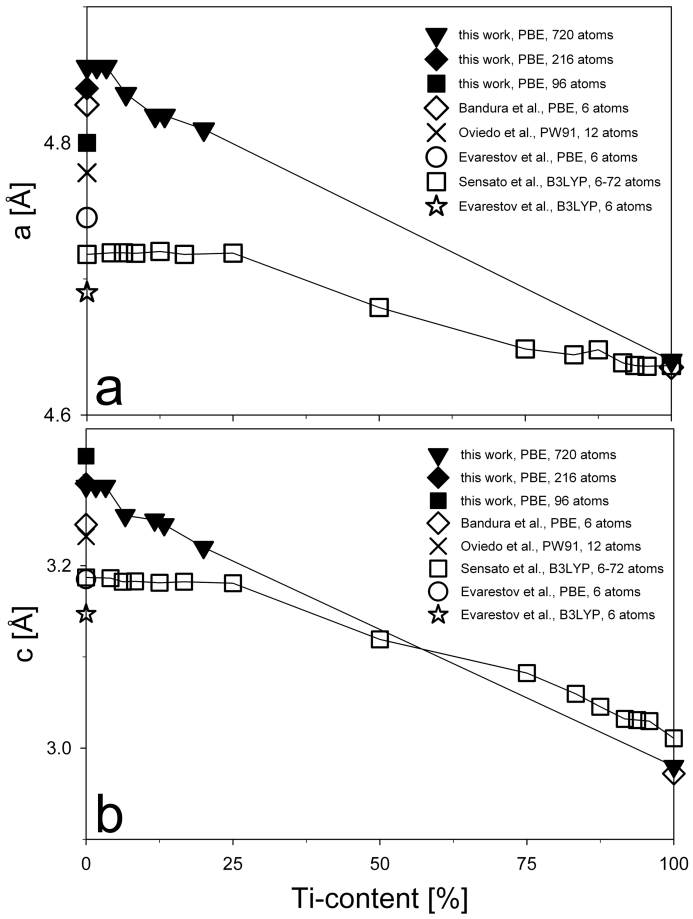

Figure 6.2: Lattice parameters (a) a and (b) c of $Sn_{1-x}Ti_xO_2$ solid solutions compared to several computational studies, applying different exchange correlation potentials, by Bandura et al. [182], Oviedo et al. [193], Evarestov et al. [180] and Sensato et al. [177].

6.4 Relaxation of the Rutile (110) Surface

6.4.1 Pure SnO_2

Figure 6.3 shows the rutile (110) surface of pure SnO_2. For the Ti-containing systems, the Sn atoms have been substituted by Ti atoms according to their final content and type of distribution. In the following, surface metal atoms bound to five and six neighboring O atoms are denoted as Me_{5c} and Me_{6c}, respectively. Rooted O atoms that are located in the surface layer are denoted as O_r, whereas bridging O atoms are named as O_{br} (Figure 6.3, inset). Table 6.2 summarizes the bond lengths and z-shifts of the surface atoms.

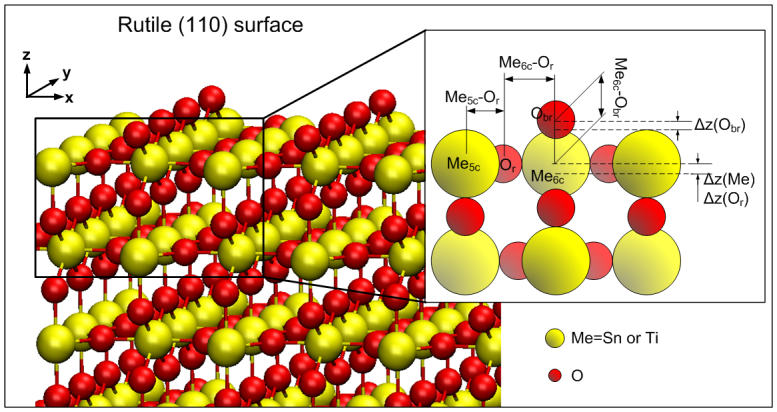

Figure 6.3: Peripheral view of rutile SnO_2(110) (Me_{5c} and Me_{6c} =yellow, O_r and O_{br} =red). For $Sn_{1-x}Ti_xO_2$ solid solutions, the metal atoms (Sn and Ti) are substituted according to the total Ti content (x). The inset shows a schematic illustration of the cross-sectional view with geometric parameters of the relaxed surface (reported in Table 6.2 and Table 6.3): shift of surface atoms in z-direction (Δz(Me), Δz(O)) and bond lengths between metal and oxygen atoms (Me_{5c}-O_r, Me_{6c}-O_r, Me_{6c}-O_{br}).

As mentioned previously, the investigation of solid solutions has been carried out for three Ti atom distributions: (i) a homogeneous one in the bulk (Figure 6.4 a,b), (ii) a homogeneous one in the surface layer (Figure 6.4 c,d), and (iii) a segregated one in the surface layer (Figure 6.4 e,f). In the supercell used here, two of the ten metal atom layers are exposed surface layers. Therefore, for surface enriched configuration, (ii) and (iii), the surface Ti content is five times higher than the total Ti content. A total Ti content of 20% thus corresponds to 100% surface Ti content. The resulting slab specific surface area is reasonably close to that (100 m^2/g) of flame-made $Sn_{1-x}Ti_xO_2$ nanoparticles (d_{BET}=10 nm)

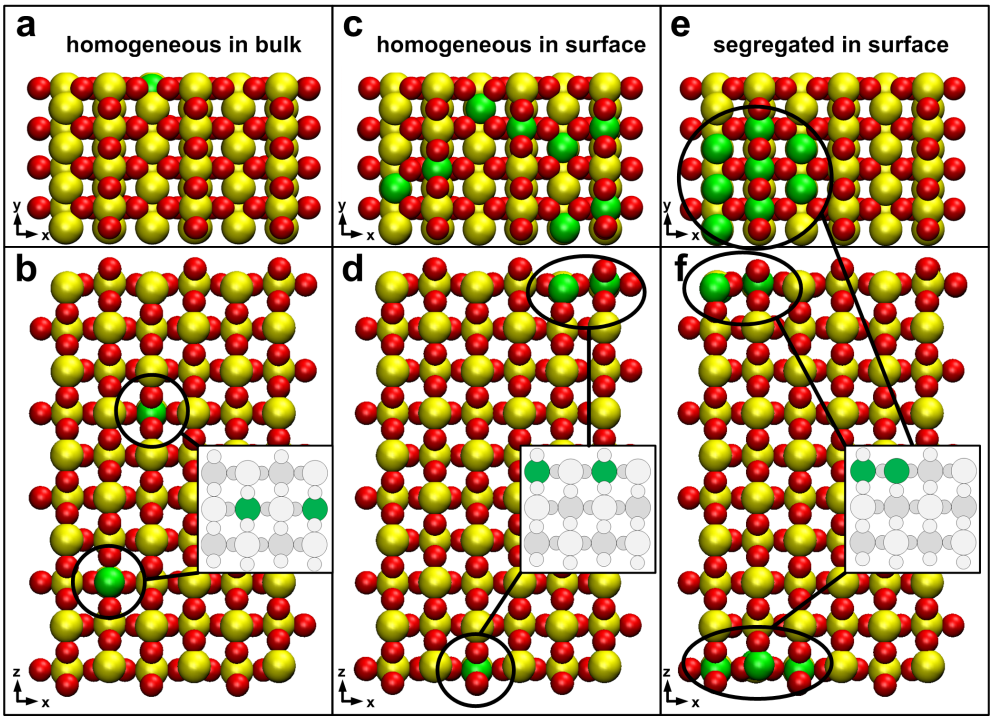

Figure 6.4: Relaxed rutile (110) surfaces with three different distributions of Ti atoms in the $Sn_{1-x}Ti_xO_2$ crystal (Sn=yellow, Ti=green, O=red) having a total Ti content of 6.7%. Top and cross-sectional views of homogeneous Ti distribution in the bulk (a,b), homogeneous Ti distribution in the surface (c, d) and segregated distribution in the surface (e,f).

previously utilized as gas sensors [17]. All graphs are shown as a function of the total Ti content. The properties of the (110) surface upon relaxation will be first discussed for pure SnO_2 and TiO_2 and then for their solid solutions.

Upon relaxation of pure (110) SnO_2, the Sn_{5c} atoms move into the surface by 0.18 Å while the Sn_{6c} atoms move out by 0.11 Å (Table 6.2). A similar z-shift is seen for O_r atoms which move outwards by 0.09 Å while only marginal displacements are observed for O_{br} atoms (Table 6.2), consistent with previous studies [182]. Here, with respect to the bulk, the Sn_{6c}-O_r bond length increases by 2.8% while the Sn_{5c}-O_r and Sn_{6c}-O_{br} bond lengths decrease by 0.9% and 4.3%, respectively. An analogous decrease of the Sn_{6c}-O_{br} (3.6%) has been reported previously [183].

Table 6.2: Geometrical properties of SnO_2, TiO_2 and $Sn_{1-x}Ti_xO_2$ solid solutions when Ti atoms are distributed homogeneously in the bulk. Results of the pure SnO_2 and TiO_2 are compared to previous DFT calculations [180, 182, 200]. Where a range of values is given for (Me_{6c}-O_r), the standard deviation of all considered values is larger than 0.01 Å.

x [%]	Me-atom	(Me_{5c}-O_r) [Å]	(Me_{6c}-O_r) [Å]	(Me_{6c}-O_{br}) [Å]	Δz (Me_{5c}) [Å]	Δz (Me_{6c}) [Å]	Δz (O_r) [Å]	Δz (O_{br}) [Å]	
0	Sn	2.09	2.17	2.02	-0.18	0.11	0.09	-0.03	
		-	2.01	-	-0.10	0.06	0.18	0.06	[182]
		-	-	-	-0.12	0.09	0.11	-0.09	[200]
1.7	Sn	2.09	2.17	2.02	-0.18	0.11	0.08	-0.03	
3.3	Sn	2.09	2.17	2.02	-0.19	0.12	0.10	-0.03	
6.7	Sn	2.08	2.15	2.02	-0.16	0.19	0.14	0.05	
14	Sn	2.08	2.13-1.16	2.01	-0.18	0.18	0.09	0.05	
20	Sn	2.07	2.14	2.01	-0.16	0.20	0.14	0.09	
100	Ti	1.96	2.05	1.83	-0.20	0.18	0.10	-0.04	
		-	1.83-1.85	-	-0.16	0.20	0.17	0.00	[182]
		-	-	-	-0.12	0.21	0.14	0.05	[180]

Table 6.3: Geometrical properties of surface enriched $Sn_{1-x}Ti_xO_2$ solid solutions. Ti atoms are distributed either homogeneously or segregated in the surface layer. Where two different values are given for (Me_{5c}-O_r) or (Me_{6c}-O_r), the respective bond lengths indicate an asymmetric behavior. Where a range of values is given, the standard deviation of all considered values is larger than 0.01 Å.

	x [%]	Me-atom	(Me_{5c}-O_r) [Å]	(Me_{6c}-O_r) [Å]	(Me_{6c}-O_{br}) [Å]	Δz (Me_{5c}) [Å]	Δz (Me_{6c}) [Å]	Δz (O_r) [Å]	Δz (O_{br}) [Å]
homogeneous	3.3	Sn	2.08-2.13	2.14-2.22	2.03/2.10	-0.16	0.10	0.09	-0.06
		Ti	1.96-2.06	2.11-2.14	1.80	-0.26	0.23		
	6.7	Sn	2.08-2.15	2.15-2.23	2.04/2.09	-0.14	0.13	0.09	-0.04
		Ti	1.92-2.09	2.09-2.19	1.80	-0.25	0.24		
	14	Sn	2.06-2.23	2.17-2.27	2.07-2.10	-0.11	0.06	0.07	-0.11
		Ti	1.79-2.37	1.99-2.39	1.75-2.10	-0.23	0.19		
segregated	3.3	Sn	2.08-2.17	2.13-2.26	2.06/2.06-2.12	-0.17	0.11	0.08	-0.06
		Ti	1.92-2.02	2.05-2.16	1.79-1.86	-0.27	0.17		
	6.7	Sn	2.07-2.15	2.10-2.27	2.02/2.15	-0.12	0.17	0.13	-0.01
		Ti	1.84-2.17	2.00-2.22	1.81-1.90	-0.23	0.17		
	14	Sn	2.07-2.29	2.13-2.44	2.01/2.14	-0.10	0.16	0.08	-0.06
		Ti	1.79-2.40	2.01-2.25	1.74-2.13	-0.21	0.17		
	20	Ti	1.77-2.76	2.00-2.46	2.01	-0.16	0.18	0.11	-0.12

6.4.2 Pure TiO_2

For pure TiO_2, the z-shifts of surface atoms are qualitatively similar to those of SnO_2. The magnitude, however, of their geometrical displacements (Table 6.2) is larger than for SnO_2. More in detail, Ti_{5c} atoms move into the surface by 0.20 Å while Ti_{6c} atoms move out of it by 0.18 Å. Rooted oxygen (O_r) atoms move out of the surface by 0.10 Å, whereas O_{br} atoms move only slightly (0.04 Å) towards the surface. The z-shifts of surface atoms on TiO_2 are in line with experimental [201] and theoretical [182] studies.

The relaxation of the surface leads to a similar behavior of the Ti-O bond length compared to what has been computed for SnO_2. The Ti_{5c}-O_r bond length decreases slightly (0.5%), whereas the Ti_{6c}-O_r bond increases by 2.5%. Prominently, the decrease of Ti_{6c}-O_{br} bond length is 8.3% and thus remarkably higher than that (4.3%) of SnO_2. The larger extent of surface rearrangement on TiO_2 than on SnO_2(110) suggests an enhanced stabilization of its surface and is consistent with the literature [179].

6.4.3 $Sn_{1-x}Ti_xO_2$ Solid Solutions

For homogeneous Ti distributions (Figure 6.4 a) in the bulk (i), the presence of Ti atoms marginally affects the geometry of the (110) surface (Table 6.2 and Figure 6.5) indicating only small interaction between bulk and surface layers. More specifically, only the Sn_{6c}-O_{br} bond length (Figure 6.5, diamonds) decreases slightly from 2.02 to 2.01 Å with increasing Ti content from 0 to 20% while the other geometrical properties remain nearly identical to those computed for the pure SnO_2 surface (Table 6.2).

For homogeneous (ii) and segregated (iii) Ti distribution in the surface (Figure 6.4 c-f), it is necessary to distinguish between Sn atoms sharing (Ti-affected) and not sharing (Ti-free) an O atom with a Ti atom. In fact, for both bulk and surface Ti distributions, hardly any variation from the Sn_{6c}-O_{br} bond length of pure (110) SnO_2 is observed for the Ti-free Sn atoms (Figure 6.6). In contrast, the Sn_{6c}-O_{br} bond length of Ti-affected Sn atoms (Figure 6.5 a, filled triangles) is always 0.7 Å higher than that (2.02 Å) of Ti-free Sn atoms (Figure 6.6) and does not vary with the Ti content. As a result, for homogeneous Ti distribution in the surface (ii), the average Sn_{6c}-O_{br} bond length (Figure 6.5 a, open triangles, Table 6.3) increases steadily with increasing Ti content in agreement with the increasing number of Ti-affected Sn atoms.

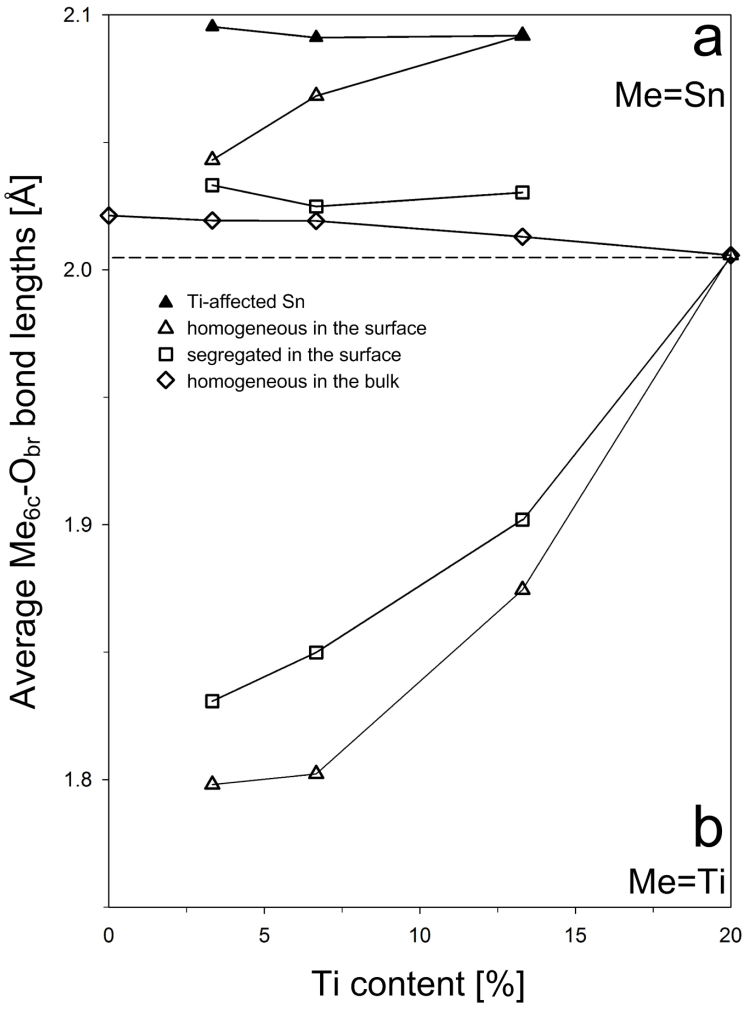

Figure 6.5: Average bond length of (a) Sn_{6c}-O_{br} and (b) Ti_{6c}-O_{br} in Å as a function of the Ti content. For Ti atoms homogeneously distributed in the SnO_2 lattice (a, diamonds), the Sn_{6c}-O_{br} distance is nearly constant with increasing Ti content. For a homogeneous Ti distribution in the surface layer, the Sn_{6c}-O_{br} bond length of Ti-affected Sn atoms (a, filled triangles) is constant and higher than that of the pure SnO_2 surface while the average Sn_{6c}-O_{br} bond length (a, open trianlges) increases linearly with increasing Ti content. The Ti_{6c}-O_{br} bond increases continuously both for segregated (b, squares) and homogeneous (b, open triangles) Ti distribution in the surface.

For segregated Ti distribution in the surface (iii), the average Sn_{6c}-O_{br} bond length (Figure 6.5 a, squares) is nearly constant with increasing Ti content since the number of Ti-affected Sn atoms increases only slightly. The effect of the change in the bond lengths is attributed to the higher electronegativity of Sn (1.8) compared to Ti (1.4) atoms [182] which causes a smaller distance between Ti and O than between Sn and O atoms and leads to an asymmetric arrangement of surface atoms. The increase of the Sn_{6c}-O_{br} bond length with adjacent Ti atoms is expected to change the bond character and strength between Sn_{6c} and O_{br} atoms, and also the top surface charge of both Sn_{6c} and O_{br} [180]. This is of particular relevance as for several molecules (e.g. CO or NO) oxidation by the bridging oxygen (O_{br}) of the metal oxide surface [156] is an important step of their catalytic reactions. This redox mechanism is influenced by the surface top charge of the involved surface species and thus the change of Sn_{6c}-O_{br} bond length, computed here, may affect remarkably the potential energy surface of several important catalytic reactions.

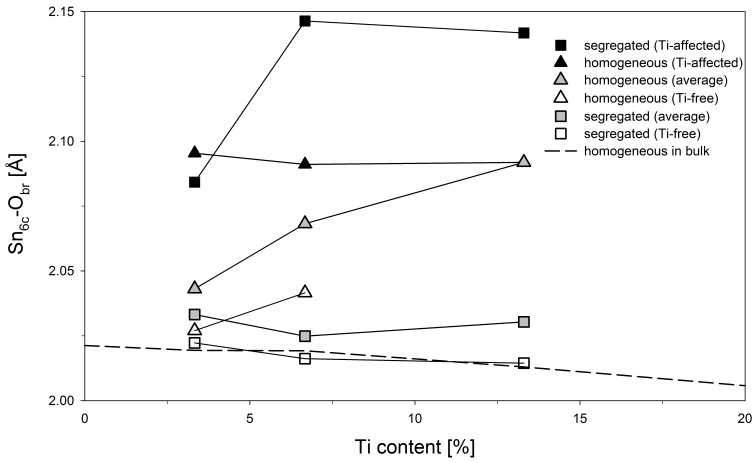

Figure 6.6: Average Sn_{6c}-O_{br} bond length for specific types of Sn_{6c} atoms. Sn_{6c} atoms that are not affected by neighboring Ti atoms (Ti-free) have a similar bond length to O_{br} both for segregated (open squares) and homogeneous (open triangles) Ti distribution in the surface than the ones for homogeneous Ti distribution in the bulk (dashed line). A remarkable increase of the Sn_{6c}-O_{br} bond length is observed when Sn is affected by a neighboring Ti_{6c} atom. At a Ti content greater than 6.7% the Sn_{6c}-O_{br} bond length is larger for a segregated (grey squares) than for a homogeneous (grey triangles) Ti distribution in the surface layer.

For the homogeneous Ti distribution in the surface (ii), at low Ti content ($\leqslant$6.7%) the Ti_{6c}-O_{br} bond length (Figure 6.5 b, triangles) was $\leqslant$1.80 Å and thus

slightly lower than that (1.83 Å) of the pure TiO_2 surface despite the greater lattice parameters of its host crystal structure. This is attributed to the higher electronegativity of Sn (see discussion above), which leads to an asymmetric shift of the O_{br} atoms towards the Ti_{6c} atoms. At higher Ti content, more Ti atoms are present in the surface layer having the same affinity towards O atoms. This leads to a more even distribution of surface atoms and thus longer Ti_{6c}-O_{br} bonds. Increasing the Ti content increases remarkably the Ti_{6c}-O_{br} bond length (Figure 6.5 b, triangles). In fact, at 20% total Ti content, it reaches the value of the Sn_{6c}-O_{br} one for (iii) homogeneous distribution in the bulk (Figure 6.5 a, diamonds). This content (20%) corresponds to 100% surface coverage of Ti atoms.

As a result, O atoms are attracted equally by the Ti_{6c} atoms, similar to the pure TiO_2 surface, but the size of the rutile lattice is determined by the Sn atoms in the bulk. As a result, the same Me_{6c}-O_{br} bond length is obtained for Ti and Sn (Figure 6.5). It has been previously suggested that the dimensions of the unit cell are a main factor determining the adsorption mode of H_2O on rutile type crystals such as SnO_2 and TiO_2 [182]. More in detail, it is expected that large unit cell dimensions lead to the formation of weaker H-bonds favoring dissociative H_2O adsorption as observed for SnO_2 and in line with its larger (than TiO_2) lattice constants [182]. Furthermore, it has been shown that decreasing the lattice parameters of Pt(111) and thus introducing compressive surface strain greatly affects adsorption properties of O_2, O, CO and CO_2 on its surface [202]. Therefore, here, it is expected that the adsorption properties of several important species (e.g. H_2O, ethanol, NO_x, O_2 and CO) could be strongly affected as, for example, the 20% Ti distribution on the SnO_2 surface leads to a full TiO_2 monolayer having, however, the unit cell dimension of the underlying SnO_2 crystal.

For segregated distributions of Ti atoms in the surface (iii), the Ti_{6c}-O_{br} bond length (Figure 6.5, squares) shifts to larger values but shows similar behavior as for homogeneous Ti surface (ii) distributions. This is also attributed to the effect of neighboring Ti_{6c} atoms attracting the O atoms with equal force and thus the bond length is influenced by the lattice parameters of the underlying crystal. A similar behavior of the Me_{6c}-O_{br} bond length has been reported previously for Ru-doped SnO_2 rutile systems [183].

6.5 Thermodynamic Stability of the (110) Rutile Surface

The thermodynamic stability of the pure metal oxide and solid solution surfaces has been evaluated by their surface energy (Figure 6.7) as a function of Ti content and distribution. For pure SnO_2, a surface energy of 0.99 J/m^2 has been computed in reasonable agreement with literature reporting values between 1.03 and 1.28 J/m^2 [180, 182, 193]. In comparison, the surface energy of TiO_2 (0.46 J/m^2) is remarkably lower than SnO_2 (Figure 6.7). This is again in agreement with previous studies reporting values from 0.53 to 0.90 J/m^2 for the (110) rutile TiO_2 surface [180, 182, 193]. Furthermore, these results confirm the higher stability of the TiO_2 surface compared to that of SnO_2. This can be partly explained by the more extensive geometric rearrangement upon relaxation of TiO_2 compared to SnO_2 (Table 6.2).

For homogeneous Ti distribution in the bulk (i), the surface energy (Figure 6.7, diamonds) of solid solutions decreases marginally from 0.99 to 0.96 J/m^2 with increasing Ti content from 0 to 20%. This is in agreement with the homogeneous composition of its surface and the small variation of the Sn_{6c}-O_{br} bond length upon relaxation (Figure 6.5, diamonds). In contrast to bulk Ti distributions, the surface energy (Figure 6.7, circles and triangles, respectively) decreases from 0.99 to 0.74 J/m^2 with increasing Ti content from 0 to 20% for both homogeneous (ii) and segregated (iii) surface Ti distributions. Surprisingly, the surface energy for both segregated and homogeneous Ti distribution is always identical. This suggests that the surface energy depends only on the number of Ti atoms in the surface layer but not on the distribution. However, even at 100% surface Ti content (20% total Ti content), the surface energy (Figure 6.7) does not reach the value of the pure TiO_2 indicating that the underlying SnO_2 bulk is destabilizing the TiO_2 surface layer with respect to the pure TiO_2 surface. For both (ii) and (iii) distributions, the amount of substituted Sn_{5c} and Sn_{6c} atoms has been the same resulting in the same amount of energy required for the breaking of Ti-O and Sn-O bonds.

To investigate the influence of the Ti atom position for surface distribution, exclusive Ti substitution on 5c and 6c Sn surface sites has been computed for 3.3%, 6.7% and 10% total Ti content (Figure 6.7, inlet). Both for Ti substitution on 6c and 5c surface sites, the resulting surface energy is lower than that for homogeneous Ti distribution in the bulk in line with the observed surface stabilization by its enrichment with Ti. For all Ti contents, Ti substitution on 6c sites results in the lowest surface energy suggesting that, at low Ti content, 5c sites may actually remain occupied by Sn atoms.

Furthermore, the surface energy for homogenous Ti distribution on the surface

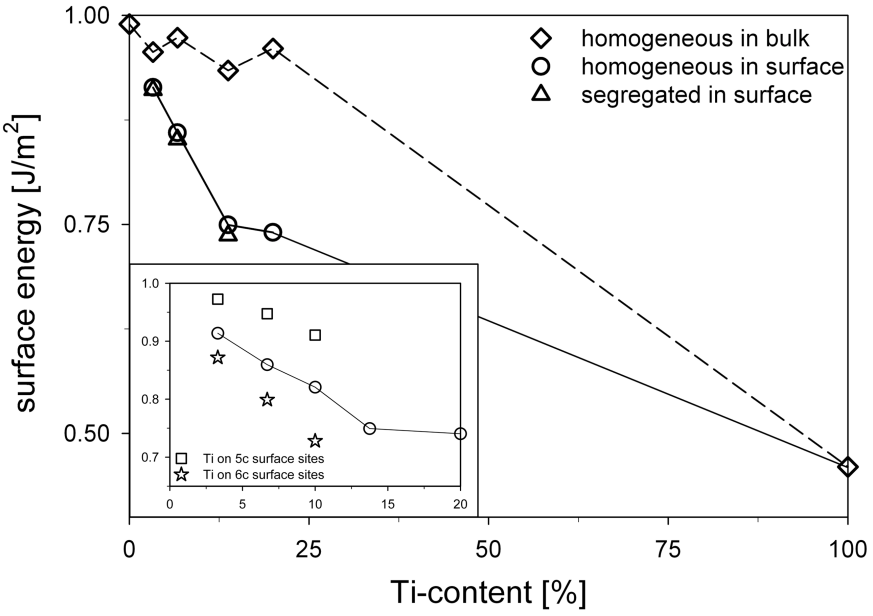

Figure 6.7: Surface energy of $Sn_{1-x}Ti_xO_2(110)$ as a function of the total Ti content when Ti atoms are distributed homogeneously in the bulk (diamonds) and homogeneously (circles) and segregated (triangles) in the surface layer. For surface enriched configurations, the surface energy decreases remarkably from 0.99 to 0.75 kJ/mol with increasing Ti content from 0 to 20%. The inset shows a magnification of the region from 0 to 20% Ti content when Ti atoms are distributed specifically on 5c (squares) and 6c (stars) surface sites showing 6c sites to be favored.

is always between that for substitution on 5c and 6c sites. Thus, it is expected that for different distributions of Ti on the $Sn_{1-x}Ti_xO_2$ surface than the one computed, the surface energy will be enclosed between the maximal and minimal values given by exclusive Ti substitution on the 5c and 6c sites, respectively. Apparently, in the (110) $Sn_{1-x}Ti_xO_2$ rutile surface, two effects are responsible for the computed drop in surface energy by increasing the surface Ti content. First, less energy is required to break Ti-bonds than Sn-O ones. Second, the proximity of Ti_{6c} atoms destabilizes the residual Sn-O bonds that have to be broken for surface creation. Both effects contribute to the lower surface energy of $Sn_{1-x}Ti_xO_2$ with surface Ti distributions (ii and iii) than with bulk ones (i).

It is in fact surprising that Ti-doping of SnO_2 nanoparticles had a dramatic impact on the rutile surface reaction with H_2O already at 4.6% Ti content [17]. In agreement with our finding, this could be attributed to local effects such as Ti surface enrichment and/or strong interaction with neighboring Sn atoms. The

findings of energetically favored Ti distributions on the SnO_2 surface have also implication for catalytic processes. Adsorption properties of catalytically interesting species such as CO [203, 204], CO_2 or NO_x [205] can be drastically changed and improved by additional surface Ti sites as it has been shown previously for other mixed metal oxides [203, 206–208]. Furthermore, it is expected that the adsorption properties on Sn sites could be affected by the neighboring Ti surfaces sites. However, to determine the catalytic activity of such $Sn_{1-x}Ti_xO_2$ surfaces a dedicated study should be performed on the adsorption properties of the interesting species and the activation barriers of the corresponding reactions. Finally, it should be stressed that our theoretical study of the composition of $Sn_{1-x}Ti_xO_2$ solid solutions surfaces reflects the situation under idealized conditions (vacuum, 0K, perfect crystal surface). In practical applications some deviation from this ideal behavior may occur due to interaction with adsorbed molecules from the surrounding medium which forms the interface with the $Sn_{1-x}Ti_xO_2$ surface, and effects caused by temperature and surface defects.

6.6 Conclusions

The geometric and electronic properties of the (110) rutile surface of $Sn_{1-x}Ti_xO_2$ solid solutions have been investigated as a function of Ti content (from 0 to 100 at%) and kind of Ti atom distribution. The large (720 atoms) supercell, utilized here, allows the simulation of low (down to 1.7 at%) Ti contents. The computations have been validated for the pure SnO_2 and TiO_2 systems showing good agreement with previous results obtained by plane waves calculations. Three different types of Ti atom distributions in the SnO_2 lattice have been investigated: homogeneous in the bulk, homogeneous in the surface and segregated in the surface. Bulk Ti distribution hardly has any effect on the geometrical parameters of the surface at any Ti content. In contrast, homogeneous Ti distribution in the surface layer leads to the strongest restructuring of the surface both in terms of bond length and z-shift. Once a full monolayer (100%) of surface Ti atoms is substituted (20% total Ti content), the geometrical properties of the surface are determined by the underlying bulk structure. The surface energy of solid solutions with homogeneous bulk Ti distribution is nearly the same (0.99 J/mol) as that of pure SnO_2 for all Ti contents. In contrast, for both homogeneous and segregated Ti distributions in the surface, the surface energy decreases remarkably from 0.99 to 0.75 J/mol with increasing Ti content from 0 to 20%. Exclusive substitution of Ti on 5c and 6c sites indicates that 6c surface sites are preferential Ti locations leading to the lowest surface energies. Furthermore, the monotonous decrease of surface energy with increasing surface Ti content for any type of distribution (homogeneous, segregated and exclusive on 5c or 6c sites) suggests that the surface

energy of $Sn_{1-x}Ti_xO_2$ solid solutions is proportional to the Ti surface content. This can be attributed to the lower energy required to break Ti-O bonds than Sn-O ones and the facilitated breaking of Sn-O bonds in the vicinity of Ti atoms. As a result, it is suggested that in $Sn_{1-x}Ti_xO_2$ solid solutions, enrichment of the (110) surface with Ti atoms is the most probable configuration. These results can help the design of complex nanocomposites by providing a general understanding of their surface composition and properties. This is particularly interesting since the experimental determination of the composition of single atomic surface layers of nanoparticles is still a very challenging task.

7

H_2O Adsorption on $Sn_{1-x}Ti_xO_2$

7.1 Introduction

The semiconducting nature of many metal oxides makes them interesting materials for numerous industrial and economical important applications. Since the pioneering work of Fujishima and Honda [10] in 1972 on photoinduced decomposition of H_2O on TiO_2, intensive research has been done to optimize the photocatalytic behavior of TiO_2 for hydrogen production from H_2O or hydrocarbons and for degradation of organic pollutants [20, 21]. The main advantages of TiO_2-based materials in this area are their high stability, low cost and high photoactivity [18, 209].

Considerable improvement of TiO_2 photocatalysts has been achieved by substitutional or interstitial doping with anionic species, in particular nitrogen [11, 22]. Doping with cationic metal atoms such as Pt [210] and Sn [176, 211] has also been shown to improve the photocatalytic behavior. The performance of TiO_2-based photocatalysts used in gas-solid phase reactions varies significantly with the relative humidity [212–214]. At low H_2O content, degradation of pollutants is enhanced by an increased number of hydroxyl groups on the surface [212]. However, at higher water content the H_2O species are competing with the actual reactants [212, 213], reducing the reaction rates as it has been shown for trichloroethylene [213] and m-xylene [215]. Furthermore, H_2O species adsorbed on the TiO_2 surface decrease the upward band bending. This facilitates the recombination of electron and holes and reduces the photocatalytic activity [18, 214]. Thus it is an important task to control the water adsorption properties on TiO_2-based catalysts in order to optimize their photocatalytic activity.

Another interesting field for semiconducting metal oxides is their use as chemoresistive gas sensors [8]. Their ability to change conductivity when gaseous molecules

are reacting with the surface makes them particularly applicable for such devices [216, 217]. Solid state gas sensors made of metal oxide nanoparticles are currently utilized for process safety control, environmental monitoring and homeland security [218, 219]. They have been applied to human breath analysis to estimate the blood alcohol content of drunk drivers [220] and more recently for the detection and monitoring of breath markers for several diseases such as lung cancer [221] or diabetes [222]. Tin oxide (SnO_2) is the most widely used metal oxide for chemoresistive gas sensors [7].

Its sensitivity and selectivity depend also on the exposed facets of the rutile crystal structure [223]. Han et al. [224] synthesized SnO_2 particles with different morphologies and found that octahedral particles with exposed high-energy (221) facets show highest gas-sensing performance towards ethanol. However, the gas sensing performances reported in this article are rather poor compared to those found in other studies with exposed low-index SnO_2 facets such as (110), (101) and (100) [225]. Furthermore, such high-index (221) facets have a higher surface energy [224] and thus are more difficult to produce than spontaneously growing low-index facets [226]. High sensitivity and selectivity is in particular important for chemoresistive gas sensors used in non-invasive medical diagnostics (breath analysis) since the breath consists of more than 1000 volatile compounds and has a high relative humidity (r.h.) [227]. This is particularly problematic as water vapor increases the electrical conductivity of the metal oxide upon reaction with its surface and thus results in an unreliable sensor response [14, 228].

High cross-sensitivity to humidity is a major drawback of SnO_2, one of the most studied and widely used gas sensing metal oxides, sensitive to several relevant analytes such as CO, NO_x, H_2 and ethanol [7]. In fact, the reaction between water vapor and the SnO_2 surface leads to remarkable changes (up to 85%) in its sensor response [14, 228]. Even for more selective sensing oxides such as WO_3, water vapor is a common problem [229] that limits its applicability to non-invasive medical diagnostics by breath analysis.

The understanding of the cross-sensitivity mechanism of gas sensing metal oxides to humidity is still in progress. As a result, there is a necessity for further research on the H_2O adsorption on wide band gap semiconducting metal oxides that overlaps with the interest to optimize such materials for photocatalysis. For adsorption of H_2O on SnO_2 and the resulting increase in electrical conductivity, three main paths have been proposed [228]. In the first mechanism, it is suggested that H_2O dissociates in an H atom and OH group that react further with the metal oxide surface. The OH group (terminal OH) binds to a surface metal atom, whereas the H atom binds to a rooted O atom resulting in a rooted OH group. The latter is then donating an electron to the conduction band [230]

according to eq. (7.1).

$$H_2O_{gas} + Sn^* + O^* \longrightarrow \left(Sn^{\delta+} - OH^{\delta-}\right) + \left(OH^+\right) + e^- \tag{7.1}$$

The asterisk indicates the active sites of the metal oxide surface. $\left(OH^+\right)$ refers to a rooted OH group and $\left(Sn^{\delta+} - OH^{\delta-}\right)$ to an isolated (terminal) hydroxyl group. Since the rooted O is normally in the (2-) state it can become ionized and function as an electron donor.

The second mechanism considers the formation of oxygen vacancies. In this mechanism, the rooted OH group reacts further and binds to a neighboring Sn atom producing an oxygen vacancy. This vacancy donates by ionization two electrons to the conduction band of the semiconductor [230]. The third mechanism is described as an indirect process where pre-adsorbed species are changing the electron affinity of the surface [231, 232]. This could be for instance the reaction of the adsorbed hydroxyl group or the hydrogen atom bond to rooted O which are acting as active sites on the surface and possibly react with acid or basic groups [231, 232].

Recently, it has been shown that altering the SnO_2 structure by introduction of impurities results in a drastic stabilization of the sensor response in the presence of varying water vapor content [17]. Doping of SnO_2 nanoparticles with low Ti content (4.6 at%) decreased the cross-sensitivity to r.h. remarkably while maintaining high sensitivity towards the tested analyte (ethanol). At the optimal doping content, a residual cross-sensitivity to r.h. of ca. 15% was measurable increasing the r.h. from 0 (dry air) to 20%. Further increase of r.h. did not have any effect on the sensor signal. This approach is particularly convenient as both metal oxides (SnO_2 and TiO_2) share a rutile crystal phase and their co-synthesis at high temperature (>2000K) promotes the formation of a substitutional solid solution without any segregation up to 80 at% of Ti.

The two metal oxides, SnO_2 and TiO_2, have noticeable differences in electronic and adsorption properties due to the fact that Ti is a transition metal and Sn is a group IV element. In terms of sensitivity and conductivity, TiO_2 is inferior to SnO_2 [8]. Nevertheless, it has a higher thermodynamic stability and less cross-sensitivity to humidity than SnO_2 [7]. Experimentally studied $Sn_{1-x}Ti_xO_2$ nanoparticles [17] combined the advantages of both metal oxides but a fundamental understanding of the H_2O interaction with their surface is still missing. In this regard, theoretical investigation of the $Sn_{1-x}Ti_xO_2$ system represents a unique opportunity to achieve a better understanding of the mechanisms controlling the adsorption properties of H_2O on wide band gap semiconducting metal oxides for application in gas sensing and photocatalysis. Among computational methods, DFT is a quantum mechanical method that is widely used to describe catalytic processes mainly on crystal metal surfaces [233–235]. Furthermore, it

has been proven to be an appropriate method for the calculation of metal oxide surfaces [180, 181, 236–238]. In fact, DFT has been applied to evaluate the stability of stoichiometric pure SnO_2 and TiO_2 surfaces showing that for both crystals the (110) surface is the most favored. Moreover, the $Sn_{1-x}Ti_xO_2$ bulk system has been studied by DFT [177] confirming the experimentally measured variation from Vegards law for the rutile lattice parameters [17, 199].

Adsorption properties of H_2O on the pure SnO_2 and TiO_2(110) surfaces have been studied extensively by DFT. It has been shown that H_2O tends to dissociate spontaneously on the SnO_2(110) surface at high coverages, indicating that dissociative adsorption is favored over associative one [182, 200]. In contrast, on TiO_2, associative adsorption is favored over dissociative adsorption at full coverage [239] while dissociative adsorption becomes favorable at low coverage [240].

In this chaper, DFT calculations have been used to investigate the H_2O adsorption properties on $Sn_{1-x}Ti_xO_2$ solid solutions. First, the binding energies and geometrical properties for dissociative and associative H_2O adsorption have been computed on the pure SnO_2 and TiO_2 surfaces at high and low H_2O coverage to verify the consistence with previous studies. The dissociative adsorption energy has then been evaluated for $Sn_{1-x}Ti_xO_2$ solid solutions as a function of the Ti content providing an explanation for the minimal cross-sensitivity to humidity observed for gas sensors made of such solid solutions.

7.2 Methods

For the DFT calculations of this chapter, the same pseudopotentials and basis sets as in the previous chapter (chapter 6) have been adopted, namely a double-ζ plus polarization (DZVP) basis set for metal atoms and a triple-ζ plus polarization (TZVP) for oxygen and hydrogen. All basis sets have been optimized according to the Mol-Opt method [62]. In the valence shell of Sn, Ti and O, four, twelve and six electrons, respectively, have been considered explicitly. For auxiliary PW expansion of the charge density, the energy cutoff has been set at 400 Ry.

The optimal compromise between physical accuracy and resource allocation for the present investigation has been found to be a supercell of 720 atoms. The rutile primitive cell has been repeated three and four times along the x- and y-directions, respectively. Along the z-direction, the cell has been repeated ten times, in order to form a slab of ten metal atom layers. All simulations have been performed with periodic boundary conditions. Lattice parameters a, c and u have been optimized according to chapter 6. Optimized parameters are listed in Table 6.1. The simulations with surface Ti distribution have been performed using the parameters optimized for bulk calculations.

To simulate the surface, 20 Å of vacuum have been added along the z-direction

in order to avoid any interaction of the slab with its periodic image. Three metal atom layers on the top and the bottom of the slab have been allowed to relax in all dimensions while four layers have been fixed in the middle to simulate the bulk corresponding to the simulation domain used previously in chapter 6 investigating the stability of $SnO_{1-x}Ti_xO_2(110)$ surfaces.

The adsorption of H_2O is simulated on one of the exposed surfaces of the slab. It is supposed that placing adsorbates on both sides gives more accurate results since possible dipole moments are eliminated [241]. However, here, calculations with adsorbates on both sides show less than 3.5 kJ/mol difference in binding energy. Thus, it is assumed that precise values of the binding energy are yielded also when simulating adsorption only on one surface. The H_2O binding energies (E_B) are calculated according to eq. (7.2), where E_{slab} and $E_{H_2O,g}$ denote the total energy of the clean SnO_2 slab and the H_2O molecule in gas phase, respectively. $E_{slab+nH_2O}$ is the energy of the surface slab plus n adsorbates. Note that with this expression, in contrast to chapter 5 a positive value of E_B indicates an exothermic adsorption.

$$E_B = \frac{(E_{slab} + nE_{H_2O,g}) - E_{slab+nH_2O}}{n} \tag{7.2}$$

The energy of an isolated H_2O molecule ($E_{H_2O,g}$) has been calculated in a periodically repeated cell of 20 Å. Here, the surface plane consists of twelve unit cells meaning that full H_2O coverage (1 ML) corresponds to twelve adsorbed H_2O groups.

Surface metal atoms (Figure 7.1) bound to five or six neighboring O atoms are named as Me_{5c} or Me_{6c}, respectively. Rooted O atoms that are located in the surface layer are denoted as O_r, whereas bridging O atoms are denoted as O_{br}. The O atoms where H_2O is adsorbed associatively is denoted as O_{H_2O}.

7.3 H_2O Adsorption on SnO_2

7.3.1 Adsorption of Isolated H_2O (1/12 ML)

Associative adsorption of an isolated H_2O molecule (1/12 ML) is found to be stable in a perpendicular configuration (Figure 7.2 a,b). The distance between Sn_{5c} and O_{H_2O} is 2.28 Å. Additionally to the perpendicular configuration, the H_2O molecule has been initially placed parallel to the surface (not shown). In this case, however, the H_2O molecule dissociates spontaneously. In the dissociated configuration, the Sn_{5c}-OH_{term} (Figure 7.1 a) bond length is remarkably smaller (2.02 Å) indicating a stronger bond. This Sn_{5c}-OH_{term} bond length is equal to

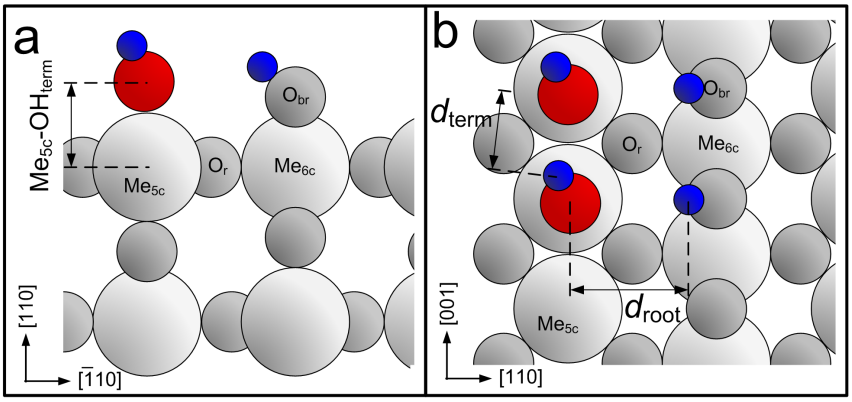

Figure 7.1: (a) Cross-sectional and (b) top schematic illustration of geometrical properties of dissociative H_2O adsorption on rutile (110). Large spheres indicate metal atoms (Sn or Ti), small gray ones O atoms of the (110) surface, red spheres O atoms of the adsorbing H_2O molecule and blue ones its H atoms.

that between Sn_{6c} and O_{br} of the clean SnO_2(110) slab (chapter 6 [34]) suggesting similar characteristics to the Sn-O bonds.

The distance between H atoms of an associatively adsorbed H_2O molecule and O_{br} is 2.86 Å (Figure 7.2 a). For dissociative adsorption, smaller intermolecular distances are found: The H atom of the OH_{root} group and the O atom of the OH_{term} has a distance (d_{root}) of 2.36 Å (Figure 7.2 d). This indicates the presence of additional attractive interactions for dissociative adsorption. Furthermore, it has been observed that the H atom of the OH_{term} group points towards the nearest O_{br} atom (opposite of the OH_{root} group, 3.11 Å, Figure 7.2 d). Thus, approaching of the two OH groups, as it has been observed at higher coverages (1.94 Å [180]), is prevented.

The binding energy of associatively adsorbed H_2O is 98.8 kJ/mol, whereas for dissociative adsorption it is significantly higher (135.2 kJ/mol). Based on these results, it is concluded that, at low coverage, H_2O tends to dissociate on the SnO_2(110) surface. The stabilization of dissociated H_2O can be explained by attractive interactions between the OH groups and a stronger bond between Sn_{5c} and the O of the OH_{term} group.

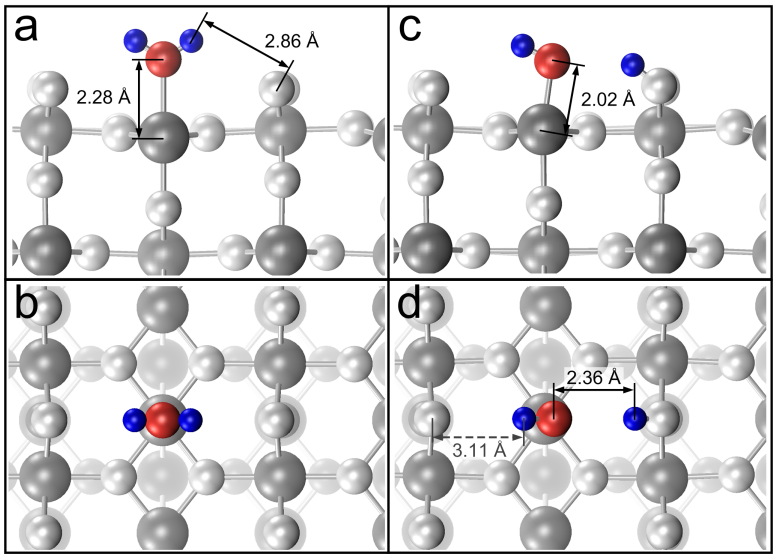

Figure 7.2: (a,c) Cross-sectional and (b,d) top view of stable configurations of isolated H_2O adsorbed (a,b) associatively and (c,d) dissociatively on SnO_2(110). The Sn-O bond length is remarkably smaller for dissociative adsorption (2.20 Å) than for associative one (2.28 Å) indicating stronger bonds.

7.3.2 Adsorption at High Coverage (1 ML)

Structural Properties For associatively adsorbed H_2O, the initial configuration has been perpendicular to the surface comparable to the isolated H_2O configuration (1/12 ML). However, at this high coverage, the H_2O molecules bend towards the surface resulting in a parallel associative adsorption configuration (Figure 7.3 a). This is in contrast to what has been observed (see discussion above) for isolated H_2O molecules which spontaneously dissociate when initially positioned in a parallel configuration. As a result, at high coverage, the distance between an H atom and an O_{br} atom is reduced to 1.42-1.88 Å (Figure 7.3 a). It is suggested that these H-bonds are stabilizing the H_2O on the surface at high coverage. The intermolecular distance between two H_2O molecules is 2.49 Å (Figure 7.3 a) indicating additional attractive interactions that are not present for isolated H_2O. The latter presumably affects the electron density around the H pointing to the O_{br} atom hindering the dissociation of an H atom as it has been observed for isolated H_2O. The distance between the O_{H_2O} atom and the Sn_{5c} atom (Sn_{5c}-O_{H_2O}) is larger for 1 ML associative adsorption (2.39 Å) than at low coverage (2.28 Å) indicating weaker bonds.

For dissociative adsorption, d_{root} (Figure 7.1 b) is remarkably smaller at high coverage (1.80 Å, Figure 7.4 a) than at low coverage (2.36 Å) indicating enhanced

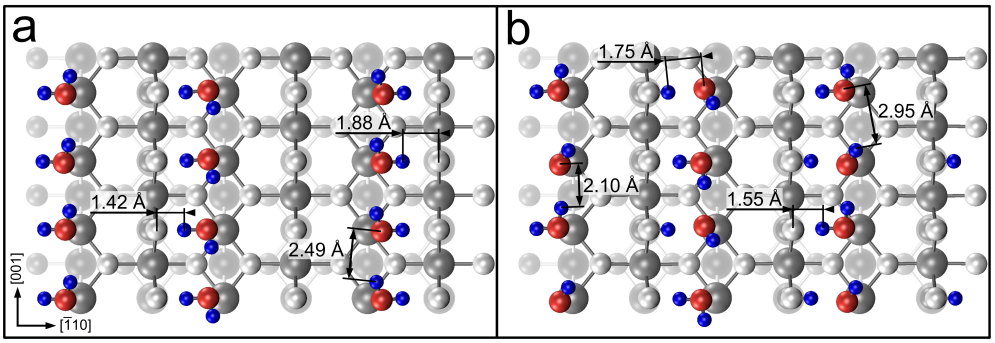

Figure 7.3: (a) Top view of a stable configuration of associatively adsorbed H_2O at 1 ML coverage on SnO_2(110). When all molecules point into the same direction, H_2O spontaneously dissociates resulting in a mixed associative/dissociative adsorption state (b) .Sn: dark gray, O_{surf}: light gray, O_{H_2O}: red, H:blue.

H-bonds. At high coverage, the H atom of OH_{term} groups is attracted by the O atom of a neighboring OH_{term} group. In contrast, at low coverage, the H atom of the OH_{term} group is attracted by an adjacent O_{br} (3.11 Å, Figure 7.2 d) atom leading to a larger d_{root}. Moreover, the neighboring OH_{term} groups show additional attractive interactions between the H and O atom of two adjacent groups that is not possible for isolated H_2O adsorption. The distance between these H and O atoms (d_{term}) is 2.49 Å. The bond length between Sn_{5c} atoms and an OH_{term} group (Sn_{5c}-OH_{term}, Figure 7.1 b) is similar at both high (2.06 Å) and low (2.02 Å) coverage indicating same bond characteristics for both coverages. These values are close to the bond length between Sn_{6c} and O_{br} (2.02 Å) of the clean SnO_2(110) surface [34].

Additional to pure associative and dissociative configurations, a stable state is found in a mixed configuration where half of the molecules dissociate and the other half adsorbs associatively (Figure 7.3 b). This configuration resembles the one found for partial H_2O dissociation on Ru(0001) where a hexagonal pattern was formed [242]. On SnO_2, the Sn_{5c}-O_{H_2O} bond length is with 2.25 Å similar to that (2.28 Å) for isolated H_2O adsorption suggesting similar bond characteristics. The bond length between Sn_{5c} and the dissociated OH_{term} groups (2.09 Å) is close to that for pure dissociative adsorption at high (2.06 Å) and low (2.02 Å) H_2O coverage. The complete geometrical properties are reported in Figure 7.3 b.

Stability Pure associative adsorption of H_2O at 1 ML has a binding energy of 112 kJ/mol (Figure 7.3 a, Table 7.1). The same binding energy (113 kJ/mol) has been computed in a previous study using a smaller unit cell with the PBE exchange correlation functional [182]. However, in the latter, artificial constraints

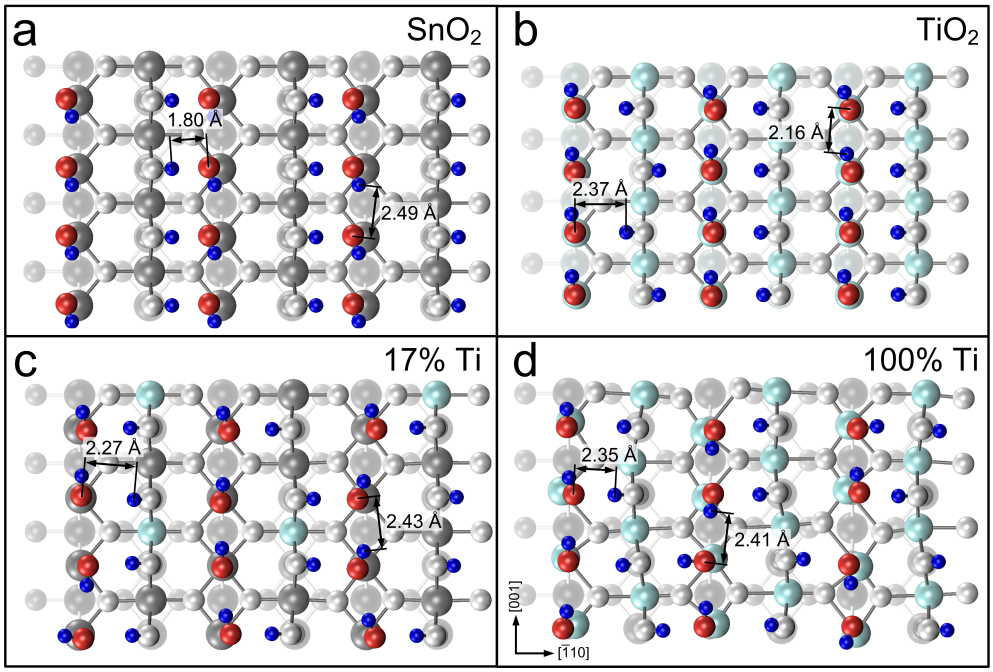

Figure 7.4: Top view of stable configurations of dissociative H_2O adsorption on (a) SnO_2, (b) TiO_2 and $Sn_{1-x}Ti_xO_2$ with surface Ti content of (c) 16.7% and (d) 100% at 1 ML coverage. The inhomogeneity of Ti-doped SnO_2 surfaces (c,d) leads to an asymmetric configuration of dissociatively adsorbed H_2O. Despite their smaller lattice parameters, d_{root} is larger on Ti-doped SnO_2 and on pure TiO_2 than on pure SnO_2.

have been introduced for the relaxation to prevent spontaneous dissociation of the H_2O molecules. Figure 7.3 a shows that the H_2O molecules bound to the left and the middle column of Sn_{5c} atoms point towards the O_{br} atom on their left side, whereas the H_2O molecules of the last column point towards the O_{br} atom on their right side resulting in an asymmetric configuration.

Previous DFT studies applying the planewaves approach showed that molecular H_2O on rutile (110) SnO_2 is neither stable for a complete nor half a monolayer coverage of H_2O [180, 182, 200, 243]. There, water molecules placed initially above a fivefold coordinated Sn atom dissociated spontaneously into OH and H. However, the unit cells used in those studies had a surface about three times smaller than that used here. The use of smaller cells restricts the possible configurations of adsorbates and their periodic repetition leads to more symmetric arrangements of adsorbed species. To understand the destabilizing effect of higher orientation symmetry (all H_2O molecules pointing into the same direction), the

Table 7.1: Dissociative and associative H_2O binding energies at 1 ML and 1/12 ML coverage on SnO_2. All values are given in $\frac{kJ}{mol}$.

coverage	dissociative	associative	mixed	
1/12 ML	135.2	98.8	-	
1 ML	145.2	112.0	137.8	
	141	113[a]	143	[182]

[a] use of artificial constraints to obtain only associative H_2O adsorption

water molecules of the third column (Figure 7.3 a) have been artificially placed so that all of them point into the same direction. This leads to dissociation of half the H_2O molecules (Figure 7.3 b) resulting in a mixed associative and dissociative adsorption state with a binding energy of 137.8 kJ/mol (Table 7.1). An associative configuration is found in previous studies using a smaller unit cell [182, 200] but required the utilization of the hybrid functional B3LYP [180]. This was attributed to the larger H-bond length in hybrid DFT calculations such as B3LYP (than in plain ones) that inhibited the formation of covalent bonds and thus H_2O dissociation [180]. However, the results presented here demonstrate that spontaneous dissociation of H_2O on $SnO_2(110)$ is not only affected by the functional used but also by constraints resulting from the use of a small unit cell with periodic boundary conditions which lead to unreasonably high-symmetry configurations [180, 182]. Here, for the first time, a stable state for associative adsorption configuration has been established in a more asymmetric configuration using a standard exchange correlation potential (PBE). Such associative adsorption is consistent with experiments showing the presence of H_2O molecules on the $SnO_2(110)$ surface [244]. This suggests that restrictions of the system size have to be considered as potential sources of errors in DFT calculations.

A binding energy of 145.2 kJ/mol has been obtained for pure dissociative adsorption of H_2O at 1 ML. Again, this is in very good agreement with previous results [182] reporting a value of 141 kJ/mol. It is significantly more stable than associative adsorption (112 kJ/mol) (Table 7.1), similar to what has been observed for isolated H_2O adsorption. For all coverages simulated in this study, on SnO_2, E_B of dissociative H_2O (135.2-145.2 kJ/mol) adsorption is higher than that of associative H_2O adsorption (98.8-112.0 kJ/mol) demonstrating that H_2O molecules preferably adsorb dissociatively on $SnO_2(110)$ independent of the coverage.

The analysis of the geometry suggests the presence of intermolecular H-bonds at high H_2O coverage for both associative and dissociative adsorption. These H-bonds stabilize the adsorbates resulting in higher binding energies at high co-

verage. In contrast, H-bonding was previously considered to play only a marginal role for H_2O adsorption on SnO_2 [239]. Furthermore, the higher binding energies at high coverage indicate that, on SnO_2, adsorption of H_2O is enhanced with increasing water content. For the use of SnO_2 as a gas sensor, this means that the higher the relative humidity the more H_2O is adsorbed. Consequently, the conductivity and response of SnO_2 gas sensors depend on the relative humidity also at relatively high humidity concentration.

7.4 H_2O Adsorption on TiO_2

7.4.1 Adsorption of Isolated H_2O (1/12 ML)

On TiO_2, in contrast to SnO_2, associatively adsorbed H_2O is stable both in configurations perpendicular (cf. Figure 7.2 a,b) and parallel (Figure 7.5 a,b) to the surface. The bond length between Ti_{5c} and O_{H_2O} is similar for both configurations (2.25 Å and 2.26 Å) and close to that on SnO_2 (2.28 Å). Despite the smaller lattice parameters of TiO_2 (a=4.64 Å and c=2.98 Å) [34], the perpendicular H-O_{br} distance (2.87 Å) is similar to that on SnO_2 (2.86 Å). This suggests that the H-O interaction is hardly affected by the dimension of the lattice or by the metal atom type (Sn or Ti).

For dissociatively adsorbed H_2O, the Ti_{5c}-OH_{term} distance (1.82 Å, Figure 7.5 c) is remarkably smaller than for associative adsorption and, as observed for SnO_2, close to the Ti_{6c}-O_{br} distance of the clean TiO_2(110) surface (1.83 Å) [34]. For dissociation of the H_2O molecule, d_{root} (Figure 7.5 c) of 2.30 Å is found. The perpendicular configuration (92.0 kJ/mol) of an H_2O molecule is slightly more stable than the parallel one (89.5 kJ/mol, Table 7.2). Dissociation is, similar to SnO_2, favored over both types of associative configurations with a binding energy of 99.4 kJ/mol (Table 7.2).

7.4.2 Adsorption at High Coverage (1 ML)

Structural Properties At 1 ML associatively adsorbed H_2O, the distance between the H atom and O_{br} is with 2.11 Å (Figure 7.6 a) remarkably larger than that on SnO_2 (1.42-1.88 Å, Figure 7.3 a) regardless of the smaller lattice parameters of TiO_2. This suggests, that H-bonds between adsorbates and surface are less pronounced on TiO_2. The Ti_{5c}-O_{H_2O} distance is larger at high coverage (2.40 Å) than for both perpendicular (2.25 Å) and parallel (2.25 Å, Figure 7.5 a) configuration at low coverage as observed for SnO_2. This indicates that at high coverage, the Ti-O bond is weaker. The distance between H and O_{H_2O} is smaller

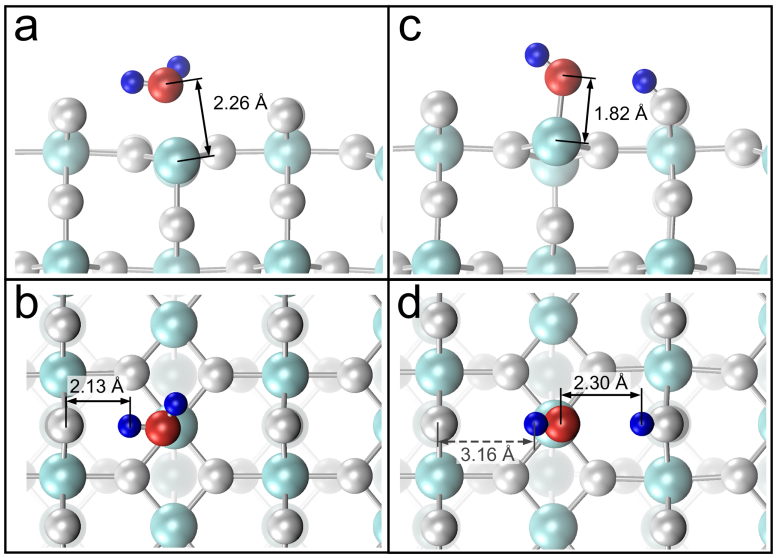

Figure 7.5: (a,c) Cross-sectional and (b,d) top view of stable configurations of isolated H_2O adsorbed associatively (a,b) and dissociatively (c,d) on TiO_2(110). A more stable state is found for associative adsorption in a perpendicular configuration similar to the one on SnO_2 (Figure 7.2 a,b). On TiO_2, the difference between the Ti-O bond length for associative and dissociative adsorption is even larger than on SnO_2, but less visible in the change of binding energy (Table 7.2).

(2.15 Å, Figure 7.6) on TiO_2 than on SnO_2 (2.49 Å, Figure 7.3 a) in agreement with the smaller lattice parameters of TiO_2.

For dissociative adsorption, d_{root} at high coverage (2.37 Å, Figure 7.4 d) is larger than for isolated adsorption (2.30 Å, Figure 7.5 d), indicating repulsive intermolecular interactions. Thus, on TiO_2, no stabilization but rather slight destabilization is established at high coverage for dissociative H_2O adsorption. In agreement with the different lattice parameters, d_{term} is smaller on TiO_2 (2.16 Å, Figure 7.4 b) than on SnO_2 (2.49 Å, Figure 7.4 a). The Ti_{5c}-OH_{term} distance at high coverage (1.87 Å, Table 7.4) is similar to that (1.82 Å) for isolated adsorption and close to the Ti_{6c}-O_{br} distance of the clean TiO_2(110) surface (1.83 Å) [34].

Stability At 1 ML, associative H_2O adsorption on TiO_2 (Figure 7.6) results in a binding energy of 78.7 kJ/mol (Table 7.2). Similar values (83-95.5 kJ/mol) have been reported previously for associative H_2O adsorption on TiO_2 at high coverage [182, 239]. Dissociatively adsorbed H_2O (Figure 7.4 b) is found to be less stable with a binding energy of 60.3 kJ/mol. This is again in reasonable agreement with previous studies (66-87.9 kJ/mol [182, 239, 245]). Partially dissociated

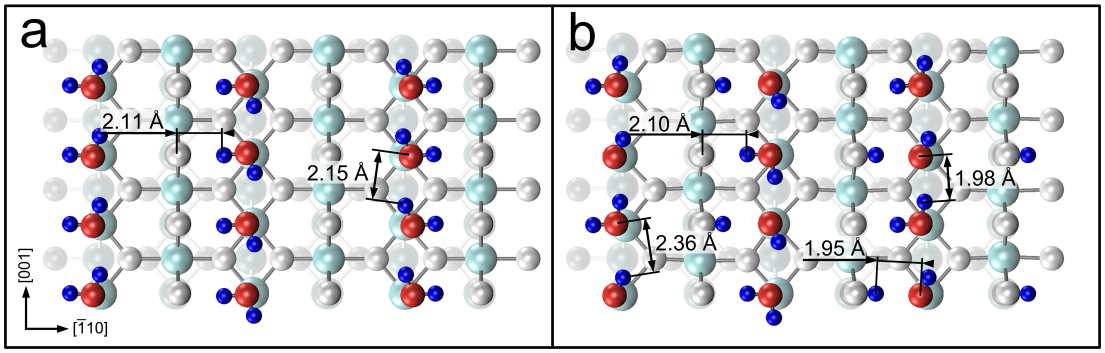

Figure 7.6: (a) Top view of H_2O adsorbed on TiO_2(110) at 1 ML in (a) an associative configuration and (b) in a configuration where both molecular and dissociated species are present. In contrast to SnO_2, H_2O does not dissociate on TiO_2 leading to highly symmetric configurations.

H_2O (75.4 kJ/mol, Figure 7.6) is slightly less stable than pure associative and dissociative adsorption. This is in contrast to SnO_2, where partial dissociation of H_2O (Figure 7.3 b) is found to be favored over pure associative adsorption and is in agreement with the observed stabilization effect of H-bonds.

Table 7.2: Dissociative and associative H_2O binding energies at 1 ML and 1/12 ML coverage on TiO_2. All values are given in $\frac{kJ}{mol}$.

coverage	dissociative	associative	mixed	
1/12 ML	99.4	92.0 (89.5[a])	-	
1 ML	60.3	78.7	75.4	
	66	83	-	[182]

[a] configuration parallel to surface (Figure 7.6)

For both associative and dissociative adsorption, E_B at high coverage (78.7 and 60.3 kJ/mol, respectively) is lower than at low coverage (92.0 and 99.4 kJ/mol, respectively) suggesting the presence of repulsive interactions between adsorbed species. This is in contrast to SnO_2, where H_2O has been found to be more stable at high coverage. There, the stabilizing effect has been attributed to the formation of H-bonds between H and O_{br} (1.42-1.88 Å, Figure 7.3 a) for associative adsorption and between OH_{term} and OH_{root} groups (d_{root}(1 ML)=1.80 Å) for dissociative adsorption. Both distances (2.11 and 2.37 Å, respectively) are larger on TiO_2, indicating a lack of intermolecular attraction. As a result, on TiO_2, the binding energy decreases with increasing H_2O coverage. In other words, on

TiO_2, H_2O adsorption is facilitated at low H_2O content in contrast to SnO_2. This implies that the saturation coverage is dependent on the temperature and can be reached already at a low relative humidity at a certain temperature.

Furthermore, a larger spread between high and low coverage binding energy has been observed compared to SnO_2. On the $TiO_2(110)$ surface, the binding energies show that, for isolated adsorption, H_2O molecules prefer to dissociate whereas associative adsorption is favored at high coverage. Thus, the preferred adsorption mechanism changes with the coverage. There has been discrepancy about the favored adsorption mechanism on $TiO_2(110)$ in the literature previously [238–240, 245, 246]. Some DFT studies [238, 240] using the PW formalism and the revised PBE exchange correlation functional revealed that the dissociative mechanism is favored at low coverages ($\theta \leq$0.5 ML), whereas others [245] using the PW91 functional stated that associative adsorption is favored at a coverage $\theta \leq$1 ML. Experimental studies using TPD, however, determined a tail of the desorption peak extending to higher temperatures (100°C) which was attributed to hydroxyl groups [247]. This confirmed the presence of dissociated H_2O at low coverages. On the other hand, at high H_2O doses (high coverage), molecular species were detected [247, 248] which supports the higher binding energy of associative adsorption at 1 ML found in this study. Furthermore, TPD analysis [247, 248] at lower H_2O doses showed a shift of the H_2O desorption peak to higher temperatures. This indicates a higher desorption energy at lower H_2O coverage which can be attributed to less dipole-dipole repulsion between adsorbed species in agreement with our findings.

7.5 H_2O Adsorption on $SnO_{1-x}Ti_xO_2(110)$

On $Sn_{1-x}Ti_xO_2$ solid solutions dissociative H_2O adsorption has been investigated for isolated species (1/12 ML) and full (1 ML) coverage. It has been shown previously that Ti is preferably distributed in the surface layer of $Sn_{1-x}Ti_xO_2$ solid solutions [34], more specific on six-fold coordinated (6c) surface sites [34, 178]. Therefore, here, H_2O adsorption mechanisms have been investigated on $SnO_{1-x}Ti_xO_2(110)$ surfaces with Ti atoms located exclusively on 6c sites up to a surface Ti content of 50% where all 6c sites are occupied by Ti. At higher surface Ti content, up to 100%, Ti atoms have been distributed additionally on 5c sites. The binding energy shown in Figure 7.8 represents an average value for the different binding sites at a specific surface Ti content.

7.5.1 Adsorption of Isolated H_2O (1/12 ML)

Structural Properties Adsorption of isolated H_2O groups has been investigated on all possible surface sites at each Ti content. Accordingly, Table 7.3 summarizes the results averaged on all possible sites. The Me_{5c}-OH_{term} bond length hardly changes compared to that on pure SnO_2 (2.02 Å) and TiO_2 (1.82 Å). In contrast, the average d_{root} distance increases from 2.36 to 2.50 Å with increasing surface Ti content from 0 to 100% and is always larger than that observed for pure TiO_2 (2.30 Å). The increase of d_{root} indicates reduced interactions and could possibly lead to weaker bond strength. The large scatter at 67% surface Ti content results from a high level of irregular surface restructuring.

Table 7.3: Bond length between Me_{5c} atoms and adsorbed OH_{term} groups (Me_{5c}-OH_{term}, Figure 7.1 b) and distance between OH groups (d_{root}, Figure 7.1 a) for dissociative H_2O adsorption at 1/12 ML coverage. All distances are given in Å. The increase of the standard deviation of d_{root} with the surface Ti content reflects the irregularity of the surface.

	surface Ti content [%]	Sn_{6c}-OH_{term}	Ti_{6c}-OH_{term}	d_{root}
SnO_2	0	2.02	-	2.36±0.002
$Sn_{1-x}Ti_xO_2$	12.5	2.02	-	2.35±0.013
	25	2.02	-	2.42±0.043
	37.5	2.01	-	2.45±0.040
	50	2.01	-	2.45±0.016
	66.7	2.01	1.84	2.64±0.175
	100	-	1.82	2.50±0.402
TiO_2	100	-	1.82	2.30±0.014

Electronic Structure For the representation of isolated H_2O adsorption, only a section of the surface is shown (Figure 7.7) since surface configurations are relevant only in the vicinity of the adsorbate. To describe the adsorption properties, the centers of the Wannier functions have been determined before (Figure 7.7, left side) and after (Figure 7.7, right side) H_2O adsorption. Green spheres in Figure 7.7 visualize the position of the Wannier centers around O_{br} atoms.

On pure SnO_2(110) (Figure 7.7 a), four Wannier centers are close to O_{br}, two of which point towards the adjacent Sn_{6c} atoms (in [001] direction). The other two are oriented out of the surface in [110] direction indicating two free electron pairs.

Upon dissociative H_2O adsorption, one of these free electron pairs is transformed into a bond with the H atom (Figure 7.7 a, right side). When some Sn_{6c} atoms have been substituted with Ti atoms, several O_{br} are bound to both metal atom types (Figure 7.7) resulting in a reorientation of the Wannier centers. In this situation, one center points to the Sn_{6c} atom while two centers point to the Ti_{6c} atom suggesting the formation of an additional bond between O_{br} and Ti_{6c}. In other words, the O_{br} atom forms a total of three bonds to the adjacent metal atoms and has one free electron pair. For the O_{br}-H bond formation, here, one of the O_{br}-Ti_{6c} bonds (Figure 7.7 b, right side) has to be broken. The required energy for this step is reflected in a lower binding energy of H_2O (Figure 7.8) on such surfaces. Regarding the reverse step this means that less energy, e.g. a lower temperature, is needed to remove H_2O from the $Sn_{1-x}Ti_xO_2$ surfaces.

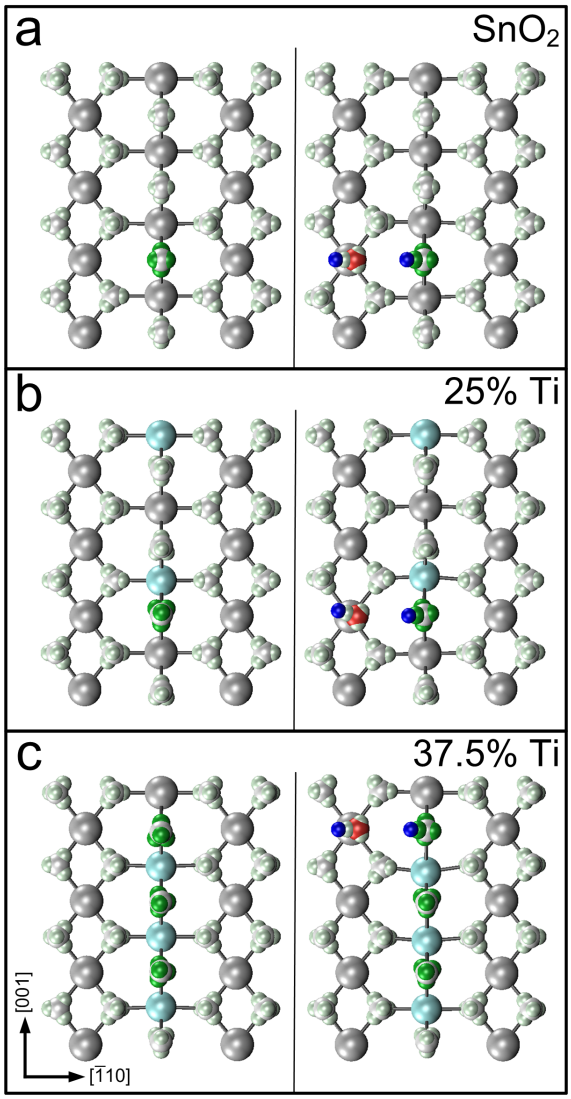

Figure 7.7: Top view of a section of the clean surface (left) of (a) SnO_2 and $Sn_{1-x}Ti_xO_2$ solid solutions with (b) 25% and (c) 37.5% surface Ti content and after adsorption of one H_2O molecule (right side). Small spheres around O atoms indicate the center of Wannier functions. The centers important for H_2O adsorption are highlighted in green.

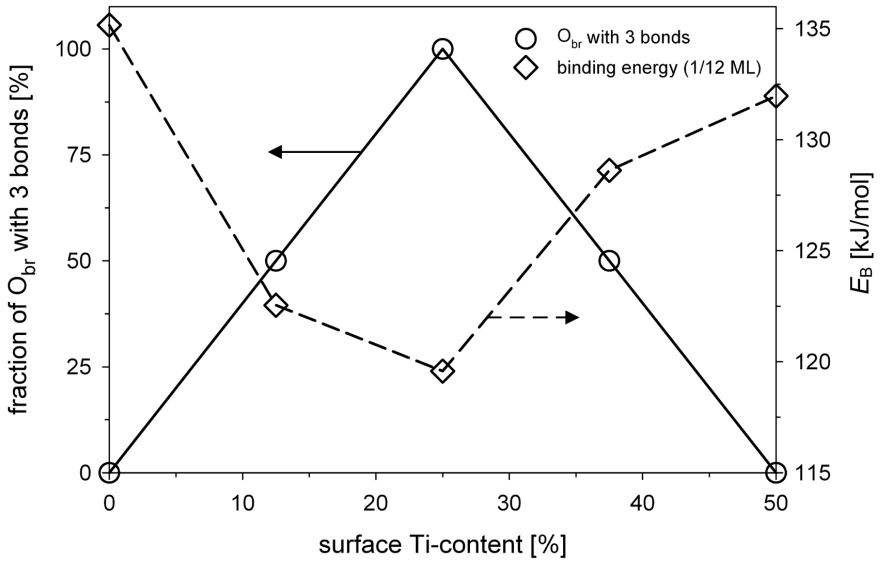

Figure 7.8: Fraction of O_{br} atoms on the (110) surface of $Sn_{1-x}Ti_xO_2$ solid solutions that form three bonds to neighboring Sn_{6c} or Ti_{6c} atoms as a function of the surface Ti content (diamonds). When all 6c sites are occupied by the same type of metal atom (Sn at 0% and Ti at 50%), O_{br} atoms form two bonds to the neighboring Me_{6c} atoms. However, when O_{br} is adjacent to an Sn_{6c} atom on one side and a Ti_{6c} atom on the other one, two bonds are formed to Ti and one to Sn. The number of O_{br} with such three bonds has a maximum at 25% surface Ti content (alternating Sn and Ti atoms on 6c sites). Upon H_2O adsorption, the third Ti_{6c}-O_{br} bond has to be broken resulting in an inverse behavior of the H_2O binding energy (triangles): the binding energy shows a minimum at 25% surface Ti content.

At a surface Ti content >25%, two or more Ti_{6c} atoms can be adjacent to each other (Figure 7.7 c). In these cases, the neighboring Ti_{6c} equally polarize the electrons (Wannier centers) of the enclosed O_{br} atom resulting in a single O_{br}-Ti_{6c} bond each (Figure 7.7 c) and a total of two bonds of the O_{br} atom. A correlation is found between the H_2O binding energy and the bonds formed by O_{br}. For this, the fraction of O_{br} atoms forming a total of three bonds to adjacent Me_{6c} atoms has been analyzed as a function of the surface Ti content (Figure 7.8, circles). It is maximal at 25% surface Ti content. The converse behavior has been observed for the average binding energy. The average binding energy of all possible adsorption sites on the surface decreases (Figure 7.8, diamonds) since the number of O_{br} with three bonds increases with the surface Ti content up to 25% (Figure 7.8, circles). However, further increase of the surface Ti content reduces the number of O_{br} with three bonds and thus the average binding energy increases.

At surface Ti contents between 25 and 50% (Figure 7.7 c) an additional effect has been observed leading to an increase of the binding energy. When the H atom is bound to an O_{br} site between Sn_{6c} and Ti_{6c}, i. e. with three bonds, one Ti-O_{br} bond is broken. However, this change in the electronic structure leads to a shift of all connected Ti_{6c} atoms in [001] direction closer to the O_{br} atoms (Figure 7.7 c, right side). This induces the formation of additional Ti_{6c}-O_{br} which is reflected in an increased binding energy (by ca. 10 kJ/mol) on such sites. At higher surface Ti contents (50-100%) the surface reconstruction and formation of additional Ti_{6c}-O_{br} and Ti_{5c}-O_r bonds on the surface increase. Here, the H_2O adsorption leads to enhanced rearrangements of the geometrical and electronic structure depending on the local environment of the active site. Decrease of the symmetry of the surface with increasing surface Ti content is reflected in an increased range of binding energies for different surface sites (Figure 7.9). This made it difficult to draw a general conclusion for surface Ti contents >50%. However, it is assumed that, in the case of low coverage, H_2O species adsorb on the energetically most favorable site. Thus, the highest binding energy for each Ti content is relevant for the determination of the adsorption characteristics. As a result, a global minimum of the H_2O binding energy for isolated adsorption (1/12 ML) is found at a surface Ti content of 25% suggesting that, at this Ti content, the temperature required for desorption of small amounts of H_2O species from the surface is lowest.

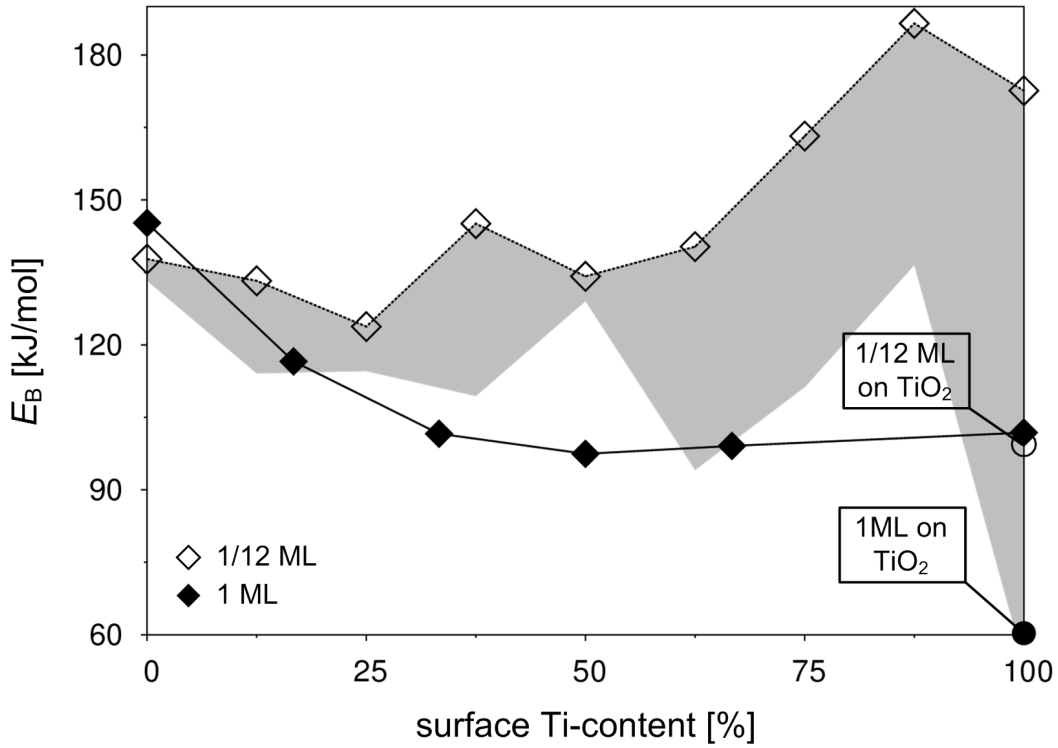

Figure 7.9: Maximum E_B of dissociative H_2O adsorption on $Sn_{1-x}Ti_xO_2(110)$ surfaces at 1/12 ML (open diamonds) and average binding energy at 1 ML (filled diamonds) coverage as a function of the surface Ti content. The gray area shows the range of E_B that has been calculated on different adsorption sites for each Ti content at 1/12 ML. At 1/12 ML, E_B has a minimum at 25% surface Ti content attributed to the maximum number of O_{br} atoms with three bonds to neighboring Me_{6c} atoms (Figure 7.8). With increasing surface Ti content, E_B increases as well as its distribution at each Ti content. This is caused by a large degree of inhomogeneity of the surface structure. E_B at 1 ML decreases drastically up to a surface Ti content of 50%. Further increase of the Ti content has hardly any effect on E_B.

7.5.2 Adsorption at High Coverage (1 ML)

Structural Properties At high coverage, d_{root} increases drastically from 1.86 to 2.49 Å when increasing the surface Ti content from 0 to 33%. This demonstrates a loss of H-bonds between adjacent OH groups that have been detected on pure SnO_2. Further increase of the Ti content hardly has any effect (2.41±0.1 Å) on d_{root}. It is close to that on pure TiO_2 (2.37 Å) indicating that d_{root} is rather determined by the surface composition than by the lattice parameters. In contrast, only marginal changes have been observed for the d_{term} and the Sn_{5c}-OH and Ti_{6c}-OH bond length. A slight decrease of d_{term} from 2.49 to 2.41 Å (Table 7.4) is found with increasing surface Ti content, consistent with the decreasing lattice parameters [34]. The influence of the lattice parameters is as well reflected in the drop (0.25 Å) of d_{term} between 100% surface Ti content, corresponding to 20% total Ti content (2.41 Å), and pure TiO_2 (2.16 Å). When Ti atoms have been introduced in the surface layer (17-67%), Sn_{5c}-OH_{term} decreases from 2.06 Å for pure SnO_2 to 2.03 Å (Table 7.4). The Ti_{5c}-OH bond length, on the other hand, is equivalent to that on pure TiO_2 (1.87 Å) indicating that the characteristic of this bond is determined by the chemical nature of the Me_{5c} atom rather than the surrounding atoms.

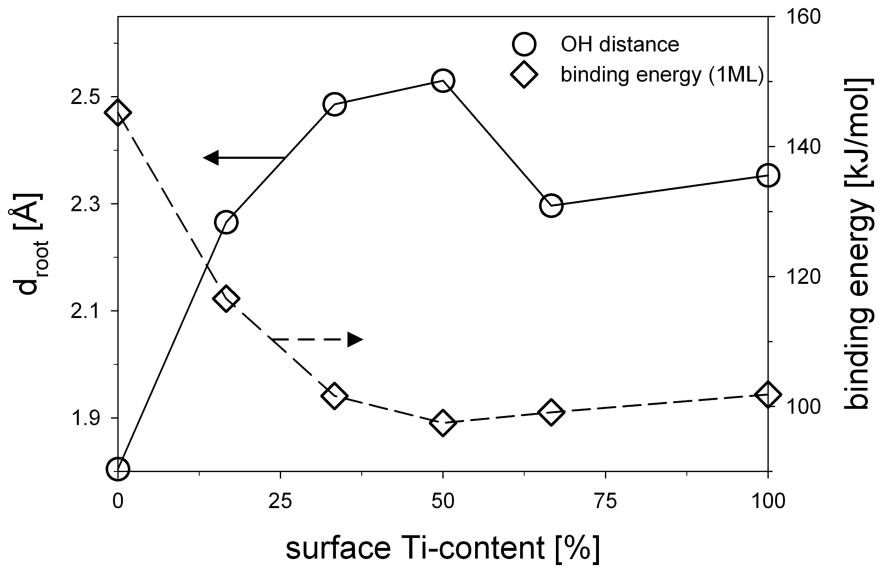

Figure 7.10: Binding energy (diamonds) and d_{root} (circles) of dissociatively adsorbed H_2O at 1 ML on $Sn_{1-x}Ti_xO_2$(110). The drastic decrease in binding energy with increasing surface Ti content up to 33% is accompanied by a remarkable increase in d_{root}.

Table 7.4: Bond length between Me_{5c} atoms and adsorbed OH_{term} groups (Me_{5c}-OH_{term}, Figure 7.1 b) and distance between adjacent OH groups d_{root} and d_{term} (Figure 7.1 a) upon dissociative H_2O adsorption at 1 ML coverage. All distances are given in Å.

	surface Ti content [%]	Sn_{5c}-OH_{term}	Ti_{6c}-OH_{term}	d_{root}	d_{term}
SnO_2	0	2.06	-	1.80	2.49
$Sn_{1-x}Ti_xO_2$	16.7	2.03	-	2.27	2.44
	33.3	2.02	-	2.49	2.35
	50	2.03	-	2.53	2.38
	66.7	2.03	1.86	2.30	2.40
	100	-	1.88	2.35	2.41
TiO_2	100	-	1.87	2.37	2.16

Stability The binding energy at high coverage (1 ML) decreases rapidly from 145.2 to 101.6 kJ/mol with increasing surface Ti content from 0 to 33%. Further increase of the surface Ti content up to 100% has only marginal effect (±3.4 kJ/mol) (Figure 7.10, diamonds, Figure 7.9, filled diamonds). The behavior of the binding energy correlates well with d_{root} (Figure 7.10, circles): a decrease in the binding energy is related to an increase in the H-O distance. This verifies the stabilization of adsorbed species by intermolecular H-bonds which can be quantified by d_{root}. At 100% surface Ti content, E_B (101.8 kJ/mol) is still significantly higher than that on pure TiO_2 (60.3 kJ/mol). This suggests that the underlying SnO_2 crystal contributes considerably to the adsorption properties.

In summary, a minimum of the adsorption binding energy of isolated dissociatively adsorbed H_2O is found for a surface Ti content of 25%. This minimum is attributed to the formation of additional bonds between O_{br} and neighboring Me_{6c} atoms which have to be broken again upon H_2O adsorption. Furthermore, E_B at the high coverage drops rapidly from 145.2 to 101.6 kJ/mol with increasing surface Ti content from 0 to 33%. Higher surface Ti contents have almost no effect on the high coverage binding energy of H_2O. This leads to an overall minimum of E_B between 25 and 33% surface Ti content. A qualitatively similar minimum has been found experimentally at a total (surface + bulk) Ti content of 4.6% for the cross-sensitivity to humidity of FSP-made $Sn_{1-x}Ti_xO_2$ nanoparticles. However, no explanation could be given yet for this behavior [17]. Assuming that all Ti atoms are distributed on the particle surface and the particles have an average size between 9 and 11 nm, the surface Ti content of such particles is approximately

24 to 29% and thus in good agreement with the computed surface Ti content for the minimum of E_B of H_2O. This suggests that dissociative H_2O adsorption plays a key role in the cross-sensitivity mechanisms to humidity of SnO_2-based gas sensors. Furthermore, it supports the proposed homolytic dissociation of water on SnO_2 that leads to an increase in its conductivity [14, 228, 230]. It has been shown previously that Sn-doping of TiO_2 catalysts leads to enhanced photoactivity [176] which was partly attributed to the decrease of the band gap [176, 249]. The results of the present study suggest additionally that the dependency of the catalytic activity on the relative humidity can be minimized for an optimal Sn:Ti ratio.

Moreover, the rapid decrease of the 1 ML binding energy causes adsorbed H_2O to be more stable at low coverage (Figure 7.9, open diamonds) than at high coverage (Figure 7.9, filled diamonds). Already at a surface Ti content of 33%, repulsive interactions between adsorbed species are more pronounced than attractive ones (H-bonds). The amount of adsorbed H_2O is not only dependent on the relative humidity but also on the process conditions such as temperature. This gives a possible explanation for the remaining minimal cross-sensitivity (15%) of FSP-made $Sn_{1-x}Ti_xO_2$ nanoparticles that has been shown experimentally [17]. In fact, there, the working temperature of the gas sensor (320 °C) was most probably high enough to overcome the binding energy at full coverage. However, due to the increased binding energy at low coverages, trace amounts of H_2O remained on the surface leading to a variation of the sensor signal measured in dry air and thus to a small cross-sensitivity residual.

Furthermore, the difference between H_2O binding energy at high and low coverage become larger with increasing surface Ti content due to the drop of the binding energy at 1 ML and the rise of the one at 1/12 ML for surface Ti contents >25% (Figure 7.9). Assuming a linear dependency of the binding energy on the coverage, it is suggested that controlling the amount of adsorbed H_2O species by the temperature is facilitated when the difference between low and high coverage binding energy gets larger. Finally it should be stressed that our theoretical study of H_2O adsorption on SnO_2, TiO_2 and $Sn_{1-x}Ti_xO_2$ surfaces and its impact on the cross-sensitivity of gas sensors only holds rigorously for equilibrated systems. However, it may also reflect the tendencies to be expected under dynamic conditions and therefore help in the interpretation of the relation between water adsorption and its impact on the cross-sensitivity.

7.6 Conclusions

The binding energy of dissociatively and associatively adsorbed H_2O has been calculated on pure $SnO_2(110)$ and $TiO_2(110)$ at high coverage (1 ML) and for

isolated species (1/12 ML). On pure SnO_2, a stable configuration is found for 1 ML associatively adsorbed H_2O using plain DFT calculations in agreement with experiments. This has been possible by the simulation of a larger unit which reduces the level of symmetry. In agreement with previous calculations, dissociative adsorption is shown to be the favored mechanism at all coverages. Independent of the adsorption mechanism, the formation of H-bonds has been observed on SnO_2, leading to a higher binding energy at high coverage compared to that at low coverage.

On TiO_2, the favored adsorption mechanism changes with coverage. Isolated H_2O groups tend to dissociate, while at high coverage, associative adsorption is favored. For both adsorption mechanisms, the binding energy at low coverage is higher than at high coverage. These finding are in agreement with TPD experiments which show a shift of H_2O desorption to higher temperatures at low doses.

On $Sn_{1-x}Ti_xO_2(110)$ with homogeneous surface Ti distribution, the binding energies for dissociative adsorption have been determined at high and low coverages. Analysis of the Wannier centers at low coverage suggest the formation of additional bonds between Ti_{6c} and O_{br} atoms. These have to be broken upon H_2O adsorption resulting in a decrease of the binding energy up to a surface Ti content of 25%. At higher Ti contents, less additional Ti_{6c}-O_{br} bond formation has been observed due to the effect of neighboring Ti_{6c} atoms. This, again , causes an increase of the low coverage binding energy at Ti contents >25%.

The binding energy at high coverage on $Sn_{1-x}Ti_xO_2(110)$ decreases rapidly with increasing surface Ti content up to 33%. This is attributed to the loss of H-bonds indicated by a larger distance between neighboring OH groups (d_{root}). Higher surface Ti contents hardly have any effect on the binding energy. Already at 12.5% surface Ti content, H_2O adsorption at low coverage is more stable than at high coverage. In this case it is suggested that the amount of adsorbed H_2O can be controlled by process parameters such as temperature.

Considering both high and low coverage binding energies, a global minimum is found between 25 and 33% surface Ti content. This minimum in binding energy gives a possible explanation to the previously observed minimum in cross-sensitivity to humidity of $Sn_{1-x}Ti_xO_2$ nanoparticle-based gas sensors. Furthermore, it supports the proposed interaction mechanism between SnO_2 and H_2O vapor based on the homolytic dissociation of H_2O on Sn_{5c} and O_{br} atoms.

The results of this study show that already small amounts of Ti on the $SnO_2(110)$ surface significantly change the H_2O adsorption behavior and that first principles calculations can aid in designing mixed metal oxides with specific H_2O adsorption characteristics. Controlling the H_2O adsorption and reaction mechanism on the desired metal oxides can improve the performance of such materials both in the fields of gas sensors as well as photocatalysis.

8

Conclusion and Outlook

In this work, density functional theory calculations have been used to investigate the structural and electronic properties of advanced metal oxide surfaces.

The choice of computational methods has been shown to be crucial for the accurate description of CeO_2 based materials. Different pseudopotentials and basis sets have been evaluated with the CP2K program package within the framework of standard DFT, DFT+U and hybrid DFT (PBE0). Using standard DFT and DFT+U, it has been shown that the quality of the pseudopotential plays an important role. Hybrid PBE0 simulations are less affected by the quality of the pseudopotential. Reasonable results with standard DFT for the stoichiometric CeO_2 system have been obtained using a pseudopotential considering 30 electrons in the valence shell of Ce atoms. In simulations with reduced CeO_2 it has been necessary to extend standard DFT calculations with a Hubbard U potential of 4.5 eV in order to obtain the correct (insulating) band structure of the material.

Investigation of small Ni clusters adsorbed on CeO_2 has shown significant stabilization with increasing size up to ten atoms. Further increase of the particle size has only little effect on the binding energy of Ni clusters on CeO_2. This is similar to the behavior of Ni clusters formed in gas phase. Three-dimensional Ni clusters have been shown to be thermodynamically favorable on CeO_2 over flat structures. Both Ni-Ni bond length and gyration radius are slightly larger in Ni clusters adsorbed on CeO_2 compared to their equivalents in gas phase indicating an opening of the structure and facilitated accessibility. This can possibly lead to enhanced catalytic properties of Ni clusters supported on CeO_2. Upon adsorption of Ni, d-type orbitals of Ni are occupied in the O_{5p}-Ce_{4f} band gap of CeO_2. At a cluster size of 13 atoms, the band gap is completely filled with the d-band of Ni atoms.

Carbon dioxide adsorption has been studied on $CeO_2(111)$ focusing on the effect of coverage on the activation and stability of CO_2. At low coverage, monoden-

tate species have been shown to be most stable. The structural properties (C-O bond length and O-C-O angle) suggest similar activation of the CO_2 molecule on CeO_2 compared to metal Rh, Pd and Pt surfaces. Monodentate species have been found to be stable up to a coverage of 1/3 ML. Further adsorption of CO_2 results in mixed configurations with multilayers of linear CO_2 species adsorbed above the monodentate ones. The results demonstrate CeO_2 to be a suitable catalyst for CO_2 activation, however, limited up to a certain coverage. This suggests that process conditions such as CO_2 partial pressure are important parameters for the successful activation of CO_2 on the CeO_2 surface.

Several distributions of Ti dopants in the rutile SnO_2 crystal have been simulated showing a tendency to Ti surface enrichment. In particular, substitution of six-fold coordinated Sn atoms with Ti results in a notable stabilization of the (110) surface of the $Sn_{1-x}Ti_xO_2$ solid solutions. This can be attributed to the polarization of electrons between Ti_{6c} and O_{br} creating additional (partial) bonds on the surface. Dissociative adsorption of H_2O species, however, is hindered on such surfaces since the newly formed bonds between surface atoms have to be broken again. As a result, a minimum of the low coverage binding energy has been found at a certain surface Ti content (25%). At high coverage, binding energy of dissociatively adsorbed H_2O decreases rapidly with increasing surface Ti content from 0 to 33%. A global minimum of the binding energy at both low and high coverage can thus be assigned to a surface Ti content between 25 and 33% which gives a possible explanation of the minimum of cross-sensitivity of Ti-doped SnO_2 gas sensors found experimentally. These results show that already small amounts of doping content can change the system properties for H_2O adsorption significantly and are a first step towards a rational design of mixed metal oxides with defined properties for technologically important applications.

The results of this study give fundamental insight in the adsorption properties of small molecules on advanced metal oxide based materials essential for many technologically important applications such as photocatalysis, CO_2 conversion to hydrocarbons and gas sensing devices. To improve the value of this study for experimental purposes it is proposed to perform further simulations investigating the reaction mechanism of CO_2 on the Ni-CeO_2 system. This could include utilization of molecular dynamics or nudged elastic band calculations investigating the Sabatier reaction on pure Ni, pure CeO_2 and the Ni-CeO_2 and a comparison of the activity of the different catalysts. Furthermore it is suggested to investigate the substitution of Sn atoms in the rutile SnO_2 crystal and on its (110) surface with other transition metal atoms such as Zr, Fe, Ru, Co, Rh, Ni, Pd and Zn and to screen for their effect on the water adsorption mechanism. This can possibly lead to the development of a new mixed metal oxide with improved properties for photocatalysis or gas detection.

List of Figures

LIST OF FIGURES

List of Tables

List of Abbreviations

5c	five-fold coordinated
6c	six-fold coordinated
ADMM	auxiliary density matrix method
AFM	atomic force microscopy
B3LYP	hybrid exchange correlation functional with three parameters using Becke's functional for exchange and the Lee-Yang-Parr functional for correlation
BFGS	minimization algorithm by Broyden, Fletcher, Goldfarb and Shanno to optimize the geometry
BSSE	basis set superposition error
DFT	density functional theory
DFT+U	extended DFT using a Hubbard U potential
DOS	density of states
DZV	double-ζ valence basis set
DZVP	double-ζ valence plus polarization basis set
FSP	flame spray pyrolysis
GGA	general gradient approximation
GPW	Gaussian and plane waves
HOMO	highest occupied molecular orbital
IR	infra-red
LDA	local density approximation
LEED	low-energy electron diffraction
LUMO	lowest unoccupied molecular orbital
Me	metal atom
MEP	minimum energy path
ML	monolayer
MLWF	maximally localized Wannier functions
MO	metal oxide
Mol-Opt	method to optimize atomic basis sets according to the electronic configuration of a atom in specific molecules
NEB	nudged elastic band
NN	nearest neighbor site
NNN	next nearest neighbor site
PBE	GGA exchange correlation functional according to Perdew, Burke and Ernzerhof [44]
PBE0	hybrid exchange correlation functional according to Perdew and Ernzerhof, com-

	menly using 0.25 of exact exchange; here 0.2 of exact exchange have been used
PDOS	projected density of states
ppb	parts per billion
PW	plane waves
r.h.	relative humidity
RKS	spin-restricted calculations according to the Kohn-Sham theorem
SCF	self-consistent field
SMSI	strong metal-support interaction
TPD	temperature programmed desorption
TWC	three way catalyst
TZV2P	triple-ζ valence plus double polarization basis set
UKS	spin-unrestricted calculations according to the Kohn-Sham theorem
XPS	x-ray photoelectron spectroscopy

References

[1] L. Marsella and V. Fiorentini. 'Structure and stability of rare-earth and transition-metal oxides'. *Physical Review B* 69 (2004) 17, 172103.

[2] S. Ohmi, C. Kobayashi, I. Kashiwagi, C. Ohshima, H. Ishiwara and H. Iwai. 'Characterization of La_2O_3 and Yb_2O_3 thin films for high-k gate insulator application'. *Journal of The Electrochemical Society* 150 (2003) 7, F134.

[3] B. Ali, L. R. Shah, C. Ni, J. Q. Xiao and S. I. Shah. 'Interplay of dopant, defects and electronic structure in driving ferromagnetism in Co-doped oxides: TiO_2, CeO_2 and ZnO'. *Journal of Physics-Condensed Matter* 21 (2009) 45, 456005.

[4] S. Pearton, C. Abernathy, D. Norton, A. Hebard, Y. Park, L. Boatner and J. Budai. 'Advances in wide bandgap materials for semiconductor spintronics'. *Materials Science and Engineering: R: Reports* 40 (2003) 4, 137.

[5] J. F. Wager. 'Transparent electronics'. *Science* 300 (2003) 5623, 1245.

[6] S. Katusic, P. Albers, R. Kern, F. M. Petrat, R. Sastrawan, S. Hore, A. Hinsch and A. Gutsch. 'Production and characterization of ITO-Pt semiconductor powder containing nanoscale noble metal particles catalytically active in dye-sensitized solar cells'. *Solar Energy Materials and Solar Cells* 90 (2006) 13, 1983.

[7] G. Eranna, B. C. Joshi, D. P. Runthala and R. P. Gupta. 'Oxide materials for development of integrated gas sensors - A comprehensive review'. *Critical Reviews in Solid State and Materials Sciences* 29 (2004) 3-4, 111.

[8] K. Zakrzewska. 'Mixed oxides as gas sensors'. *Thin Solid Films* 391 (2001) 2, 229.

[9] A. Tricoli, M. Graf and S. E. Pratsinis. 'Optimal doping for enhanced SnO_2 sensitivity and thermal stability'. *Advanced Functional Materials* 18 (2008) 13, 1969.

[10] A. Fujishima and K. Honda. 'Electrochemical photolysis of water at a semiconductor electrode'. *Nature* 238 (1972) 5358, 37.

[11] R. Asahi, T. Morikawa, T. Ohwaki, K. Aoki and Y. Taga. 'Visible-light photocatalysis in nitrogen-doped titanium oxides'. *Science* 293 (2001) 5528, 269.

[12] S. Livraghi, M. C. Paganini, E. Giamello, A. Selloni, C. Di Valentin and G. Pacchioni. 'Origin of photoactivity of nitrogen-doped titanium dioxide under visible light'. *Journal of the American Chemical Society* 128 (2006) 49, 15666.

[13] H. Ogawa, M. Nishikawa and A. Abe. 'Hall measurement studies and an electrical-conduction model of tin oxide ultrafine particle films'. *Journal of Applied Physics* 53 (1982) 6, 4448.

[14] N. Barsan and U. Weimar. 'Conduction model of metal oxide gas sensors'. *Journal of Electroceramics* 7 (2001) 3, 143.

[15] A. Rothschild and Y. Komem. 'The effect of grain size on the sensitivity of nanocrystalline metal-oxide gas sensors'. *Journal of Applied Physics* 95 (2004) 11, 6374.

[16] R. W. J. Scott, S. M. Yang, N. Coombs, G. A. Ozin and D. E. Williams. 'Engineered sensitivity of structured tin dioxide chemical sensors: Opaline architectures with controlled necking'. *Advanced Functional Materials* 13 (2003) 3, 225.

[17] A. Tricoli, M. Righettoni and S. E. Pratsinis. 'Minimal cross-sensitivity to humidity during ethanol detection by SnO_2-TiO_2 solid solutions'. *Nanotechnology* 20 (2009) 31, 315502.

[18] A. L. Linsebigler, G. Q. Lu and J. T. Yates. 'Photocatalysis on TiO_2 surfaces - Principles, mechanisms, and selected results'. *Chemical Reviews* 95 (1995) 3, 735.

[19] K. Maeda, T. Takata, M. Hara, N. Saito, Y. Inoue, H. Kobayashi and K. Domen. 'GaN:ZnO solid solution as a photocatalyst for visible-light-driven overall water splitting'. *Journal of the American Chemical Society* 127 (2005) 23, 8286.

[20] J. M. Herrmann. 'Heterogeneous photocatalysis: fundamentals and applications to the removal of various types of aqueous pollutants'. *Catalysis Today* 53 (1999) 1, 115.

[21] D. Chatterjee and S. Dasgupta. 'Visible light induced photocatalytic degradation of organic pollutants'. *Journal of Photochemistry and Photobiology C-Photochemistry Reviews* 6 (2005) 2-3, 186.

[22] C. Di Valentin, E. Finazzi, G. Pacchioni, A. Selloni, S. Livraghi, M. C. Paganini and E. Giamello. 'N-doped TiO_2: Theory and experiment'. *Chemical Physics* 339 (2007) 1-3, 44.

[23] J. K. Nørskov, J. Rossmeisl, A. Logadottir, L. Lindqvist, J. R. Kitchin, T. Bligaard and H. Jonsson. 'Origin of the overpotential for oxygen reduction at a fuel-cell cathode'. *Journal of Physical Chemistry B* 108 (2004) 46, 17886.

[24] F. Abild-Pedersen, J. Greeley, F. Studt, J. Rossmeisl, T. Munter, P. Moses, E. Skúlason, T. Bligaard and J. Nørskov. 'Scaling properties of adsorption energies for hydrogen-containing molecules on transition-metal surfaces'. *Physical Review Letters* 99 (2007) 1, 016105.

[25] F. Studt, F. Abild-Pedersen, H. Hansen, I. Man, J. Rossmeisl and T. Bligaard. 'Volcano relation for the deacon process over transition-metal oxides'. *ChemCatChem* 2 (2010) 1, 98.

[26] J. Suntivich, H. A. Gasteiger, N. Yabuuchi, H. Nakanishi, J. B. Goodenough and Y. Shao-Horn. 'Design principles for oxygen-reduction activity on perovskite oxide catalysts for fuel cells and metal-air batteries.' *Nature Chemistry* 3 (2011) 7, 546.

[27] S. L. Dudarev, D. N. Manh and A. P. Sutton. 'Effect of Mott-Hubbard correlations on the electronic structure and structural stability of uranium dioxide'. *Philosophical Magazine Part B* 75 (1997) 5, 613.

[28] G. B. Bachelet and N. E. Christensen. 'Relativistic and core-relaxation effects on the energy-bands of Gallium-Arsenide and Germanium'. *Physical Review B* 31 (1985) 2, 879.

[29] D. Andersson, S. Simak, B. Johansson, I. Abrikosov and N. Skorodumova. 'Modeling of CeO_2, Ce_2O_3, and CeO_{2x} in the LDA+U formalism'. *Physical Review B* 75 (2007) 3.

[30] J. L. F. Da Silva, M. V. Ganduglia-Pirovano, J. Sauer, V. Bayer and G. Kresse. 'Hybrid functionals applied to rare-earth oxides: The example of ceria'. *Physical Review B* 75 (2007) 4, 045121.

[31] D. Hamann. 'Semiconductor charge densities with hard-core and soft-core pseudopotentials'. *Physical Review Letters* 42 (1979) 10, 662.

[32] P. Huang and E. A. Carter. 'Advances in correlated electronic structure methods for solids, surfaces, and nanostructures'. *Annual Review of Physical Chemistry* 59 (2008), 261.

[33] K. R. Hahn, M. Iannuzzi, A. P. Seitsonen and J. Hutter. 'Coverage effect of the CO_2 adsorption mechanisms on CeO_2(111) by first principles analysis'. *Journal of Physical Chemistry C* 117 (2013) 4, 1701.

[34] K. R. Hahn, A. Tricoli, G. Santarossa, A. Vargas and A. Baiker. 'Theoretical study of the (110) surface of $Sn_{1-x}Ti_xO_2$ solid solutions with different distribution and content of Ti'. *Surface Science* 605 (2011) 15-16, 1476.

[35] K. R. Hahn, A. Tricoli, G. Santarossa, A. Vargas and A. Baiker. 'First principles analysis of H_2O adsorption on the (110) surfaces of SnO_2, TiO_2 and their solid solutions'. *Langmuir* 28 (2012) 2, 1646.

[36] R. M. Martin. *Electronic structure: Basic theory and practical methods.* Cambridge University Press, New York (2008).

[37] I. N. Levine. *Quantum Chemistry.* Pearson Education, Inc, Upper Saddle River, 6th edn. (2008).

[38] P. Hohenberg and W. Kohn. 'Inhomogeneous electron gas'. *Physical Review* 136 (1964) 3B, B864.

[39] W. Kohn. 'Electronic structure of matter - wave functions and density functionals'. *Nobel Lectures in Chemistry (1996-2000)*. World Scientific, Singapore (2003), pp. 213–237.

[40] L. Sham and W. Kohn. 'One-Particle properties of an inhomogeneous interacting electron gas'. *Physical Review* 145 (1966) 2, 561.

[41] M. Born and R. Oppenheimer. 'Zur Quantentheorie der Molekeln'. *Annalen der Physik* 389 (1927) 20, 457.

[42] V. I. Anisimov, J. Zaanen and O. K. Andersen. 'Band theory and Mott insulators: Hubbard U instead of Stoner I'. *Physical Review B* 44 (1991) 3, 943.

[43] A. D. Becke. 'A new mixing of Hartree-Fock and local density-functional theories'. *Journal of Chemical Physics* 98 (1993) 2, 1372.

[44] J. P. Perdew, M. Ernzerhof and K. Burke. 'Rationale for mixing exact exchange with density functional approximations'. *Journal of Chemical Physics* 105 (1996) 22, 9982.

[45] V. I. Anisimov, F. Aryasetiawan and A. I. Lichtenstein. 'First-principles calculations of the electronic structure and spectra of strongly correlated systems: the LDA + U method'. *Journal of Physics: Condensed Matter* 9 (1997) 4, 767.

[46] A. Kotani and T. Yamazaki. 'Systematic analysis of core photoemission spectra for actinide di-oxides and rare-earth sesqui-oxides'. *Progress of Theoretical Physics Supplement* (1992) 108, 117.

[47] S. L. Dudarev, G. A. Botton, S. Y. Savrasov, C. J. Humphreys and A. P. Sutton. 'Electron-energy-loss spectra and the structural stability of nickel oxide: An LSDA+U study'. *Physical Review B* 57 (1998) 3, 1505.

[48] M. Norman. 'Band theory and the insulating gap in CoO'. *Physical Review B* 40 (1989) 15, 10632.

[49] C. Lee, W. Yang and R. G. Parr. 'Development of the Colle-Salvetti correlation-energy formula into a functional of the electron density'. *Physical Review B* 37 (1988) 2, 785.

[50] G. Wannier. 'The structure of electronic excitation levels in insulating crystals'. *Physical Review* 52 (1937) 3, 191.

[51] G. Wannier. 'Dynamics of band electrons in electric and magnetic fields'. *Reviews of Modern Physics* 34 (1962) 4, 645.

[52] W. Kohn. 'Analytic properties of Bloch waves and Wannier functions'. *Physical Review* 115 (1959) 4, 809.

[53] N. Marzari, I. Souza and D. Vanderbilt. 'An introduction to maximally-localized Wannier functions'. *Psi-K Scientific Highlight of the Month, No 57* (2003), pp. 129–168.

[54] N. Marzari and D. Vanderbilt. 'Maximally localized generalized Wannier functions for composite energy bands'. *Physical Review B* 56 (1997) 20, 12847.

[55] N. Marzari, A. A. Mostofi, J. R. Yates, I. Souza and D. Vanderbilt. 'Maximally localized Wannier functions: Theory and applications'. *Reviews of Modern Physics* 84 (2012) 4, 1419.

[56] H. Jonsson, G. Mills and K. W. Jacobson. 'Nudged elastic band method for finding minimum energy paths of transitions'. B. J. Berne, G. Ciccotti and D. F. Coker (eds.), *Classical and Quantum Dynamics in Condensed Phase Simulations*. World Scientific (1998), pp. 385–404.

[57] G. Henkelman and H. Jonsson. 'Improved tangent estimate in the nudged elastic band method for finding minimum energy paths and saddle points'. *Journal of Chemical Physics* 113 (2000) 22, 9978.

[58] J. VandeVondele, M. Krack, F. Mohamed, M. Parrinello, T. Chassaing and J. Hutter. 'QUICKSTEP: Fast and accurate density functional calculations using a mixed Gaussian and plane waves approach'. *Computer Physics Communications* 167 (2005) 2, 103.

[59] CP2K Developers 2012 , CP2K is freely available from: www.cp2k.org.

[60] S. Goedecker, M. Teter and J. Hutter. 'Separable dual-space Gaussian pseudopotentials'. *Physical Review B* 54 (1996) 3, 1703.

[61] G. Lippert, J. Hutter and M. Parrinello. 'A hybrid Gaussian and plane wave density functional scheme'. *Molecular Physics* 92 (1997) 3, 477.

[62] J. VandeVondele and J. Hutter. 'Gaussian basis sets for accurate calculations on molecular systems in gas and condensed phases'. *Journal of Chemical Physics* 127 (2007) 11, 114105.

[63] J. P. Perdew, K. Burke and M. Ernzerhof. 'Generalized gradient approximation made simple'. *Physical Review Letters* 77 (1996) 18, 3865.

[64] J. VandeVondele and J. Hutter. 'An efficient orbital transformation method for electronic structure calculations'. *Journal of Chemical Physics* 118 (2003) 10, 4365.

[65] C. G. Broyden. 'The convergence of single-rank quasi-Newton methods'. *Mathematics of Computation* 24 (1970) 110, 365.

[66] R. Fletcher. 'A new approach to variable metric algorithms'. *The Computer Journal* 13 (1970) 3, 317.

[67] D. Goldfarb. 'A family of variable-metric methods derived by variational means'. *Mathematics of Computation* 24 (1970) 109, 23.

[68] D. F. Shanno and P. C. Kettler. 'Optimal conditioning of quasi-Newton methods'. *Mathematics of Computation* 24 (1970) 111, 657.

[69] G. A. Hussein. 'Rare earth metal oxides: formation, characterization and catalytic activity. Thermoanalytical and applied pyrolysis review'. *Journal of Analytical and Applied Pyrolysis* 37 (1996) 2, 111.

[70] K. C. Taylor. 'Automobile catalytic converters'. J. R. Anderson and M. Boudart (eds.), *Catalysis: Science and Technology*, vol. 5, chap. 2. Springer-Verlag, Berlin (1984).

[71] F. Uchikawa and J. D. Mackenzie. 'Superconducting $YBa_2Cu_3O_{7x}$ fibers from the thermoplastic gel method'. *Journal of Materials Research* 4 (1989) 04, 787.

[72] A. D. Berry, R. T. Holm, M. Fatemi and D. K. Gaskill. 'OMCVD of thin films from metal diketonates and triphenylbismuth'. *Journal of Materials Research* 5 (1990) 06, 1169.

[73] B. Schulte, M. Maul, W. Becker, E. G. Schlosser, S. Elschner, P. Haussler and H. Adrian. 'Carrier gas-free chemical vapor deposition technique for in situ preparation of high quality $YBa_2Cu_3O_{7\delta}$ thin films'. *Applied Physics Letters* 59 (1991) 7, 869.

[74] H. Osten, J. Liu, P. Gaworzewski, E. Bugiel and P. Zaumseil. 'High-k gate dielectrics with ultra-low leakage current based on praseodymium oxide'. *International Electron Devices Meeting 2000.* IEEE (2000), pp. 653–656.

[75] A. Trovarelli. 'Catalytic properties of ceria and CeO_2-containing materials'. *Catalysis Reviews-Science and Engineering* 38 (1996) 4, 439.

[76] G. Kim. 'Ceria-promoted three-way catalysts for auto exhaust emission control'. *Industrial & Engineering Chemistry Product Research and Development* 21 (1982) 2, 267.

[77] J. C. Summers and S. A. Ausen. 'Interaction of cerium oxide with noble metals'. *Journal of Catalysis* 58 (1979) 1, 131.

[78] N. Laosiripojana, D. Chadwick and S. Assabulnrungrat. 'Effect of high surface area CeO_2 and Ce-ZrO_2 supports over Ni catalyst on CH_4 reforming with H_2O in the presence of O_2, H_2, and CO_2'. *Chemical Engineering Journal* 138 (2008) 1-3, 264.

[79] W. C. Chueh, C. Falter, M. Abbott, D. Scipio, P. Furler, S. M. Haile and A. Steinfeld. 'High-flux solar-driven thermochemical dissociation of CO_2 and H_2O using nonstoichiometric ceria'. *Science* 330 (2010) 6012, 1797.

[80] E. Aneggi, M. Boaro, C. de Leitenburg, G. Dolcetti and A. Trovarelli. 'Insights into the redox properties of ceria-based oxides and their implications in catalysis'. *Journal of Alloys and Compounds* 408-412 (2006), 1096.

[81] J. Kašpar, P. Fornasiero and M. Graziani. 'Use of CeO_2-based oxides in the three-way catalysis'. *Catalysis Today* 50 (1999) 2, 285.

[82] S. Hilaire, X. Wang, T. Luo, R. J. Gorte and J. Wagner. 'A comparative study of water-gas-shift reaction over ceria supported metallic catalysts'. *Applied Catalysis A: General* 215 (2001) 1-2, 271.

[83] G. Jacobs, E. Chenu, P. M. Patterson, L. Williams, D. Sparks, G. Thomas and B. H. Davis. 'Water-gas shift: comparative screening of metal promoters for metal/ceria systems and role of the metal'. *Applied Catalysis A: General* 258 (2004) 2, 203.

[84] F. Marabelli and P. Wachter. 'Covalent insulator CeO_2 - optical reflectivity measurements'. *Physical Review B* 36 (1987) 2, 1238.

[85] L. Gerward, J. S. Olsen, L. Petit, G. Vaitheeswaran, V. Kanchana and A. Svane. 'Bulk modulus of CeO_2 and PrO_2 - An experimental and theoretical study'. *Journal of Alloys and Compounds* 400 (2005) 1-2, 56.

[86] A. Pfau and K. D. Schierbaum. 'The electronic-structure of stoichiometric and reduced CeO_2 surfaces - an XPS, UPS and HREELS study'. *Surface Science* 321 (1994) 1-2, 71.

[87] E. Wuilloud, B. Delley, W. D. Schneider and Y. Baer. 'Spectroscopic evidence for localized and extended f-symmetry states in CeO_2'. *Physical Review Letters* 53 (1984) 2, 202.

[88] P. J. Hay, R. L. Martin, J. Uddin and G. E. Scuseria. 'Theoretical study of CeO_2 and Ce_2O_3 using a screened hybrid density functional'. *Journal of Chemical Physics* 125 (2006) 3.

[89] M. Huang and S. Fabris. 'CO adsorption and oxidation on ceria surfaces from DFT+U calculations'. *Journal of Physical Chemistry C* 112 (2008) 23, 8643.

[90] J. Graciani, A. M. Márquez, J. J. Plata, Y. Ortega, N. C. Hernández, A. Meyer, C. M. Zicovich-Wilson and J. F. Sanz. 'Comparative study on the performance of hybrid DFT functionals in highly correlated oxides: The case of CeO_2 and Ce_2O_3'. *Journal of Chemical Theory and Computation* 7 (2011) 1, 56.

[91] M. Guidon, J. Hutter and J. VandeVondele. 'Auxiliary density matrix methods for Hartree-Fock exchange calculations'. *Journal of Chemical Theory and Computation* 6 (2010) 8, 2348.

[92] F. D. Murnaghan. 'The compressibility of media under extreme pressures'. *Proceedings of the National Academy of Sciences of the United States of America* 30 (1944) 9, 244.

[93] T. K. Woo, Z. X. Yang, M. Baudin and K. Hermansson. 'Atomic and electronic structure of unreduced and reduced CeO_2 surfaces: A first-principles study'. *Journal of Chemical Physics* 120 (2004) 16, 7741.

[94] A. Siokou and R. M. Nix. 'Interaction of methanol with well-defined ceria surfaces: Reflection/absorption infrared spectroscopy, X-ray photoelectron spectroscopy, and temperature-programmed desorption study'. *Journal of Physical Chemistry B* 103 (1999) 33, 6984.

[95] R. Dovesi, B. Civalleri, R. Orlando, C. Roetti and V. R. Saunders. 'Ab initio quantum simulation in solid state chemistry'. K. B. Lipkowitz, R. Larter and T. R. Cundari (eds.), *Reviews in Computational Chemistry*, vol. 21, chap. 1. John Wiley & Sons, Hoboken, New Jersey (2005).

[96] S. Fabris, G. Vicario, G. Balducci, S. de Gironcoli and S. Baroni. 'Electronic and atomistic structures of clean and reduced ceria surfaces'. *Journal of Physical Chemistry B* 109 (2005) 48, 22860.

[97] M. Nolan, S. Grigoleit, D. C. Sayle, S. C. Parker and G. W. Watson. 'Density functional theory studies of the structure and electronic structure of pure and defective low index surfaces of ceria'. *Surface Science* 576 (2005) 1-3, 217.

[98] N. Skorodumova, M. Baudin and K. Hermansson. 'Surface properties of CeO_2 from first principles'. *Physical Review B* 69 (2004) 7.

[99] S. Fabris, S. de Gironcoli, S. Baroni, G. Vicario and G. Balducci. 'Taming multiple valency with density functionals: A case study of defective ceria'. *Physical Review B* 71 (2005) 4, 041102(R).

[100] D. Mullins, P. Radulovic and S. Overbury. 'Ordered cerium oxide thin films grown on Ru(0001) and Ni(111)'. *Surface Science* 429 (1999) 1-3, 186.

[101] M. Henderson, C. Perkins, M. Engelhard, S. Thevuthasan and C. Peden. 'Redox properties of water on the oxidized and reduced surfaces of CeO_2'. *Surface Science* 526 (2003) 1-2, 1.

[102] F. Esch, S. Fabris, L. Zhou, T. Montini, C. Africh, P. Fornasiero, G. Comelli and R. Rosei. 'Electron localization determines defect formation on ceria substrates'. *Science* 309 (2005) 5735, 752.

[103] M. Cococcioni and S. de Gironcoli. 'Linear response approach to the calculation of the effective interaction parameters in the LDA+U method'. *Physical Review B* 71 (2005) 3, 035105.

[104] J. F. Jerratsch, X. Shao, N. Nilius, H. J. Freund, C. Popa, M. V. Ganduglia-Pirovano, A. M. Burow and J. Sauer. 'Electron localization in defective ceria films: A study with scanning-tunneling microscopy and density-functional theory'. *Physical Review Letters* 106 (2011) 24, 246801.

[105] M. Ganduglia-Pirovano, J. Da Silva and J. Sauer. 'Density-functional calculations of the structure of near-surface oxygen vacancies and electron localization on CeO_2(111)'. *Physical Review Letters* 102 (2009) 2, 026101.

[106] Y.-M. Chiang, E. Lavik and D. Blom. 'Defect thermodynamics and electrical properties of nanocrystalline oxides: pure and doped CeO_2'. *Nanostructured Materials* 9 (1997) 1-8, 633.

[107] C. T. Campbell. 'Ultrathin metal films and particles on oxide surfaces: structural, electronic and chemisorptive properties'. *Surface Science Reports* 27 (1997) 1-3, 1.

[108] Y. Zhai, D. Pierre, R. Si, W. Deng, P. Ferrin, A. U. Nilekar, G. Peng, J. A. Herron, D. C. Bell, H. Saltsburg, M. Mavrikakis and M. Flytzani-Stephanopoulos. 'Alkali-stabilized Pt-OH_x species catalyze low-temperature water-gas shift reactions.' *Science* 329 (2010) 5999, 1633.

[109] A. Phatak, N. Koryabkina, S. Rai, J. Ratts, W. Ruettinger, R. Farrauto, G. Blau, W. Delgass and F. Ribeiro. 'Kinetics of the water-gas shift reaction on Pt catalysts supported on alumina and ceria'. *Catalysis Today* 123 (2007) 1-4, 224.

[110] P. Panagiotopoulou, A. Christodoulakis, D. Kondarides and S. Boghosian. 'Particle size effects on the reducibility of titanium dioxide and its relation to the water-gas shift activity of Pt/TiO_2 catalysts'. *Journal of Catalysis* 240 (2006) 2, 114.

[111] G. N. Vayssilov, Y. Lykhach, A. Migani, T. Staudt, G. P. Petrova, N. Tsud, T. Skála, A. Bruix, F. Illas, K. C. Prince, V. Matolin, K. M. Neyman and J. Libuda. 'Support nanostructure boosts oxygen transfer to catalytically active platinum nanoparticles'. *Nature Materials* 10 (2011) 4, 310.

[112] W. Wang and J. Gong. 'Methanation of carbon dioxide: an overview'. *Frontiers of Chemical Science and Engineering* 5 (2011) 1, 2.

[113] X. Du, D. Zhang, L. Shi, R. Gao and J. Zhang. 'Morphology dependence of catalytic properties of Ni/CeO_2 nanostructures for carbon dioxide reforming of methane'. *Journal of Physical Chemistry C* 116 (2012) 18, 10009.

[114] C. R. Henry. 'Surface studies of supported model catalysts'. *Surface Science Reports* 31 (1998) 7-8, 231.

[115] F.-W. Chang, M.-T. Tsay and S.-P. Lang. 'Hydrogenation of CO_2 over nickel catalysts supported on rice husk ash prepared by ion exchange'. *Applied Catalysis A: General* 209 (2001) 1-2, 217.

[116] G. Pacchioni. 'Electronic interactions and charge transfers of metal atoms and clusters on oxide surfaces'. *Physical Chemistry Chemical Physics* 15 (2013) 6, 1737.

[117] A. Bruix, J. A. Rodriguez, P. J. Ramirez, S. D. Senanayake, J. Evans, J. B. Park, D. Stacchiola, P. Liu, J. Hrbek and F. Illas. 'A new type of strong metal-support interaction and the production of H_2 through the transformation of water on $Pt/CeO_2(111)$ and $Pt/CeO_x/TiO_2(110)$ catalysts'. *Journal of the American Chemical Society* 134 (2012) 21, 8968.

[118] F. Cova, D. G. Pintos, A. Juan and B. Irigoyen. 'A first-principles modeling of Ni interactions on CeO_2-ZrO_2 mixed oxide solid solutions'. *Journal of Physical Chemistry C* 115 (2011) 15, 7456.

[119] S. Xu and X. Wang. 'Highly active and coking resistant Ni/CeO_2-ZrO_2 catalyst for partial oxidation of methane'. *Fuel* 84 (2005) 5, 563.

[120] L. Barrio, A. Kubacka, G. Zhou, M. Estrella, A. Martínez-Arias, J. C. Hanson, M. Fernández-García and J. A. Rodriguez. 'Unusual physical and chemical properties of Ni in $Ce_{1x}Ni_xO_{2y}$ oxides: Structural characterization and catalytic activity for the water gas shift reaction'. *Journal of Physical Chemistry C* 114 (2010) 29, 12689.

[121] S. D. Senanayake, J. Evans, S. Agnoli, L. Barrio, T.-L. Chen, J. Hrbek and J. A. Rodriguez. 'Water-gas shift and CO methanation reactions over $NiCeO_2(111)$ catalysts'. *Topics in Catalysis* 54 (2011) 1-4, 34.

[122] G. A. Deluga, J. R. Salge, L. D. Schmidt and X. E. Verykios. 'Renewable hydrogen from ethanol by autothermal reforming'. *Science* 303 (2004) 5660, 993.

[123] A. Haryanto, S. Fernando, N. Murali and S. Adhikari. 'Current status of hydrogen production techniques by steam reforming of ethanol: A review'. *Energy & Fuels* 19 (2005) 5, 2098.

[124] R. Farrauto, S. Hwang, L. Shore, W. Ruettinger, J. Lampert, T. Giroux, Y. Liu and O. Ilinich. 'New material needs for hydrogen fuel processing: Generating hydrogen for the PEM fuel cell'. *Annual Review of Materials Research* 33 (2003) 1, 1.

[125] A. Trovarelli, C. de Leitenburg, M. Boaro and G. Dolcetti. 'The utilization of ceria in industrial catalysis'. *Catalysis Today* 50 (1999) 2, 353.

[126] Y. Zhou, J. M. Perket, A. B. Crooks and J. Zhou. 'Effect of ceria support on the structure of Ni nanoparticles'. *Journal of Physical Chemistry Letters* 1 (2010) 9, 1447.

[127] J. P. Perdew and Y. Wang. 'Accurate and simple analytic representation of the electron-gas correlation energy'. *Physical Review B* 45 (1992) 23, 13244.

[128] Z. Chafi, N. Keghouche and C. Minot. 'DFT study of Ni-CeO_2 interaction: Adsorption and insertion'. *Surface Science* 601 (2007) 11, 2323.

[129] Z. Lu, Z. Yang and K. Hermansson. 'The adsorption properties of Cu and Ni on the ceria(111) surface'. *Advanced Materials Research* 213 (2011), 166.

[130] J. Carrasco, L. Barrio, P. Liu, J. A. Rodriguez and M. V. Ganduglia-Pirovano. 'Theoretical studies for the adsorption of CO and C on Ni(111) and Ni/CeO_2 (111): Evidence for a strong metal-support interaction'. *Journal of Physical Chemistry C* 117 (2013) 16, 8241.

[131] B. V. Reddy, S. K. Nayak, S. N. Khanna, B. K. Rao and P. Jena. 'Physics of nickel clusters. 2. Electronic structure and magnetic properties'. *Journal of Physical Chemistry A* 102 (1998) 10, 1748.

[132] Q. L. Lu, Q. Q. Luo, L. L. Chen and J. G. Wan. 'Structural and magnetic properties of Ni_n (n = 221) clusters'. *European Physical Journal D* 61 (2011) 2, 389.

[133] G. A. Cisneros, M. Castro and D. R. Salahub. 'DFT study of the structural and electronic properties of small Ni_n (n=2-4) clusters'. *International Journal of Quantum Chemistry* 75 (1999) 4-5, 847.

[134] M. C. Michelini, R. Pis Diez and A. H. Jubert. 'Density functional study of small Ni clusters, with n=2-6, 8, using the generalized gradient approximation'. *International Journal of Quantum Chemistry* 85 (2001) 1, 22.

[135] A. N. Andriotis. 'Magnetic properties of Ni and Fe clusters: a tight binding molecular dynamics study'. *Chemical Physics Letters* 260 (1996) 1-2, 15.

[136] Z. X. Yang, Z. M. Fu, Y. N. Zhang and R. Q. Wu. 'Direct CO oxidation by lattice oxygen on Zr-doped ceria surfaces'. *Catalysis Letters* 141 (2011) 1, 78.

[137] Y. Yoshida, Y. Arai, S. Kado, K. Kunimori and K. Tomishige. 'Direct synthesis of organic carbonates from the reaction of CO_2 with methanol and ethanol over CeO_2 catalysts'. *Catalysis Today* 115 (2006) 1-4, 95.

[138] S. Sharma, Z. P. Hu, P. Zhang, E. W. McFarland and H. Metiu. 'CO_2 methanation on Ru-doped ceria'. *Journal of Catalysis* 278 (2011) 2, 297.

[139] H.-J. Freund and M. W. Roberts. 'Surface chemistry of carbon dioxide'. *Surface Science Reports* 25 (1996) 8, 225.

[140] R. G. Copperthwaite, P. R. Davies, M. A. Morris, M. W. Roberts and R. A. Ryder. 'The reactive chemisorption of carbon dioxide at magnesium and copper surfaces at low temperature'. *Catalysis Letters* 1 (1988) 1-3, 11.

[141] P. Rasmussen, P. Taylor and I. Chorkendorff. 'The interaction of carbon dioxide with Cu(100)'. *Surface Science* 269-270 (1992), 352.

[142] G.-C. Wang, L. Jiang, Y. Morikawa, J. Nakamura, Z.-S. Cai, Y.-M. Pan and X.-Z. Zhao. 'Cluster and periodic DFT calculations of adsorption and activation of CO_2 on the Cu(hkl) surfaces'. *Surface Science* 570 (2004) 3, 205.

[143] J. Krause, D. Borgmann and G. Wedler. 'Photoelectron spectroscopic study of the adsorption of carbon dioxide on Cu(110) and Cu(110)/K as compared with the systems Fe(110)/CO_2 and Fe(110)/K+CO_2'. *Surface Science* 347 (1996) 1-2, 1.

[144] P. R. Norton and P. J. Richards. 'A photoelectron spectroscopic study of the adsorption of CO and CO_2 on platinum'. *Surface Science* 49 (1975) 2, 567.

[145] C. F. Zinola, C. Gomis-Bas, G. L. Estiú, E. A. Castro and A. J. Arvia. 'A semiempirical quantum approach to the formation of carbon dioxide adsorbates on Pt(100) and Pt(111) cluster surfaces'. *Langmuir* 14 (1998) 14, 3901.

[146] F. Solymosi and A. Berkó. 'Adsorption of CO_2 on clean and potassium-covered Pd(100) surfaces'. *Journal of Catalysis* 101 (1986) 2, 458.

[147] D. Ehrlich, S. Wohlrab, J. Wambach, H. Kuhlenbeck and H.-J. Freund. 'Reaction of CO_2 on Pd(111) activated via promotor action of alkali coadsorption'. *Vacuum* 41 (1990) 1-3, 157.

[148] M. H. Nassir. 'Sequential carbon oxygen bond cleavage in chemisorption of CO_2 on Fe(100)'. *Journal of Vacuum Science & Technology A: Vacuum, Surfaces, and Films* 11 (1993) 4, 2104.

[149] G. Meyer, E. Reinhart, D. Borgmann and G. Wedler. 'Interaction of carbon dioxide with potassium-promoted Fe(110) I. Dependence on potassium coverage and carbon dioxide exposure at 85 K'. *Surface Science* 320 (1994) 1-2, 110.

[150] S.-G. Wang, X.-Y. Liao, D.-B. Cao, C.-F. Huo, Y.-W. Li, J. Wang and H. Jiao. 'Factors controlling the interaction of CO_2 with transition metal surfaces'. *Journal of Physical Chemistry C* 45, 16934.

[151] X. Ding, V. Pagan, M. Peressi and F. Ancilotto. 'Modeling adsorption of CO_2 on Ni(110) surface'. *Materials Science and Engineering: C* 27 (2007) 5-8, 1355.

[152] R. Hammami, A. Dhouib, S. Fernandez and C. Minot. 'CO_2 adsorption on (001) surfaces of metal monoxides with rock-salt structure'. *Catalysis Today* 139 (2008) 3, 227.

[153] A. Markovits, A. Fahmi and C. Minot. 'A theoretical study of CO_2 adsorption on TiO_2'. *Journal of Molecular Structure: THEOCHEM* 371 (1996), 219.

[154] D. C. Sorescu, J. Lee, W. A. Al-Saidi and K. D. Jordan. 'CO_2 adsorption on TiO_2(110) rutile: Insight from dispersion-corrected density functional theory calculations and scanning tunneling microscopy experiments'. *Journal of Chemical Physics* 134 (2011) 10, 104707.

[155] R. Hammami, H. Batis and C. Minot. 'Combined experimental and theoretical investigation of the CO_2 adsorption on $LaMnO_{3+y}$ perovskite oxide'. *Surface Science* 603 (2009) 20, 3057.

[156] M. Calatayud, A. Markovits, M. Menetrey, B. Mguig and C. Minot. 'Adsorption on perfect and reduced surfaces of metal oxides'. *Catalysis Today* 85 (2003) 2-4, 125.

[157] A. Markovits, J. Ahdjoudj and C. Minot. 'Theoretical study of the adsorption of acids and bases on TiO_2 and MgO surfaces'. *Nuovo Cimento della Societa Italiana di Fisica D-Condensed Matter Atomic Molecular and Chemical Physics Fluids Plasmas Biophysics* 19 (1997) 11, 1719.

[158] T. Jin, Y. Zhou, G. J. Mains and J. M. White. 'Infrared and x-ray photoelectron-spectroscopy study of CO and CO_2 on Pt/CeO_2'. *Journal of Physical Chemistry* 91 (1987) 23, 5931.

[159] P. Bagus, C. Nelin, E. Ilton, M. Baron, H. Abbott, E. Primorac, H. Kuhlenbeck, S. Shaikhutdinov and H.-J. Freund. 'The complex core level spectra of CeO_2: An analysis in terms of atomic and charge transfer effects'. *Chemical Physics Letters* 487 (2010) 4-6, 237.

[160] M. Breysse, M. Guenin, B. Claudel and J. Veron. 'Catalysis of carbon monoxide oxidation by cerium dioxide. 2. Microcalorimetric investigation of adsorption and catalysis'. *Journal of Catalysis* 28 (1973) 1, 54.

[161] E. Aneggi, J. Llorca, M. Boaro and A. Trovarelli. 'Surface-structure sensitivity of CO oxidation over polycrystalline ceria powders'. *Journal of Catalysis* 234 (2005) 1, 88.

[162] Z. Cheng, B. J. Sherman and C. S. Lo. 'Carbon dioxide activation and dissociation on Ceria(110): A density functional theory study'. *Journal of Chemical Physics* 138 (2013) 1, 014702.

[163] S. Grimme. 'Semiempirical GGA-type density functional constructed with a long-range dispersion correction'. *Journal of Computational Chemistry* 27 (2006) 15, 1787.

[164] G. Herzberg. *Molecular spectra and molecular structure*, vol. 3. Van Nostrand, New York (1966).

[165] R. S. Mulliken. 'Electronic population analysis on LCAO-MO molecular wave functions'. *Journal of Chemical Physics* 23 (1955) 10, 1833.

[166] D. R. Lide. *CRC Handbook of Chemistry and Physics*. Taylor & Francis, 75th edn. (1994).

[167] X. Ding, L. De Rogatis, E. Vesselli, A. Baraldi, G. Comelli, R. Rosei, L. Savio, L. Vattuone, M. Rocca, P. Fornasiero, F. Ancilotto, A. Baldereschi and M. Peressi. 'Interaction of carbon dioxide with Ni(110): A combined experimental and theoretical study'. *Physical Review B* 76 (2007) 19.

[168] H. He, P. Zapol and L. A. Curtiss. 'A theoretical study of CO_2 anions on anatase (101) surface'. *Journal of Physical Chemistry C* 114 (2010) 49, 21474.

[169] P. W. Park, H. H. Kung, D. W. Kim and M. C. Kung. 'Characterization of SnO_2/Al_2O_3 lean NO_x catalysts'. *Journal of Catalysis* 184 (1999) 2, 440.

[170] M. Batzill and U. Diebold. 'The surface and materials science of tin oxide'. *Progress in Surface Science* 79 (2005) 2-4, 47.

[171] D. H. Solomon and D. G. Hawthorne. *Chemistry of Pigments and Fillers*. John Wiley and Sons, New York (1983).

[172] J. Lademann, H. J. Weigmann, H. Schaefer, G. Mueller and W. Sterry. 'Laser spectroscopic investigation of the stability of coated titanium microparticles used in sunscreens'. *Laser Physics* 10 (2000) 2, 478.

[173] F. Fresno, D. Tudela, J. M. Coronado, M. Fernández-García, A. B. Hungría and J. Soria. 'Influence of Sn^{4+} on the structural and electronic properties of $Ti_{1-x}Sn_xO_2$ nanoparticles used as photocatalysts'. *Physical Chemistry Chemical Physics* 8 (2006) 20, 2421.

[174] R. Méndez-Román and N. Cardona-Martínez. 'Relationship between the formation of surface species and catalyst deactivation during the gas-phase photocatalytic oxidation of toluene'. *Catalysis Today* 40 (1998) 4, 353.

[175] F. Fresno, M. D. Hernández-Alonso, D. Tudela, J. M. Coronado and J. Soria. 'Photocatalytic degradation of toluene over doped and coupled (Ti,M)O_2 (M = Sn or Zr) nanocrystalline oxides: Influence of the heteroatom distribution on deactivation'. *Applied Catalysis B-Environmental* 84 (2008) 3-4, 598.

[176] F. E. Oropeza, B. Davies, R. G. Palgrave and R. G. Egdell. 'Electronic basis of visible region activity in high area Sn-doped rutile TiO_2 photocatalysts'. *Physical Chemistry Chemical Physics* 13 (2011) 17, 7882.

[177] F. R. Sensato, R. Custódio, E. Longo, A. Beltrán and J. Andrés. 'Electronic and structural properties of $Sn_xTi_{1-x}O_2$ solid solutions: A periodic DFT study'. *Catalysis Today* 85 (2003) 2-4, 145.

[178] W. Lin, Y. F. Zhang, Y. Li, K. N. Ding, J. Q. Li and Y. J. Xu. 'Structural characterizations and electronic properties of Ti-doped SnO_2(110) surface: A first-principles study'. *Journal of Chemical Physics* 124 (2006) 5, 54704.

[179] J. R. Sambrano, G. F. Nobrega, C. A. Taft, J. Andrés and A. Beltrán. 'A theoretical analysis of the TiO_2/Sn doped (110) surface properties'. *Surface Science* 580 (2005) 1-3, 71.

[180] R. A. Evarestov, A. V. Bandura and E. V. Proskurov. 'Plain DFT and hybrid HF-DFT LCAO calculations of SnO_2(110) and (100) bare and hydroxylated surfaces'. *Physica Status Solidi B-Basic Solid State Physics* 243 (2006) 8, 1823.

[181] M. Ramamoorthy, D. Vanderbilt and R. D. Kingsmith. '1st-Principles calculations of the energetics of stoichiometric TiO_2 surfaces'. *Physical Review B* 49 (1994) 23, 16721.

[182] A. V. Bandura, J. D. Kubicki and J. O. Sofo. 'Comparisons of multilayer H_2O adsorption onto the (110) surfaces of alpha-TiO_2 and SnO_2 as calculated with density functional theory'. *Journal of Physical Chemistry B* 112 (2008) 37, 11616.

[183] Z. G. Zhu, R. C. Deka, A. Chutia, R. Sahnoun, H. Tsuboi, M. Koyama, N. Hatakeyama, A. Endou, H. Takaba, C. A. Del Carpio, M. Kubo and A. Miyamoto. 'Enhanced gas-sensing behaviour of Ru-doped SnO_2 surface: A periodic density functional approach'. *Journal of Physics and Chemistry of Solids* 70 (2009) 9, 1248.

[184] Y. B. Xue and Z. A. Tang. 'Density functional study of the interaction of CO with undoped and Pd doped SnO_2(110) surface'. *Sensors and Actuators B-Chemical* 138 (2009) 1, 108.

[185] Y. Yamaguchi, K. Tabata and T. Yashima. 'First-principles calculations on the surface electronic and reactive properties of M/SnO_2 (M = Ge, Mn) (110)'. *Journal of Molecular Structure-Theochem* 714 (2005) 2-3, 221.

[186] R. Long, N. J. English and Y. Dai. 'First-principles study of S doping at the rutile TiO_2(110) surface'. *Journal of Physical Chemistry C* 113 (2009) 40, 17464.

[187] G. Lippert, J. Hutter and M. Parrinello. 'The Gaussian and augmented-plane-wave density functional method for ab initio molecular dynamics simulations'. *Theoretical Chemistry Accounts* 103 (1999) 2, 124.

[188] F. Schiffmann, J. Hutter and J. VandeVondele. 'Atomistic simulations of a solid/liquid interface: a combined force field and first principles approach to the structure and dynamics of acetonitrile near an anatase surface'. *Journal of Physics-Condensed Matter* 20 (2008) 6, 64206.

[189] J. P. Perdew and M. Levy. 'Physical content of the exact Kohn-Sham orbital energies - band-gaps and derivative discontinuities'. *Physical Review Letters* 51 (1983) 20, 1884.

[190] L. J. Sham and M. Schluter. 'Density-functional theory of the energy-gap'. *Physical Review Letters* 51 (1983) 20, 1888.

[191] K. J. Hameeuw, G. Cantele, D. Ninno, F. Trani and G. Iadonisi. 'The rutile TiO_2(110) surface: Obtaining converged structural properties from first-principles calculations'. *Journal of Chemical Physics* 124 (2006) 2, 24708.

[192] P. J. D. Lindan, N. M. Harrison, M. J. Gillan and J. A. White. 'First-principles spin-polarized calculations on the reduced and reconstructed TiO_2(110) surface'. *Physical Review B* 55 (1997) 23, 15919.

[193] J. Oviedo and M. J. Gillan. 'The energetics and structure of oxygen vacancies on the SnO_2(110) surface'. *Surface Science* 467 (2000) 1-3, 35.

[194] A. A. Bolzan, C. Fong, B. J. Kennedy and C. J. Howard. 'Structural studies of rutile-type metal dioxides'. *Acta Crystallographica Section B-Structural Science* 53 (1997), 373.

[195] S. C. Abrahams and J. L. Bernstein. 'Rutile - normal probability plot analysis and accurate measurement of crystal structure'. *Journal of Chemical Physics* 55 (1971) 7, 3206.

[196] R. D. Shannon and C. T. Prewitt. 'Effective ionic radii in oxides and fluorides'. *Acta Crystallographica Section B-Structural Crystallography and Crystal Chemistry* B 25 (1969), 925.

[197] G. Q. Qin, D. C. Li, Z. W. Chen, Y. L. Hou, Z. J. Feng and S. M. Liu. 'Structural, electronic and optical properties of $Sn_{1-x}Sb_xO_2$'. *Computational Materials Science* 46 (2009) 2, 418.

[198] M. Park, T. E. Mitchell and A. H. Heuer. 'Subsolidus equilibria in TiO_2-SnO_2 system'. *Journal of the American Ceramic Society* 58 (1975) 1-2, 43.

[199] T. Hirata, K. Ishioka, M. Kitajima and H. Doi. 'Concentration dependence of optical phonons in the TiO_2-SnO_2 system'. *Physical Review B* 53 (1996) 13, 8442.

[200] P. J. D. Lindan. 'Water chemistry at the SnO_2(110) surface: the role of inter-molecular interactions and surface geometry'. *Chemical Physics Letters* 328 (2000) 4-6, 325.

[201] G. Cabailh, X. Torrelles, R. Lindsay, O. Bikondoa, I. Joumard, J. Zegenhagen and G. Thornton. 'Geometric structure of TiO_2(110) (1x1): Achieving experimental consensus'. *Physical Review B* 75 (2007) 24, 241403.

[202] L. Grabow, Y. Xu and M. Mavrikakis. 'Lattice strain effects on CO oxidation on Pt(111)'. *Physical Chemistry Chemical Physics* 8 (2006) 29, 3369.

[203] H. Y. Kim, H. M. Lee, R. G. S. Pala, V. Shapovalov and H. Metiu. 'CO oxidation by rutile TiO_2(110) doped with V, W, Cr, Mo, and Mn'. *Journal of Physical Chemistry C* 112 (2008) 32, 12398.

[204] S. D. Gardner, G. B. Hoflund, D. R. Schryer, J. Schryer, B. T. Upchurch and E. J. Kielin. 'Catalytic behavior of noble-metal reducible oxide materials for low-temperature CO oxidation: 1. Comparison of catalyst performance'. *Langmuir* 7 (1991) 10, 2135.

[205] B. H. Engler. 'Catalysts for environmental-protection'. *Chemie Ingenieur Technik* 63 (1991) 4, 298.

[206] P. Bera, A. Gayen, M. S. Hegde, N. P. Lalla, L. Spadaro, F. Frusteri and F. Arena. 'Promoting effect of CeO_2 in combustion synthesized Pt/CeO_2 catalyst for CO oxidation'. *Journal of Physical Chemistry B* 107 (2003) 25, 6122.

[207] T. Baidya, A. Gayen, M. S. Hegde, N. Ravishankar and L. Dupont. 'Enhanced reducibility of $Ce_{1-x}Ti_xO_2$ compared to that of CeO_2 and higher redox catalytic activity of $Ce_{1-x-y}Ti_xPt_yO_{2-\delta}$ compared to that of $Ce_{1-x}Pt_xO_{2-\delta}$'. *Journal of Physical Chemistry B* 110 (2006) 11, 5262.

[208] W. J. Shan, Z. C. Feng, Z. L. Li, Z. Jing, W. J. Shen and L. Can. 'Oxidative steam reforming of methanol on $Ce_{0.9}Cu_{0.1}O_Y$ catalysts prepared by deposition-precipitation, coprecipitation, and complexation-combustion methods'. *Journal of Catalysis* 228 (2004) 1, 206.

[209] M. R. Hoffmann, S. T. Martin, W. Y. Choi and D. W. Bahnemann. 'Environmental applications of semiconductor photocatalysis'. *Chemical Reviews* 95 (1995) 1, 69.

[210] S. Sato and J. M. White. 'Photodecomposition of water over Pt/TiO_2 catalysts'. *Chemical Physics Letters* 72 (1980) 1, 83.

[211] F. Fresno, J. A. Coronado, D. Tudela and J. Soria. 'Influence of the structural characteristics of $Ti_{1-x}Sn_xO_2$ nanoparticles on their photocatalytic activity for the elimination of methylcyclohexane vapors'. *Applied Catalysis B-Environmental* 55 (2005) 3, 159.

[212] Y. Paz. 'Photocatalytic treatment of air: From basic aspects to reactors'. I. d. L. Hugo and R. Benito Serrano (eds.), *Advances in Chemical Engineering*, vol. 36. Academic Press (2009), pp. 289–336.

[213] L. A. Phillips and G. B. Raupp. 'Infrared spectroscopic investigation of gas solid heterogeneous photocatalytic oxidation of trichloroethylene'. *Journal of Molecular Catalysis* 77 (1992) 3, 297.

[214] M. Anpo, K. Chiba, M. Tomonari, S. Coluccia, M. Che and M. A. Fox. 'Photocatalysis on native and platinum-loaded TiO_2 and ZnO catalysts - origin of different reactivities on wet and dry metal oxides'. *Bulletin of the Chemical Society of Japan* 64 (1991) 2, 543.

[215] J. Peral and D. F. Ollis. 'Heterogeneous photocatalytic oxidation of gas-phase organics for air purification - acetone, 1-butanol, butyraldehyde, formaldehyde, and meta-xylene oxidation'. *Journal of Catalysis* 136 (1992) 2, 554.

[216] W. H. Brattain and J. Bardeen. 'Surface properties of Germanium'. *Bell System Technical Journal* 32 (1953) 1, 1.

[217] W. H. Brattain and C. G. B. Garrett. 'Surface properties of semiconductors'. *Physica* 20 (1954) 10, 885.

[218] E. S. Snow, F. K. Perkins, E. J. Houser, S. C. Badescu and T. L. Reinecke. 'Chemical detection with a single-walled carbon nanotube capacitor'. *Science* 307 (2005) 5717, 1942.

[219] N. Yamazoe and N. Miura. 'Gas Sensors: Principles, Operation and Developments'. G. Sberveglieri (ed.), *New Approaches in the Design of Gas Sensors*. Kluwer Academic Publishers Group, Dordrecht (1992).

[220] D. C. Ciccel. 'Highway Saftey Programs; Conforming products list of screening devices to measure alcoholin bodily fluids' (2009).

[221] C. Di Natale, A. Macagnano, E. Martinelli, R. Paolesse, G. D'Arcangelo, C. Roscioni, A. Finazzi-Agro and A. D'Amico. 'Lung cancer identification by the analysis of breath by means of an array of non-selective gas sensors'. *Biosensors & Bioelectronics* 18 (2003) 10, 1209.

[222] L. Wang, A. Teleki, S. E. Pratsinis and P. I. Gouma. 'Ferroelectric WO_3 nanoparticles for acetone selective detection'. *Chemistry of Materials* 20 (2008) 15, 4794.

[223] G. Korotcenkov. 'Gas response control through structural and chemical modification of metal oxide films: state of the art and approaches'. *Sensors and Actuators B-Chemical* 107 (2005) 1, 209.

[224] X. G. Han, M. S. Jin, S. F. Xie, Q. Kuang, Z. Y. Jiang, Y. Q. Jiang, Z. X. Xie and L. S. Zheng. 'Synthesis of tin dioxide octahedral nanoparticles with exposed high-energy (221) facets and enhanced gas-sensing properties'. *Angewandte Chemie-International Edition* 48 (2009) 48, 9180.

[225] A. Tricoli, M. Righettoni and A. Teleki. 'Semiconductor gas sensors: Dry synthesis and application'. *Angewandte Chemie-International Edition* 49 (2010) 42, 7632.

[226] B. Thiel and R. Helbig. 'Growth of SnO_2 single-crystals by a vapor-phase reaction method'. *Journal of Crystal Growth* 32 (1976) 2, 259.

[227] W. Q. Cao and Y. X. Duan. 'Breath analysis: Potential for clinical diagnosis and exposure assessment'. *Clinical Chemistry* 52 (2006) 5, 800.

[228] N. Barsan and U. Weimar. 'Understanding the fundamental principles of metal oxide based gas sensors; the example of CO sensing with SnO_2 sensors in the presence of humidity'. *Journal of Physics-Condensed Matter* 15 (2003) 20, R813.

[229] M. Righettoni, A. Tricoli and S. E. Pratsinis. 'Si:WO_3 sensors for highly selective detection of acetone for easy diagnosis of diabetes by breath analysis'. *Analytical Chemistry* 82 (2010) 9, 3581.

[230] G. Heiland, D. Kohl and T. Seiyama. 'Physical and chemical aspects of oxidic semiconductor gas sensors'. T. Seiyama (ed.), *Chemical Sensor Technology*, vol. 1, chap. 15-38. Kodansha, Tokyo (1988), pp. 15–38.

[231] S. R. Morrison. *The Chemical Physics of Surfaces*. Plenum, New York, 2nd edn. (1990).

[232] V. A. Henrich and P. A. Cox. *The Surface Science of Metal Oxides*. Cambridge University Press, Cambridge (1994).

[233] L. C. Grabow, A. A. Gokhale, S. T. Evans, J. A. Dumesic and M. Mavrikakis. 'Mechanism of the water gas shift reaction on Pt: First principles, experiments, and microkinetic modeling'. *Journal of Physical Chemistry C* 112 (2008) 12, 4608.

[234] J. L. Zhang, M. B. Vukmirovic, K. Sasaki, A. U. Nilekar, M. Mavrikakis and R. R. Adzic. 'Mixed-metal Pt monolayer electrocatalysts for enhanced oxygen reduction kinetics'. *Journal of the American Chemical Society* 127 (2005) 36, 12480.

[235] M. Ojeda, R. Nabar, A. U. Nilekar, A. Ishikawa, M. Mavrikakis and E. Iglesia. 'CO activation pathways and the mechanism of Fischer-Tropsch synthesis'. *Journal of Catalysis* 272 (2010) 2, 287.

[236] J. I. Martínez, H. A. Hansen, J. Rossmeisl and J. K. Nørskov. 'Formation energies of rutile metal dioxides using density functional theory'. *Physical Review B* 79 (2009) 4, 45120.

[237] F. R. Sensato, R. Custódio, M. Calatayud, A. Beltrán, J. Andrés, J. R. Sambrano and E. Longo. 'Periodic study on the structural and electronic properties of bulk, oxidized and reduced SnO_2(110) surfaces and the interaction with O_2'. *Surface Science* 511 (2002) 1-3, 408.

[238] S. Wendt, R. Schaub, J. Matthiesen, E. K. Vestergaard, E. Wahlström, M. D. Rasmussen, P. Thostrup, L. M. Molina, E. Lægsgaard, I. Stensgaard, B. Hammer and F. Besenbacher. 'Oxygen vacancies on TiO_2(110) and their interaction with H_2O and O_2: A combined high-resolution STM and DFT study'. *Surface Science* 598 (2005) 1-3, 226.

[239] P. J. D. Lindan, N. M. Harrison and M. J. Gillan. 'Mixed dissociative and molecular adsorption of water on the rutile (110) surface'. *Physical Review Letters* 80 (1998) 4, 762.

[240] P. J. D. Lindan and C. J. Zhang. 'Exothermic water dissociation on the rutile TiO_2(110) surface'. *Physical Review B* 72 (2005) 7, 75439.

[241] J. Goniakowski and M. J. Gillan. 'The adsorption of H_2O on TiO_2 and SnO_2(110) studied by first-principles calculations'. *Surface Science* 350 (1996) 1-3, 145.

[242] P. J. Feibelman. 'Partial dissociation of water on Ru(0001)'. *Science* 295 (2002) 5552, 99.

[243] S. P. Bates. 'Full-coverage adsorption of water on SnO_2(110): the stabilisation of the molecular species'. *Surface Science* 512 (2002) 1-2, 29.

[244] V. A. Gercher and D. F. Cox. 'Water-adsorption on stoichiometric and defective SnO_2(110) surfaces'. *Surface Science* 322 (1995) 1-3, 177.

[245] L. A. Harris and A. A. Quong. 'Molecular chemisorption as the theoretically preferred pathway for water adsorption on ideal rutile TiO_2(110)'. *Physical Review Letters* 93 (2004) 8, 86105.

[246] P. J. D. Lindan and C. J. Zhang. 'Comment on "Molecular chemisorption as the theoretically preferred pathway for water adsorption on ideal rutile TiO_2(110)"'. *Physical Review Letters* 95 (2005) 2, 029601.

[247] M. B. Hugenschmidt, L. Gamble and C. T. Campbell. 'The Interaction of H_2O with a TiO_2(110) Surface'. *Surface Science* 302 (1994) 3, 329.

[248] M. A. Henderson. 'An HREELS and TPD study of water on TiO_2(110): The extent of molecular versus dissociative adsorption'. *Surface Science* 355 (1996) 1-3, 151.

[249] R. Long, Y. Dai and B. Huang. 'Geometric and electronic properties of Sn-doped TiO_2 from first-principles calculations'. *Journal of Physical Chemistry C* 113 (2009) 2, 650.